



universität  
wien

## MASTERARBEIT / MASTER'S THESIS

Titel der Masterarbeit / Title of the Master's Thesis

"Fuzzy Dark Matter Halos: Angular Momentum, Vortices  
and Quantum Turbulence"

verfasst von / submitted by

Sonja Ornella Schobesberger, BSc BSc

angestrebter akademischer Grad / in partial fulfillment of the requirements for the degree

Master of Science (MSc)

Wien, 2020 / Vienna, 2020

Studienkennzahl lt. Studienblatt /  
degree programme code as it appears on  
the student record sheet:

A 066 861

Studienrichtung lt. Studienblatt /  
degree programme as it appears on  
the student record sheet:

Masterstudium Astronomie UG2002

Betreut von / Supervisor:

Mag. Mag. Dr. Tanja Rindler-Daller

---

# Acknowledgements

I would like to thank my supervisor Mag. Mag. Dr. Tanja Rindler-Daller most sincerely. Her dedication, eye for detail, vast knowledge of the field and concern for others create that kind of enjoyable working environment full of fruitful and valuable discussions students can only wish for. I consider myself very lucky that I was given the opportunity to work with her.

---

# Abstract

Competing theories on the nature of dark matter show different characteristic signature effects on scales of galactic halos ( $\approx$  kpc). Bose-Einstein condensed dark matter, BEC-DM, (also  $\psi$ DM or scalar field dark matter), a model motivated by several extensions to the standard model of particle physics like ultra-light axions, assumes that dark matter particles are bosons able to undergo Bose-Einstein condensation. Complicated dynamics arise due to the wave properties of this dark matter model. In particular, a Bose-Einstein-condensed dark matter halo subject to angular momentum may exhibit those quantum vortices we know from rotating laboratory condensates. These vortex-lines are basically “mini-tornadoes” where the density goes to zero and the velocity diverges. They are the building blocks of quantum turbulence. A virialized self-gravitating Bose-Einstein condensed dark matter halo satisfies the Gross-Pitaevskii-Poisson system of equations. Its fluid-like nature allows to distinguish between the so-called Thomas-Fermi and fuzzy regime, where the latter corresponds to a limit of vanishing dark matter self-interaction. The ground state attractor solution of the Gross-Pitaevskii-Poisson system in the fuzzy regime is a fundamental feature of this dark matter model which constitutes the central stable “soliton” core of  $\psi$ DM halos in the fuzzy regime. We apply an energy argument in order to determine whether the formation of one singly-charged vortex in the center of such a stable configuration due to rotation is energetically favored or not. In light of this, we developed two approximate analytical models for these central stable regions of BEC-DM halos; a Gaussian sphere and a compressible, ( $n = 2$ )-polytropic irrotational Riemann-S ellipsoid. We have shown that vortex formation in the fuzzy regime is not energetically favored, neither in the case of the Gaussian sphere model, nor in the case of the ( $n = 2$ )-polytropic irrotational Riemann-S ellipsoid. Moreover, according to our analysis higher dark matter particle masses imply that vortex formation is even less favored. Comparing our results with promising BEC-DM halo formation numerical simulations suggests that especially our ( $n = 2$ )-polytropic irrotational Riemann-S ellipsoid model provides a suitable tool to analyse the central, vortex-free regions of BEC-DM halos.

---

# Zusammenfassung

Theoretische Modelle über das grundlegende Wesen der dunklen Materie unterscheiden sich unter anderem in ihren Merkmalen auf galaktischen Längenskalen. Sogenannte Bose-Einstein-kondensierte dunkle Materie, BEC-DM, (auch bekannt als  $\psi$ DM oder Skalar Feld-dunkle Materie), ein durch Erweiterungen des Standardmodells der Teilchenphysik gut begründeter Ansatz, geht davon aus, dass die Teilchen, aus welchen dunkle Materie besteht, Bosonen sind. Diese unterliegen der Bose-Einstein Statistik und sind bekanntlich in der Lage einen makroskopischen Quantenzustand, auch bekannt als Bose-Einstein-Kondensat, zu bilden. Die folglich inhärenten Welleneigenschaften dieser Beschreibung führen zu faszinierender aber doch hochgradig komplexer Dynamik. Betrachtet man insbesondere BEC-DM Halos in Kombination mit Eigendrehimpuls, so besteht die Möglichkeit, dass sich sogenannte "vortices" oder Wirbel ausbilden. Diese Mini-Tornados, durch verschwindende Dichte und ins Unendliche wachsende Geschwindigkeit charakterisiert, sind von Bose-Einstein Kondensat Experimenten aus dem Labor bekannt. Es stellt sich heraus, dass sich Quantenturbulenz aus diesen Wirbelsträngen zusammensetzt. Zur Beschreibung eines virialisierten BEC-DM Halos dient das sogenannte Gross-Pitaevskii-Poisson Gleichungssystem. Dieses bietet eine quantenhydrodynamische Formulierung, welche die Unterscheidung zweier Grenzfälle zulässt; der Thomas-Fermi und "fuzzy" Limes. Letzterer entspricht dem Grenzfall verschwindender Selbstwechselwirkung der dunkle Materie Teilchen. Der Grundzustand des Gross-Pitaevskii-Poisson Gleichungssystems im fuzzy Limes stellt in seinem Erscheinungsbild ein grundlegendes Merkmal dieses Modells dar und findet sich in den stabilen, glatten Zentralregionen von fuzzy BEC-DM Halos. Im Rahmen dieser Arbeit wird eine Energieanalyse angewandt, um die Wahrscheinlichkeit des Auftretens eines derartigen einfach-gewickelten Wirbels im Zentrum eines BEC-DM Halos zu untersuchen. In Anbetracht dessen, wurden zwei approximative Modelle des stabilen BEC-DM Halozentrums erstellt; eine Gauß'sche Kugel und ein wirbelfreier Riemann-S Ellipsoid mit einem Dichteprofil, welches einer ( $n = 2$ )-Polytrope entspricht. Unsere Analyse kommt zu dem Schluss, dass das Auftreten eines "vortex" in keinem der beiden Fälle, weder für die Gauß'sche Kugel noch für den polytropischen Riemann-S Ellipsoid, energetisch begünstigt ist. Es stellt sich weiters heraus, dass mit steigender Bosonenmasse "vortex"-Bildung in steigendem Maße

---

unbegünstigt ist. Der Vergleich mit vielversprechenden Merger-Simulationen zeigt, dass insbesondere unser polytropisches Riemann-S ellipsoides Modell ein gut geeignetes analytisches Werkzeug zur Untersuchung der "vortex"-freien Zentralregionen eines BEC-DM Halos darstellt.

# Contents

<b>Overview</b>	<b>1</b>
<b>1 Introduction to the dark matter hypothesis</b>	<b>3</b>
1.1 Astrophysical evidence . . . . .	4
1.2 The $\Lambda$ CDM model and its persisting small-scale crisis . . . . .	7
1.3 A world beyond the $\Lambda$ CDM model . . . . .	9
<b>2 Scalar field dark matter</b>	<b>13</b>
2.1 Gross-Pitaevskii formulation of a dark matter superfluid . . . . .	14
2.2 The Thomas-Fermi regime . . . . .	18
2.3 The fuzzy regime . . . . .	21
<b>3 Superfluids, Bose-Einstein condensation and turbulence: A short excursion</b>	<b>29</b>
3.1 Bose-Einstein condensates . . . . .	29
3.2 Association of superfluids with Bose-Einstein condensation . . . . .	30
3.3 Vorticity . . . . .	31
3.4 Quantum turbulence . . . . .	35
<b>4 Rotating configurations of Bose-Einstein condensed dark matter halos</b>	<b>37</b>
4.1 Compressible ellipsoidal equilibrium figures . . . . .	39
<b>5 Vortex formation in the fuzzy regime</b>	<b>49</b>
5.1 Model A: The Gaussian sphere . . . . .	49
5.2 Model B: The irrotational Riemann-S ellipsoid . . . . .	73
<b>6 Conclusions and discussion</b>	<b>89</b>
<b>A Polytropic spheres</b>	<b>95</b>
<b>B The perturbed halo potential <math>\Phi_1</math>: An analytical approach</b>	<b>99</b>

---

<b>C Non-collisionality</b>	<b>105</b>
<b>Bibliography</b>	<b>111</b>
<b>List of Figures</b>	<b>117</b>

# Overview

We begin this thesis with Chapter 1, where we introduce the reader to the vast topic of *dark matter* (DM). This Chapter is dedicated to providing answers to questions like “What is dark matter?”, “Why do the majority of astrophysicists proceed on the assumption that it exists?”, “What kinds of theories on the nature of dark matter and its comprising particles are there?” and “How are they connected to the evolution and formation of structure in the Universe?”. Finally, we introduce so-called *scalar field* dark matter (SFDM), also referred to as Bose-Einstein-condensed DM (BEC-DM) or  $\psi$ DM; one major competing theory which is the focus of this thesis. Thus, we present in Chapter 2 the fundamental theoretical framework and its foundation - the Gross-Pitaevskii-Poisson system of equations - which we use for our analysis of a Bose-Einstein-condensed dark matter halo. In this Chapter, we see how the formulation may be rewritten in terms of quantum-mechanical fluid equations and how based on that, SFDM admits two limiting cases or regimes, the so-called Thomas-Fermi and fuzzy regime. Our analysis regards the fuzzy regime and combines two initially totally independent fields of research, dark matter astrophysics and condensed matter physics. The reason is that the goal of our analysis is to determine whether the formation of so-called *vortices*, the building blocks of quantum turbulence known to arise in driven laboratory Bose-Einstein condensates (BECs), is energetically favored in rotating Bose-Einstein-condensed fuzzy dark matter halos in equilibrium. Since this kind of analysis obviously requires the corresponding theoretical background of condensed matter physics, Chapter 3 includes a “crash course” on superfluids, BECs and quantum turbulence. We distinguish between two models of BEC-DM halos in the course of our energy analysis, where our second “halo model B” heavily relies on compressible generalizations of rotating figures of equilibrium and to be precise on the so-called compressible irrotational Riemann-S ellipsoid. As a result, Chapter 4 provides a detailed study of these equilibrium figures. In Chapter 5, the heart of this thesis, we present our energy analysis that shall decide whether the formation of one central singly-charged vortex occurs for our two given halo models. A conclusion of our results, their implications and comparison to the results of corresponding recent numerical simulations can be found in Chapter 6. Finally, some of the detailed theoretical aspects are relegated to three Appendices.

---

# Chapter 1

## Introduction to the dark matter hypothesis

As a concept, the problem of dark matter, one of the greatest mysteries of modern cosmology, is something scientists have encountered many times before in the history of physics and astronomy. Whenever anomalies appear, deviations from predictions of the current paradigm, thought patterns, theories, etc., one has to decide whether they should be regarded as something yet unseen, nevertheless a legitimate constitute within this paradigm, or as a need to refine or generalize or evolve the currently accepted laws of nature. [Bertone et al. \(2004\)](#) commence their review on particle dark matter with an eloquent comparison. There are two examples within the field of celestial mechanics, where in both cases observed motions deviated from the expected orbits, however the remedies in each case turned out to be of very converse nature. In the case of the anomalous motion of Uranus astronomers were led to suspect the existence of Neptune, which was eventually discovered in 1846. On the other hand, the solution to the anomalies in Mercury's motion required a more refined theoretical framework for gravitation, in other words Einstein's theory of general relativity.

For decades by now, we are confronted with a conceptually similar situation where we observe a certain set of "anomalies" at nearly every astrophysical scale, which will be explained in more detail, raising the question whether these belong to the "Uranus case" or to the "Mercury case", or to be precise; are scientists confronted with the existence of unseen, *dark* matter or do we have to rethink general relativity? This thesis proceeds from the dark matter hypothesis.

There are many different approaches and scientific pathways leading from different directions to this one issue, coined *dark matter*. Completely independent efforts for example in theoretical particle physics and astrophysics have been starting to show links. On the one hand observational evidence at all astrophysical scales has been collected over the years and on the other hand, coming from the realm of particle physics, there is by now plenty

of evidence for the existence of physics beyond the Standard Model. Most crucially, theoretical extensions to the Standard Model do provide viable dark matter particle candidates from the astrophysical point of view. As a consequence, we experience a strong interplay between particle physics, cosmology and astrophysics, where the formulation of new theories predicting new particles and the observational constraints of the particle's properties and parameters are co-dependent.

## 1.1 Astrophysical evidence

In Bertone et al. (2004) the astrophysical signs for dark matter are divided into three scale categories; signs on galactic scales, galaxy cluster scales and cosmological scales.

**Galactic Scales** It could be that galactic rotation curves are the most commonly mentioned direct evidence for dark matter on galactic scales. These curves plot the radial velocity of stars and gas against their distance from the galactic center. From Newtonian Dynamics we

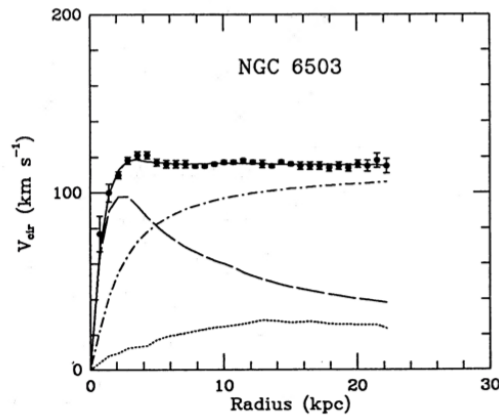


Figure 1.1: Rotation curve of NGC 6503 from Begeman et al. (1991). Dark matter, disk and gas contributions are represented by dashed-dotted, dashed and dotted lines, respectively.

expect curves according to

$$v(r) = \sqrt{\frac{GM(r)}{r}}, \quad (1.1)$$

where  $M(r) = \int 4\pi\rho(r)r^2dr$  and  $\rho(r)$  is the radial density profile, beyond the inner rigid-body-like rotation. Theory predicts that the curve should turn over and fall proportional to  $1/\sqrt{r}$  beyond the optical disc. However, observed rotation curves, obtained by combining observations of the 21cm line with optical surface photometry, show a characteristic flat behaviour at large distances, also far beyond the edge of the disk. One of the most famous

---

observations revealing this characteristics are those by Vera Rubin and Kent Ford of M31, see [Rubin and Ford \(1970\)](#), whose spectroscopic analysis revealed that a large amount of unseen matter must be holding these quickly rotating spiral galaxy together, since otherwise it would drift apart.  $v(r) \approx \text{constant}$  thereby implies the existence of a *dark* halo with  $\rho(r) \propto 1/r^2$  and  $M(r) \propto r$ . A typical example can be seen in figure 1.1. This feature is also seen in so-called Low Surface Brightness galaxies, which are probably everywhere dark matter-dominated.

There are numerous other arguments for dark matter on galactic scales from which we will mention only a few. There is for example the so-called Oort discrepancy (see [Bahcall et al. \(1992\)](#)). The amount of stars and other tracers of gravitational potentials do not seem to be compatible with the gravitational potential one can infer from their distribution in the solar neighborhood within the Milky way disk. Also, observations of dwarf spheroidal galaxies and measurements of their velocity distributions imply mass-to-light ratios larger than those observed in our local neighborhood, see for example [Vogt et al. \(1995\)](#). Finally, there are studies like [Moustakas and Metcalf \(2003\)](#) inferring substructure due to modulations of strong lensing.

**Scale of Galaxy Clusters** In 1933, measurements of the velocity dispersion of galaxies in the Coma cluster led Fritz Zwicky to propose something like dark matter in the modern sense for the first time. He inferred a mass-to-light ratio of  $\approx 400 (M/L)_{\odot}$  which exceeds the ratio in the solar neighborhood by two orders of magnitude ([Zwicky \(1933\)](#)).

About two decades later a true pioneer in every sense, twentieth-century astronomer Vera Rubin, started her scientific career. [Hooper \(2007\)](#) touches on the huge impact her career and personal efforts had on astronomy and the scientific society. Her findings provided some of the first actual evidence for the dark matter hypothesis. [Hooper \(2007\)](#) mentions her substantial contributions on galactic as well as cluster scales. At the beginning of her career she established that members of galaxy clusters might rotate about a gravitational center in the cluster and that their motions deviate from the Hubble flow. On top of that, she concluded that the amount of mass required to explain this motion must be larger than the total stellar mass observed in the cluster. These findings and her genius conclusion of invisible matter were immensely controversial at that time, and unfortunately even more so when published by a female scientist. The American Astronomical Society did not accept her findings in 1950 despite the enormous evidence she had accumulated. Later her doctoral thesis, [Rubin \(1954\)](#), concluded that galaxies clumped together, rather than being randomly distributed through space, a controversial statement not pursued by others for two decades.

Today we know that due to her strength, passion, genius and endurance in the face of discouraging sexism, she has been one of the astronomers who paved the way for other

---

women in the field <sup>1</sup>. As if that was not enough, her legacy is sometimes described as the beginning of a Copernican-scale change in cosmology.

Nowadays, astronomy offers several methods with which the mass of a galaxy cluster can be determined. In their review, [Bertone et al. \(2004\)](#) mention three of them. One can observe the distribution of radial velocities in a cluster and apply the virial theorem, infer the gravitational potential well through studies of weak gravitational lensing or study X-ray emission that traces the hot gas in rich clusters. They also mention that dynamical estimates provide values for mass-to-light ratios on galaxy cluster scales in the range  $(M/L)/1000 \approx 0.2 - 0.3$ .

**Cosmological scales** The Cosmic Microwave Background (CMB) offers a way to infer the total amount of dark matter in the Universe, see [Coles and Lucchin \(2003\)](#) for an introduction into CMB physics. It turns out that a lot of information about the evolution, content and geometry of our Universe is stored in the CMB power spectrum where the temperature fluctuations of the CMB are plotted as a function of angular size. This information can be extracted by comparing observed to theoretically modeled CMB power spectra. The Planck mission for example has provided observations of temperature (and polarization) anisotropies of CMB radiation and thereby the data to construct a CMB power spectrum. So-called cosmological models or often called "cosmologies" constitute the theoretical counter part consisting of a set of assumptions on the content and structure development of our Universe. [Planck Collaboration \(2018\)](#) start from what they denote "base"  $\Lambda$ -cold dark matter (CDM) model, a spatially-flat standard cosmological model with 6 parameters and adiabatic scalar perturbations given by a power-law spectrum. Fitting the observed spectrum with the cosmological model determines then the best-fit parameters from the peak of the likelihood surface. Among the directly or indirectly resulting cosmological parameters are the dark matter density today,  $\Omega_c h^2 = 0.1200 \pm 0.0012$ , and the baryon density today,  $\Omega_b h^2 = 0.02237 \pm 0.00015$  (see equations (23) and (24) of [Planck Collaboration \(2018\)](#)). Together, the parameter constraints from the CMB and other sources have converged remarkably on parameters of the  $\Lambda$ CDM model. Overall, parameter constraints from the CMB show a striking level of agreement with other constraints from other sources, which has led to the standard  $\Lambda$ CDM model being called the concordance cosmology. It is important evidence that this cosmological model, which constitutes a remarkably well description of the large-scale conditions of the Universe, is based on dark matter contributing roughly 27 percent to the mass-energy density.

---

<sup>1</sup>Regarding these struggles, we recommend her articles [Rubin \(1978\)](#) and [Rubin \(1982\)](#).

---

## 1.2 The $\Lambda$ CDM model and its persisting small-scale crisis

Many efforts and cosmological data have converged upon the  $\Lambda$ -cold dark matter paradigm, short  $\Lambda$ CDM, as cosmology's standard model. An impressive amount of agreement between the standard  $\Lambda$ CDM model, for the cosmic mass-energy content and structure formation and development, and observational data has earned it the title concordance cosmology. This model assumes a flat geometry and yields that dark matter contributes about 26% and baryonic matter about 5% to the mass-energy content while the dominant remainder seems consistent with the cosmological constant  $\Lambda$ , see [Planck Collaboration \(2016\)](#). Within this framework, the initial spectral index of primordial density fluctuations amounts to  $\approx 1$  ([Planck Collaboration \(2016\)](#)) which is consistent with inflationary initial conditions. In other words, the standard  $\Lambda$ CDM model involves an almost scale-invariant power spectrum of primordial density fluctuations. CDM acts like a pressureless fluid (this will be explained in a moment). Thereby, dark matter collapses readily under its own gravity and yields hierarchical non-linear structures which provide the underlying gravitational potential "hosting" baryonic matter. These so-called dark matter halos show self-similarity to such an extent (subhalos embedded in subhalos embedded in... etc.) that one of the features of the standard  $\Lambda$ CDM model is substantial power at small mass scales.

From the particle point of view, cold dark matter particles are non-relativistic, collisionless (see Appendix C) and cold in the sense that their velocity dispersion has almost no impact on structure formation. On large scales, they are supposed to interact with the particles of the Standard Model of particle physics and each other solely via gravity. Standard CDM particles are cold cosmic thermal relics which [Coles and Lucchin \(2003\)](#) describe as matter which was held in thermal equilibrium with the Universe's other components until their decoupling or so-called "freeze out" in the early Universe. Cold thermal relics are those which are non-relativistic at the time of decoupling, after which they cool off while the Universe expands. Consequently, standard CDM on large scales has a vanishing pressure, speed of sound and thermodynamical temperature, i.e. it holds

$$P_{\text{hom}} = w \rho_{\text{hom}} \quad \& \quad w = 0, \quad (1.2)$$

where the pressure and density are averaged over large distances. We go into more detail on the non-collisionality that is associated with the  $\Lambda$ CDM model in Appendix C. Collisionless cold dark matter can be modeled as a collisionless system of particles that is commonly described by the collisionless Boltzmann<sup>2</sup> equation together with the Poisson equation.

However, what is the particle realization of the standard  $\Lambda$ CDM model? There seem to be no viable particle candidates within the Standard Model (SM) of particle physics and

---

<sup>2</sup>Some authors refer to it as the Vlasov equation.

---

candidates arising from extensions to the SM still lack detection or laboratory support. There are two major candidates. The supersymmetric weakly interacting massive particles, short WIMPS, are thermal relics of order  $\mathcal{O}(GeV)$ , e.g. [Jungman et al. \(1996\)](#). Another option is the quantum chromodynamics (QCD) axion, which is a nonthermal relic of order  $\mathcal{O}(\mu eV)$ , e.g. [Peccei and Quinn \(1977\)](#).

It could very well be that the standard  $\Lambda$ CDM model would not be the dominant paradigm it is today, if it was not for numerical simulations. The Millennium simulation [Springel et al. \(2005\)](#) based on the cosmological simulation code GADGET-2, see [Springel \(2005\)](#), represents one of those high-impact simulations. The GADGET-2 code follows the dark matter component and stars in galaxies by treating them as a collisionless fluid which is subject to gravity. They are described by the collisionless Boltzmann equation and the Poisson equation which the code solves with the N-body method. Ordinary baryons like hydrogen and helium are represented by an ideal gas and followed by smoothed particle hydrodynamics. The two components are coupled via gravity and placed in an expanding Universe given by the Friedman equations. The resulting cosmic web of halos and galaxies across all redshifts based on the standard  $\Lambda$ CDM model reflects very successfully the picture we have from numerous types of large-scale observational data like galaxy surveys, the CMB, the Lyman- $\alpha$  forest or weak gravitational lensing.

However, with improving resolution of the simulations based on the standard  $\Lambda$ CDM model, the model faces enduring inconsistencies between predictions and observations on small, galactic scales. [Weinberg et al. \(2015\)](#) give a review on what has by now been coined "small-scale crisis of  $\Lambda$ CDM". Considerable power of the  $\Lambda$ CDM model on small scales gives rise to the so-called "cusp-core", "missing satellites" and "too-big-to-fail" problem.

**The Cusp-Core problem** Essentially, the collisionless  $\Lambda$ CDM model predicts amounts of dark matter in the central regions of galaxies, which are simply too high. According to N-body simulations dark matter halos and subhalos have density profiles which are singular or "cuspy" in their centers. [Navarro et al. \(1997\)](#) developed a universal density profile of dark matter halos and subhalos due to hierarchical clustering in standard  $\Lambda$ CDM N-body simulations. This famous NFW-profile, a function of the radial distance  $r$ , is given by

$$\rho(r) = \rho_s \left( \frac{r}{r_s} \right)^{-1} \left( 1 + \frac{r}{r_s} \right)^{-2}, \quad (1.3)$$

where  $r_s$  and  $\rho_s$  are halo parameters. One can see that this profile scales as  $r^{-1}$  for small  $r$  and as  $r^{-3}$  towards large  $r$ . However, according to [Weinberg et al. \(2015\)](#) a majority of rotation curves of galaxies, even of low surface brightness galaxies or dwarf galaxies (e.g. [Burkert \(1995\)](#) or [McGaugh and de Blok \(1998\)](#)), prefer "cored" density profiles, who scale as  $\rho \propto r^0$

---

in the center.

**Missing Satellites problem** The standard collisionless CDM model “preserves” its already mentioned initial power spectrum down to the smallest scales in the sense that it retains a very high amount of low-mass substructure in the form of dark matter subhalos. However, observations do by far not confirm these predictions. [Hui et al. \(2017\)](#) highlight this controversy in their introduction by comparing the galaxy number density,  $dn(M_*) \propto M_*^{-1.2} dM_*$ , to the predicted dark matter halo number density,  $dn(M_h) \propto M_h^{-2} dM_h$ , where  $M_*$  and  $M_h$  denote the total stellar mass and dark matter halo mass, respectively. As described in [Weinberg et al. \(2015\)](#), according to simulations, a  $10^{12} M_\odot$  (Milky Way-like) dark matter halo comprises a huge number of subhalos which are massive enough to host satellite galaxies. The model of [Moore et al. \(1999\)](#) predicted that the Milky Way’s halo, to be precise its virialized extent, should incorporate approximately 500 satellite galaxies with higher circular velocities compared to the Draco and Ursa Minor dwarfs. As opposed to this, we know approximately 10 satellite galaxies orbiting the Milky Way. However, [Weinberg et al. \(2015\)](#) argue that the missing satellites problem is the one problem which can be solved by “baryonic physics” suppressing star formation efficiency.

**Too-Big-to-Fail problem** Taking a closer look at the most luminous satellite galaxies of the Milky Way (or Andromeda) galaxy raises another, as [Weinberg et al. \(2015\)](#) conclude, very significant discrepancy between predictions of the collisionless  $\Lambda$ CDM model and observational data. In principle, we would expect the most massive dark matter subhalos to host the most luminous satellites. However, the masses of the central regions of the most massive subhalos in a  $10^{12} M_\odot$  (Milky Way-like) simulated dark matter halo exceed the masses inferred from stellar dynamics of the most massive observed dwarf satellites of the Milky Way by a factor of about 5, see for example [Boylan-Kolchin et al. \(2011\)](#) who coined the phrase “too-big-to-fail”. How can it be that the most massive subhalos, which one would expect to be “too big to fail” hosting a galaxy, remain dark causing the most luminous satellites to reside in other halos? Following [Weinberg et al. \(2015\)](#), this is a particularly serious issue, since it arises in dark matter dominated massive systems.

### 1.3 A world beyond the $\Lambda$ CDM model

We find ourselves in a situation in which a prevalent notion called  $\Lambda$ CDM model or even paradigm hits on problems. How do we conceive this? There are essentially three different levels of perception considering this specific scientific framework yielding three different concept formations.

---

Proceeding from a point of view that considers the  $\Lambda$ CDM model to be fundamentally “correct”<sup>3</sup>, one arrives at widely-considered efforts to *resolve* discrepancies via baryonic feedback. Processes like photo-heating and stripping could according to [Brooks et al. \(2013\)](#) solve the missing satellites problem.

The second and third level represent entirely different perceptions, but yield essentially similar efforts. On the one hand, you can start from the notion which accepts the  $\Lambda$ CDM model as the current paradigm. Coming from there, dark matter models including particles with inherently different properties than those covered by  $\Lambda$ CDM are obligated to provide a basis of legitimacy. This very often manifests itself as a chain of reasoning starting from the  $\Lambda$ CDM paradigm and using its small-scale-crisis to justify another model. On the other hand, one can think of the  $\Lambda$ CDM model as one out of many, namely the model that has been worked on a lot and that can explain an overwhelming amount of observational data but definitely not all of it. This view point does not require any justifications for other models. Both view points however yield alternative underlying dark matter theories. There are for example models which do not rely on dark matter being pressureless.

One variant is so-called *warm* dark matter (WDM). Indeed, DM particle candidates can be classified according to their velocity dispersion that in turn yields their free-streaming length. According to [Viel et al. \(2005\)](#) warm dark matter refers to thermal relics which have just about the right amount of velocity dispersion so that their free-streaming length smooths out density fluctuations below a certain scale so that low-mass structure formation will be suppressed. In other words, WDM effectively reduces structure formation below its so-called free-streaming scale. Theoretical particle physics offers the gravitino (the graviton’s super-symmetric partner) and the right-handed sterile neutrino as WDM candidates.

*Self-interacting* dark matter (SIDM) proposed by [Spergel and Steinhardt \(2000\)](#) represents another possibility. Here, non-collisionality is given up in favor of self-interaction between dark matter particles. There is no reason preventing dark matter particles from self-interaction mediated through some “dark” force. This scenario implies that the particles scatter elastically via  $2 \rightarrow 2$  interactions yielding “collisional pressure” which may modify or even suppress small-scale structure. [Tulin and Yu \(2018\)](#) give a vast overview of SIDM arguing that the cross-section per unit mass must at least amount to

$$\frac{\sigma}{m} \approx 1 \text{ cm}^2/\text{g}, \quad (1.4)$$

in order to have the desired effect on small scales, where at the same time the collision rate is negligible at large scales.

However, this thesis is dedicated to another promising and, regarding its nature, quite

---

<sup>3</sup>At this point, we are at risk to enter a discussion on how to define whether a scientific theory is correct or not. This would go far beyond the scope of this thesis, which is why we refer to corresponding considerations in the context of philosophy of science.

---

remarkable dark matter model - so-called *scalar field* dark matter (SFDM). Non-thermally generated ultralight bosonic scalar fields could manifest themselves as cold “wavelike” DM. Theoretical particle physics offers particle candidates which may constitute SFDM. One example would be the class of ultralight axions - the axiverse - predicted by string theory and investigated by [Arvanitaki et al. \(2010\)](#). Axion cosmology is a very diverse field of research, see [Marsh \(2016\)](#).

In principle, certain conditions allow bosons to occupy (or “condense into”) one macroscopic quantum state, which is often referred to as Bose-Einstein condensation, with the result that they can be described by one classical field. Coming from axion cosmology, [Davidson \(2015\)](#) notes that it could be very misleading to talk about “Bose-Einstein condensates (BECs) of axions” since due to the way axion dark matter is produced in the early Universe it is already a classical field. They propose a “translation” of notions in which “classical field”, “Bose-Einstein condensation” and “condensed regime” refer to one and the same thing. These considerations are part of the interesting topic whether axions display long-range correlation.

This kind of dark matter was formed in a low-momentum, non-relativistic (cold) state whose field may be described by the coherent wavefunction  $\psi(\vec{r}, t)$ . This wavefunction shows interference patterns and quantum fluctuations which determine the dark matter distribution. These (kpc scale) fluctuations are the reason why for the longest time there have been no high resolution simulations of SFDM (often also referred to as BEC-DM or  $\psi$ DM). The dark matter only cosmological simulations of [Schive et al. \(2014a\)](#) showed how cosmic structure forms as a consequence of the quantum mechanical wave properties of  $\psi$ DM. In Chapter 2, we will see how BEC-DM can be characterized by a quantum hydrodynamical or fluid description. In comparison to standard CDM, there appears an additional quantum pressure term or “quantum stress” arising from the uncertainty principle of quantum mechanics (cf. the Schrödinger equation) which is able to work against gravity up to DM halo scales depending on the axion mass. According to [Schive et al. \(2014a\)](#), this quantum pressure yields a comoving Jeans length,  $\lambda_J \propto (1+z)^{1/4} m^{-1/2}$ , where  $z$  denotes redshift and  $m$  the boson mass. This finite scale suppresses small-scale structure formation below a cutoff mass.

$\psi$ DM shows quite complicated dynamics. The simulations of [Schive et al. \(2014a\)](#), in which they evolve one single coherent wave(function), demonstrate that the cosmic large-scale structure, a web of filaments and voids, is indistinguishable from large scale structures seen in standard  $\Lambda$ CDM simulations. However, a closer look at gravitationally bound objects, which arise in this  $\psi$ DM cosmology, reveals a detailed core-halo structure. [Chavanis \(2019b\)](#) and [Hui et al. \(2017\)](#)<sup>4</sup> describe the relaxation process of systems comprised of BEC-

---

<sup>4</sup>This paper (and [Schive et al. \(2014a\)](#)) consider so-called *fuzzy* dark matter. Regarding SFDM, one can distinguish between two limiting cases, where one of them is often referred to as fuzzy dark matter, see 2.3.

---

DM which leads to this core-halo equilibrium configuration. These systems relax by means of a process called gravitational cooling during which excited states of the wavefunction radiate parts of the scalar field. The result, shown in [Schive et al. \(2014a\)](#) is a characteristic feature of BEC-DM. In the center of these eventually virialized objects, we find a coherent dense (condensed) wave that forms a de-Broglie wavelength sized flat core. This “solitonic” core corresponds to the stable, minimum-energy solution admitted by self-gravitating BEC-DM systems and its smooth “cored” density profile (including a finite central density) does not contradict observations, unlike the cuspy profiles of standard  $\Lambda$ CDM. The surroundings of this core are traversed by a finite number of interfering excited states yielding a time-dependant granularity. The fact that these surroundings’ density scales like an NFW profile suggests again that BEC-DM and standard CDM behave similarly over scales much larger than the boson’s possibly *kpc*-scaled de-Broglie wavelength.

Consistency with constraints by large-scale structure sets a lower bound to the axion mass,  $m > 10^{-23}$  eV, see e.g. [Bozek et al. \(2015\)](#). However, due to the scale symmetry of underlying equations (at least in the fuzzy regime, see [2.3](#)) theoretical results considering BEC-DM are universally applicable, regardless of the boson’s mass.

## Chapter 2

# Scalar field dark matter

The vast spectrum of hypotheses on the constituents of dark matter can be divided into particle- and wave-like DM. If the dark matter particle mass is low enough, we are presented essentially different phenomenology and speak of so-called *wave* or *fuzzy dark matter* (a term introduced in [Hu et al. \(2000\)](#)), in the sense that the particle's de-Broglie wavelength for given mass  $m$  and velocity  $v$ ,

$$\lambda_{deB} = \frac{h}{mv}, \quad (2.1)$$

exceeds the typical inter-particle separation or even becomes astronomically relevant:

$$\frac{\lambda_{deB}}{2\pi} = 1.92 \text{ kpc} \left( \frac{10^{-22} \text{ eV}}{m} \right) \left( \frac{10 \text{ km s}^{-1}}{v} \right). \quad (2.2)$$

Given that *wave* dark matter refers to dark matter particles that are able, in the most literal sense, to occupy macroscopically their quantum ground state, the Pauli exclusion principle demands wave dark matter to be comprised of bosons. Hence, we are confronted with a scenario, where dark matter is made up of ultra-light bosons or axion-like particles (ALPs) with masses of the order of  $10^{-23} - 10^{-20}$  eV.

Wave dark matter is commonly modeled by a scalar field, and hence often referred to as scalar-field dark matter (SFDM). [Hui et al. \(2020\)](#) introduce their analysis of defects (due to destructive interference) in wave dark matter on galactic scales and above by considering a real Klein-Gordon scalar field  $\phi$ , which is minimally coupled to gravity and whose action is described by

$$S = \int d^4x \sqrt{-g} \left( -\frac{1}{2}(\partial\phi)^2 - \frac{m^2}{2}\phi^2 \right). \quad (2.3)$$

Here, it is assumed that any interaction of the scalar field besides gravity can be neglected,

i.e. that the self-interaction of the axion-like particle can be ignored <sup>5</sup>. The situations of interest are restricted to the non-relativistic limit, hence it is convenient to parameterize the dark matter field as

$$\phi = \frac{1}{\sqrt{2m}} \left( \psi e^{-imt} + \psi^* e^{imt} \right), \quad (2.4)$$

with  $\psi$  denoting a complex scalar field.  $\psi$  satisfies a Schrödinger equation coupled to gravity

$$i\partial_t \psi = -\frac{1}{2m} \nabla^2 \psi + m\Phi \psi, \quad (2.5)$$

assuming that  $|\dot{\psi}| \ll m|\psi|$  and dropping rapidly oscillating terms <sup>6</sup>. The gravitational potential  $\Phi$  satisfies the Poisson equation sourced by the mass density  $\rho$ ,

$$\nabla^2 \Phi = \frac{\rho}{2M_{pl}^2}, \quad (2.6)$$

where  $M_{pl}$  denotes the Planck mass and  $\rho = m|\psi|^2$ . If the factor  $\hbar$  was reintroduced (as it will be in later Sections), it would become clear that  $\hbar$  and  $m$  always appear in the combination  $\hbar/m$ . Hence, on the one hand the wave properties of this classical field configuration lead to behavior analogous to quantum-mechanical phenomena, but on the other hand the physics is classical.

Our work deals with dark matter halos at galactic scales and below. In theory the complex scalar field  $\psi$  produces galactic DM halos through so-called Bose-Einstein condensation, see for example [Arbey et al. \(2001\)](#). Within this theory, at zero temperature bosonic particles may condense into self-gravitating Bose-Einstein condensates, a macroscopic occupation of the ground quantum state. In that case, the complex scalar field corresponds to the condensate's wavefunction.

Evidence for the existence of Bose-Einstein-condensates comes from laboratory experiments, performed on very small (laboratory) scales, so far. In the following, theory and formalism stimulated by the exciting first experimental realizations of Bose-Einstein condensates (BECs) will be applied to analyze a condensate state of matter in a cosmic background.

## 2.1 Gross-Pitaevskii formulation of a dark matter superfluid

General-relativistic effects can usually be neglected at galactic scales since densities are very low and so the Newtonian limit will be applied. Hence, the foundation of our model of a self-gravitating BEC halo is the Gross-Pitaevskii (GP) equation, a non-linear Schrödinger

<sup>5</sup>In the following Sections, self-interaction will be included as part of a more general description of condensates and will then be ignored again due to the choice of a certain regime. However, in [Hui et al. \(2017\)](#) and [Hui et al. \(2020\)](#) it is argued that self-interaction is subdominant on galactic scales and above in the case of ALPs.

<sup>6</sup>Notice that  $\hbar = c = 1$  in this context.

---

equation. In 1961 Eugene Gross and Lev Pitaevskii independently formulated this theoretical framework to account for the quantized vorticity of Bose gases, see Section 3.3. There they originally incorporate an external trapping potential in the context of experimental setups. However, our analysis requires to consider the gravitational potential of a galactic halo:

$$i\hbar \frac{\partial \psi}{\partial t} = -\frac{\hbar^2}{2m} \Delta \psi + (m\Phi + g|\psi|^2)\psi, \quad (2.7)$$

where  $|\psi|^2(\vec{r}, t) = n(\vec{r}, t)$  corresponds to the number probability density,  $m$  denotes the particle mass,  $\Delta$  the Laplace operator and  $\Phi$  the gravitational potential. This equation (disregarding the replacement of the trapping potential) governs the evolution of the condensate's wavefunction in the case of dilute nonuniform Bose gases according to [Pitaevskii and Stringari \(2003\)](#). By means of Poisson's equation,

$$\Delta \Phi = 4\pi G m |\psi|^2, \quad (2.8)$$

the density is self-consistently coupled to the halo gravitational potential, where  $G$  denotes the gravitational constant.

This mean-field theory relies on the assumption that all bosons in the halo volume  $V$  reside in one quantum state, i.e. one single-particle state  $\psi$ <sup>7</sup>. This complex wavefunction is then normalized by the total number of particles  $N$ ,

$$N = \int_V |\psi|^2 dV. \quad (2.9)$$

In contrast to standard collisionless cold dark matter, SFDM (here in terms of the Gross-Pitaevskii framework) does in general include self-interaction of the dark matter particles. The energy of the condensate incorporates an effective interaction potential

$$\frac{g}{2} |\psi|^4, \quad (2.10)$$

with self-interaction strength or coupling constant  $g$ . Requiring a dilute gas together with a low-energy limit allows to disregard interactions between more than two bodies and thus the interaction strength is given by

$$g = 4\pi\hbar^2 \frac{a_s}{m}, \quad (2.11)$$

where  $a_s$  is the scattering length of the bosons. The dark matter particles in this scenario scatter elastically with each other. The strict requirement of a dilute gas demands  $a_s$  to be way smaller than the mean distance between particles. The sign of the parameter  $g$  is set by

---

<sup>7</sup>The label "single-particle state" can be misleading since the system in question is still made up of  $N$  particles. However, the extraordinary properties of total condensation are hereby emphasized.

the sign of  $a_s$ .

The physical meaning of the Gross-Pitaevskii-Poisson system is enlightened by applying the so-called Madelung transformation to the wavefunction  $\psi(\vec{r}, t)$ . Via decomposing the wavefunction into its amplitude and phase function

$$\psi(\vec{r}, t) = |\psi|(\vec{r}, t)e^{iS(\vec{r}, t)} = \sqrt{\frac{\rho(\vec{r}, t)}{m}}e^{iS(\vec{r}, t)}, \quad (2.12)$$

where

$$\rho(\vec{r}, t) = m|\psi|^2 \quad (2.13)$$

is the dark matter halo density. Inserting equation (2.12) into (2.7) and separating the real and imaginary parts decouples the GP equation into two equations for the real amplitude function  $|\psi|$  and real phase function  $S$ .

$$-\frac{2m}{\hbar}|\psi|\frac{\partial S}{\partial t} + \Delta|\psi| - |\psi|(\vec{\nabla}S)^2 - \frac{2m}{\hbar^2}(m\Phi + g|\psi|^2)|\psi| = 0 \quad (2.14)$$

and

$$\frac{\partial|\psi|^2}{\partial t} + \vec{\nabla} \cdot \left( |\psi|^2 \frac{\hbar}{m} \vec{\nabla} S \right) = 0. \quad (2.15)$$

Following Madelung (1927), the bulk (or flow) velocity field can be identified as the gradient flow

$$\vec{v} = \frac{\hbar}{m} \vec{\nabla} S \quad (2.16)$$

through the relations for the current density

$$\vec{j}(\vec{r}, t) = \frac{\hbar}{2im}(\psi^* \vec{\nabla} \psi - \psi \vec{\nabla} \psi^*) = n \frac{\hbar}{m} \vec{\nabla} S \quad (2.17)$$

and

$$\vec{j} = n \cdot \vec{v}. \quad (2.18)$$

By that, equations (2.14) and (2.15) can be rewritten as a system of hydrodynamic equations for the variables  $\rho$  and  $\vec{v}$  emphasizing the (super-)fluid character of the system, see for example Rindler-Daller and Shapiro (2012), Tsatsos et al. (2016) or Chavanis (2019b). The results are an Euler-like equation of motion,

$$\rho \frac{\partial \vec{v}}{\partial t} + \rho(\vec{v} \cdot \vec{\nabla})\vec{v} = -\rho \vec{\nabla} Q - \rho \vec{\nabla} \Phi - \vec{\nabla} P_{SI}, \quad (2.19)$$

and a continuity equation,

$$\frac{\partial \rho}{\partial t} + \vec{\nabla} \cdot (\rho \vec{v}) = 0. \quad (2.20)$$

---

The right-hand side of equation (2.19) requires further investigation. The so-called Bohm quantum potential, defined as

$$Q = -\frac{\hbar^2}{2m^2} \frac{\Delta\sqrt{\rho}}{\sqrt{\rho}}, \quad (2.21)$$

gives rise to what is often referred to as ‘quantum pressure’. In addition, the self-interaction yields a pressure of polytropic form

$$P_{SI} = \frac{g}{2m^2} \rho^2 = K_p \rho^{1+1/n}. \quad (2.22)$$

The polytropic index  $n$  corresponds to 1 and the polytropic constant  $K_p$  is only depending on the DM particle parameters  $m$  and  $g$ . These two are the fundamental particle parameters of this framework.

Following [Rindler-Daller and Shapiro \(2012\)](#), we will too restrict the analysis to stationary systems, i.e. the time-independent GP equation including the chemical potential  $\mu$

$$\mu\psi_s(\vec{r}) = -\frac{\hbar^2}{2m} \Delta\psi_s(\vec{r}) + (m\Phi + g|\psi_s|^2)\psi_s(\vec{r}). \quad (2.23)$$

The time-independent GP equation can be obtained from the time-dependent equation (2.7) by inserting the state

$$\psi(\vec{r}, t) = \psi_s(\vec{r})e^{-i\mu t/\hbar}. \quad (2.24)$$

Stationary states have this form of wavefunction, evolving harmonically in time and yielding a time-independent density  $\rho = m|\psi_s|^2$  and gravitational potential. Of course  $\psi_s$  itself can be decomposed analogously to (2.12) as

$$\psi_s(\vec{r}) = |\psi_s|(\vec{r})e^{iS_s(\vec{r})}, \quad (2.25)$$

where from now on the subscript  $s$  will be omitted. The GP energy functional is given by

$$E[\psi] = \int_V \left[ \frac{\hbar^2}{2m} |\nabla\psi|^2 + \frac{m}{2} \Phi |\psi|^2 + \frac{g}{2} |\psi|^4 \right] d^3r \quad (2.26)$$

By means of decomposition (2.25) we can write the total energy,

$$E = K + W + U_{SI} \quad (2.27)$$

---

as a sum of the total kinetic energy

$$K \equiv \int_V \frac{\hbar^2}{2m} |\nabla\psi|^2 d^3r \quad (2.28)$$

$$= \int_V \frac{\hbar^2}{2m^2} (\nabla\sqrt{\rho})^2 d^3r + \int_V \frac{\rho}{2} \vec{v}^2 d^3r \equiv K_Q + T, \quad (2.29)$$

the gravitational potential energy

$$W \equiv \int_V \frac{\rho}{2} \Phi d^3r \quad (2.30)$$

and the internal energy

$$U_{SI} \equiv \int_V \frac{g}{2m^2} \rho^2 d^3r. \quad (2.31)$$

$K_Q$  is the part of the kinetic energy accounting for the quantum-like phenomena,  $T$ , as the bulk kinetic energy of the system, includes rotational or internal motions and  $U_{SI} = \int P_{SI} dV$  is determined by the self-interaction pressure given in (2.22). If we allow the internal energy to arise from any polytropic pressure  $P = K_p \rho^{1+1/n}$ , i.e.

$$U = K_p n \int \rho^{1+1/n} d^3r, \quad (2.32)$$

then the scalar virial theorem writes

$$2K + W + \frac{3}{n}U = 0. \quad (2.33)$$

Considering the three terms on the right-hand side of the Euler-like equation (2.19), we can distinguish two regimes. This framework provides two different forces which can stabilize the halo against gravitational collapse. On the one hand, there is the regime where self-interaction or in other words the scattering of the DM particles is entirely neglected and hence solely the quantum potential works against gravity. On the other hand, there is the regime of strongly interacting particles, where self-interaction pressure dominates and balances gravity.

## 2.2 The Thomas-Fermi regime

The aim of this Section is to give a brief but insightful overview of the Thomas-Fermi limit within the Gross-Pitaevskii framework.

A static state of the hydrodynamic equations (2.19) and (2.20), i.e.  $\partial_t \rho = 0$  and  $\vec{v} = 0$ , corresponds to the equation of quantum hydrostatic equilibrium

$$\rho \vec{\nabla} Q + \vec{\nabla} P_{SI} + \rho \vec{\nabla} \Phi = 0. \quad (2.34)$$

---

It accounts for the balance between the quantum potential, the pressure due to scattering and gravity. Following [Chavanis \(2019a\)](#) and [Chavanis \(2019b\)](#)<sup>8</sup>, we combine equation (2.34) with the Poisson equation and obtain a differential equation of quantum hydrostatic equilibrium determining the density of the DM halo in equilibrium,

$$\frac{\hbar^2}{2m^2} \Delta \left( \frac{\Delta \sqrt{\rho}}{\sqrt{\rho}} \right) - \vec{\nabla} \cdot \left( \frac{\vec{\nabla} P_{SI}}{\rho} \right) = 4\pi G \rho. \quad (2.35)$$

Moreover, with  $P_{SI}$  as in (2.22), we have

$$\frac{\hbar^2}{2m^2} \Delta \left( \frac{\Delta \sqrt{\rho}}{\sqrt{\rho}} \right) - \frac{4\pi a_s \hbar^2}{m^3} \Delta \rho = 4\pi G \rho. \quad (2.36)$$

The TF approximation amounts to setting  $Q = 0$ , which leaves

$$- \frac{4\pi a_s \hbar^2}{m^3} \Delta \rho = 4\pi G \rho, \quad (2.37)$$

an analogue of the Lane-Emden equation of polytropic index  $n = 1$ . For spherical symmetric configurations, this equation has an analytical solution given by

$$\rho(r) = \rho_0 \frac{\sin(\pi r/R)}{\pi r/R}, \quad (2.38)$$

(where  $\rho_0$  denotes the central density) which is stable and has a compact support:

$$R = \pi \left( \frac{a_s \hbar^2}{G m^3} \right)^{1/2} \quad (2.39)$$

is the radius corresponding to the first root of the profile, see Appendix A about polytropic spheres. It is noteworthy that this radius is independent of the halo's total mass  $M$ . As in [Rindler-Daller and Shapiro \(2012\)](#) we restrict this overview to repulsive self-interaction, i.e.  $a_s > 0$  and hence  $K_p > 0$ . [Chavanis \(2019a\)](#) assume that the smallest observed halo with typical values

$$R \approx 1 \text{ kpc}, \quad M \approx 10^8 M_\odot \quad (2.40)$$

corresponds to the ground state, thus getting

$$\left( \frac{a_s}{\text{fm}} \right) \left( \frac{\text{eV}/c^2}{m} \right)^3 = 3.28 \times 10^3. \quad (2.41)$$

[Tulin and Yu \(2018\)](#) give a table on observations which give constraints on the self-interaction

---

<sup>8</sup>Notice that they employ the convention  $\rho = |\psi|^2$ , which yields different powers of  $m$  in some parts of their hydrodynamic formulation.

---

cross section per particle mass  $\sigma/m = (4\pi a_s^2)/m$ . [Chavanis \(2019a\)](#) proceed on the constraint  $\sigma/m < 1.25 \text{ cm}^2/\text{g}$  and arrive at an upper boson mass bound,

$$m = 1.1 \times 10^{-3} \text{ eV}/c^2, \quad a_s = 4.41 \times 10^{-6} \text{ fm}, \quad (2.42)$$

and a lower one,

$$m = 2.92 \times 10^{-22} \text{ eV}/c^2, \quad a_s = 8.13 \times 10^{-62} \text{ fm}. \quad (2.43)$$

In this case, the values correspond to the bound  $\sigma/m = 1.25 \text{ cm}^2/\text{g}$  and to the transition between the Thomas-Fermi and non-interacting (fuzzy) regime, respectively. As a consequence, one can see that allowing repulsive self-interaction between the dark matter particles, a wide range of boson masses would be possible.

[Rindler-Daller and Shapiro \(2014\)](#) discuss amongst other things boson scattering and relaxation times of Bose-Einstein condensed dark matter halos and for example arrive at an upper bound of

$$m \leq 1.066 \times 10^{-3} \text{ eV}/c^2 \quad (2.44)$$

by comparing their expression for the relaxation time of a spherical, uniform halo core with the Hubble time.

Two of the first to postulate and discuss "repulsive" and "fluid" dark matter were [Goodman \(2000\)](#) and [Peebles \(2000\)](#). The postulation included a condensate of massive bosons allowed to interact via gravity and repulsive self-interaction. More specifically, [Peebles \(2000\)](#) proposed a model in which the scalar field interacts with itself by a potential close to quartic for large and close to quadratic for small field values. As a result, they were able to conclude huge consequences regarding the minimum length scale for bound objects and the low-mass end of the primordial mass power spectrum.

[Rindler-Daller and Shapiro \(2012\)](#) establish conditions on the validity of the Thomas-Fermi regime and whether a halo lies in the TF regime or not. There is a characteristic length scale mentioned in classic literature on Bose-Einstein condensates, for example [Pethick and Smith \(2008\)](#), namely the so-called healing length  $\xi$ . This length describes the distance over which the  $\psi$  tends to its background value when it is subjected to a localized distortion or perturbation and is the result of balancing the quantum kinetic term with the self-interaction at order level accuracy,

$$0 = -\frac{\hbar^2}{2m} \frac{\psi}{\xi^2} + g|\psi|^2\psi, \quad (2.45)$$

yielding

$$\xi = \frac{\hbar}{\sqrt{2\rho g}}, \quad (2.46)$$

---

with  $\bar{\rho} = 3M/(4\pi R^3)$ . To put it another way, it takes the gas or superfluid this distance to “heal” a local disturbance. According to (2.46) the healing length increases with decreasing self-interaction strength  $g$  for given mean density. By estimating the forces associated with the quantum kinetic term and the self-interaction term and using relations (2.39) and (2.53), [Rindler-Daller and Shapiro \(2012\)](#) conclude that in the TF regime the system’s size is way larger than the healing length and that the de-Broglie wavelength is a lot smaller than the size of the halo, i.e.

$$R \gg \xi, \quad \frac{R}{\lambda_{deB}} \gg 1. \quad (2.47)$$

Moreover, they show that  $\lambda_{deB} \sim 4.3\xi$ .

## 2.3 The fuzzy regime

This Section is dedicated to the regime of extremely low particle masses, where the de-Broglie wavelength is a significant fraction of or even comparable to the system’s size and the self-interaction is subdominant. To be precise, we will consider BEC- cold dark matter without self-interaction, also referred to as fuzzy, vanilla or free scalar-field dark matter from here on.

It shall be understood that the object we will repeatedly term “halo” or “BEC-DM halo” in this and following Sections refers to a region whose size is comparable to the de-Broglie wavelength and whose wave function / density profile corresponds to the ground state of the Gross-Pitaevskii-Poisson system in the fuzzy limit. This object in question may either constitute an entire actual halo or just a virialized core region embedded into a larger halo.

The following analyses and discussions on Bose-Einstein-condensed dark matter halos in the fuzzy regime require to define and thereby introduce quantities which seem inherent in this regime.

Considering the Thomas-Fermi regime within the framework of the Gross-Pitaevskii model, the reader is now already familiar with the so-called healing length  $\xi$ , describing a length scale over which the interaction energy becomes comparable to the kinetic one. It is a function of the interaction strength  $g$  and mass density, see [Pethick and Smith \(2008\)](#).

By translating these notions into the fuzzy regime through a replacement of the interaction energy by the gravitational energy, we introduce the so-called *gravitational healing length*,  $\xi_G$ , and derive it by setting the quantum kinetic energy equal to the gravitational energy, see the Gross-Pitaevskii energy functional (2.26),

$$\frac{\hbar^2}{2m} |\nabla\psi|^2 = \frac{m}{2} \Phi |\psi|^2. \quad (2.48)$$

---

The kinetic energy is of order  $\hbar^2/(2m\zeta_G^2)$  and the gravitational energy is of order  $mGM/(2\zeta_G)$ , which yields

$$\zeta_G = \frac{\hbar^2}{m^2GM}, \quad (2.49)$$

where  $M$  is the total mass, i.e. a global halo property. Approximating the spatial dimension in  $\Phi$  with  $\zeta_G$ , i.e. with the same length scale used to approximate the Laplace operator on the left-hand side, corresponds to the notion of the Jeans instability. Another possibility would have been to choose the gravitational energy to be of order  $mGM/(2R)$ , which represents global properties as opposed to the local sensitivity of the Laplace operator. ( $R$  denotes the halo radius.)

The forthcoming energy analysis in the fuzzy regime gives rise to a quantity with the dimension of mass, which we define to be the *characteristic mass*,  $m_c$ , given entirely by halo observables,

$$m_c^2 = \frac{\hbar^2}{RGM}. \quad (2.50)$$

As a result, one can find the relation

$$\zeta_G = \left(\frac{m_c}{m}\right)^2 R. \quad (2.51)$$

Previous works have used a slightly different definition of a characteristic mass, e.g.  $m_H$  in [Rindler-Daller and Shapiro \(2012\)](#). The comparison yields

$$m_H \equiv \frac{2}{\sqrt{3}} \frac{\hbar}{\sqrt{RGM}} = \frac{2}{\sqrt{3}} m_c. \quad (2.52)$$

The specific circumstances in the fuzzy regime can be exploited in order to gain some insight into the particle mass range. More specifically, a lower bound of  $m$  follows from requiring that the de-Broglie wavelength should be of same order as the system's size,

$$\lambda_{deB} \lesssim R, \quad (2.53)$$

where

$$\lambda_{deB} = \frac{h}{mv} \approx \frac{h}{m} \sqrt{\frac{R}{GM}}, \quad (2.54)$$

and  $R$  denotes the size of the system. The last approximation in equation (2.54) uses  $v_{vir} \approx v_{circ} = (GM/R)^{1/2}$ . Equation (2.53) yields

$$2\pi \leq \frac{m}{m_c}. \quad (2.55)$$

---

The requirement

$$\xi_G \leq \lambda_{deB}, \quad (2.56)$$

yields a weaker lower bound to  $m/m_c$  than (2.55).  $\xi_G$  can be understood from a Jeans analysis point of view as the smallest length scale for bound structures and also as the length scale of local perturbations.

In principle,  $\xi_G$  is of the same order as the size of the system  $R$  in the fuzzy regime. Therefore, it follows from (2.51) that  $m$  has to be of the same order as  $m_c$ . We want to observe the fuzzy regime, i.e. the plot range used in Chapter 5 will be limited to a fiducial particle mass range of  $2\pi \leq m/m_c \leq 3\pi$ .

There are two interpretations for our characteristic particle mass  $m_c$  in the non-interacting regime. On the one hand, it is the mass which results from requiring

$$\xi_G = \frac{\lambda_{deB}}{2\pi} = R. \quad (2.57)$$

It is precisely the fact, that all length scales in this regime are of equal order, which makes the fuzzy limit of the GP framework such challenging grounds for theory. On the other hand, just as in [Rindler-Daller and Shapiro \(2012\)](#) we find another meaning for  $m_c$  by observing that  $m = (2/\sqrt{3})m_c = m_H$  if the characteristic gravitational angular frequency

$$\Omega_{\text{grav}} = \sqrt{\pi G \bar{\rho}} \quad (2.58)$$

is equal to the angular frequency

$$\Omega_{QM} = \frac{\hbar}{mR^2} \quad (2.59)$$

of a uniformly rotating halo with mass  $M$  and angular momentum

$$L = MR^2 \Omega_{QM} \stackrel{!}{=} L_{QM} = N\hbar. \quad (2.60)$$

The background and meaning of  $L_{QM}$  will be explained in Section 3.3.

The fuzzy regime effectively amounts to the non-interacting limit ( $K_p = 0$ ). Thus, we are interested in solutions of the time-independent Gross-Pitaevskii-Poisson system without self-interaction

$$\mu\psi(\vec{r}) = -\frac{\hbar^2}{2m}\Delta\psi(\vec{r}) + m\Phi(\vec{r})\psi(\vec{r}), \quad (2.61)$$

$$\Delta\Phi(\vec{r}) = 4\pi Gm|\psi(\vec{r})|^2. \quad (2.62)$$

Mathematical physicists will recognize this system of equations as the Schrödinger - Poisson (SP) or Schrödinger - Newton equations, see for example the analytical approach to and

analysis of the system in [Tod and Moroz \(1999\)](#), provided the identification between the eigenenergy  $E$  and the chemical potential  $\mu$  as in [Chavanis \(2019b\)](#).

[Tod and Moroz \(1999\)](#) assume without loss of generality that  $\psi$  is real and introduce the real functions  $S$  and  $V$  by setting<sup>9</sup>

$$\psi = \left( \frac{\hbar^2}{8\pi G m^3} \right)^{1/2} S, \quad E - m\Phi = \frac{\hbar^2}{2m} V. \quad (2.63)$$

This change of variables together with the assumption of spherical symmetry yields

$$\frac{1}{r}(rS)'' = -SV \quad (2.64)$$

$$\frac{1}{r}(rV)'' = -S^2. \quad (2.65)$$

The prime denotes differentiation with respect to the spherical radial coordinate  $r$ . This system admits a specific scaling invariance. Given a solution  $(S(r), V(r))$ , for any arbitrary real  $\lambda$  there is another solution of the form

$$\hat{S}(r) = \lambda^2 S(\lambda r), \quad \hat{V}(r) = \lambda^2 V(\lambda r). \quad (2.66)$$

Their analysis yields amongst other things that there exists a discrete family of smooth, finite and normalizable solutions where the  $n$ th solution ( $n \in \mathbb{N}$ ) has a number of  $n - 1$  zeros and that the energy eigenvalues increase monotonically towards 0 with increasing  $n$ <sup>10</sup>. In the case of spherical symmetry, they note two relevant asymptotic forms: The solutions admit Taylor series expansions near  $r = 0$ ,

$$S = S_0 - \frac{1}{6} S_0 V_0 r^2 + \mathcal{O}(r^4) \quad \text{and} \quad V = V_0 - \frac{1}{6} S_0^2 r^2 + \mathcal{O}(r^4). \quad (2.67)$$

Also, assuming large  $r$ , there are solutions looking like

$$S = \frac{A}{r} e^{-kr} + \dots \quad \text{and} \quad V = -k^2 + \frac{B}{r} + \dots, \quad (2.68)$$

where  $A, B$  and  $k$  are real constants. In later Sections, they show that the bound state solutions we are looking for, have exactly these asymptotic forms.

In principle, the solution can be obtained by looking for regular and finite solutions for the variables  $\psi$  and  $\Phi$  of the SP system, since it then poses an eigenvalue problem which can be solved numerically. Following many authors like [Membrado et al. \(1989\)](#), [Kaup \(1968\)](#), [Ruffini and Bonazzola \(1969\)](#) or [Guzmán and Ureña-López \(2004\)](#), the family of numerical solutions is presented in Appendix B of [Hui et al. \(2017\)](#). They numerically calculated

<sup>9</sup>Notice that their function  $U$  has the dimension of gravitational energy and corresponds to  $m\Phi$ .

<sup>10</sup>Of course, on this and the following page, the label " $n$ " is not to be confused with the polytropic index  $n$ .

---

eigenstates of the SP system in spherical symmetry assuming isolated systems, i.e. that  $\psi, \Phi$  approach 0 as  $r$  goes to infinity and that they are regular at the origin. The scaling invariance (2.66) means that a solution level  $n$  forms a one-parameter family, characterized by the total mass  $M$ . Then the central density is given by

$$\rho_c = \left( \frac{Gm^2}{\hbar^2} \right)^3 M^4 \rho_n, \quad (2.69)$$

where the dimensionless constant  $\rho_n$  (depending on the eigenstate label  $n$ ) is calculated numerically. The densest state is the  $n = 0$  ground state from where the central density decreases with increasing level number  $n$ . The  $n = 0$  "soliton" state is a long-term attractor for fuzzy dark matter systems since according to the review [Hui et al. \(2017\)](#) excited states decay by means of dispersion of probability density to the soliton state.

The total mass  $M = Nm$  is conserved and finite, however the system in this regime has no compact support and thus has to be cut off artificially. In order to do so, one may calculate a radius which includes 99 percent of the mass. An exact mass-radius relation is given by

$$R_{99} = 9.946 \frac{\hbar^2}{GMm^2}, \quad (2.70)$$

see for example [Membrado et al. \(1989\)](#).

What does the theory of fuzzy dark matter predict in comparison to  $\Lambda$ CDM? According to [Hui et al. \(2017\)](#), the large-scale predictions of fuzzy dark matter do not differ from standard  $\Lambda$ CDM. However, as we have already mentioned in Section 1.3, fuzzy dark matter favors central cored density profiles over the  $\Lambda$ CDM cusps. Moreover, there are much less low-mass sub-halos expected than in standard  $\Lambda$ CDM theory. This has two reasons. First, fuzzy dark matter sub-halos are prone to tidal disruption due to the central density's upper bound, see equation (2.69), and due to the ability of fuzzy dark matter to tunnel through the potential barrier at the tidal radius. Secondly, the power spectrum of density perturbations is suppressed at small-scale structure compared to  $\Lambda$ CDM predictions due to the particle's large de-Broglie wavelength.

We have already established that the SP system can be solved numerically for the wavefunction  $\psi$  and the gravitational potential  $\Phi$  coupled to it. [Schive et al. \(2014b\)](#) use a function of the form

$$\rho = \rho_0 (1 + (r/c)^2)^{-8}, \quad (2.71)$$

where  $c$  denotes their core radius and  $r$  the distance from the center, in order to fit the soliton density profile. However, since the analytical approach of the following analysis described in subsequent Sections required an analytical solution we establish two toy-models, each incorporating a test function for the mass density  $\rho = m|\psi|^2$  and reduce the problem to

---

solving the Poisson equation for  $\Phi$  with given  $\rho$  in the first case or relying on global quantities in the second case.

The first toy-model is inspired by the well-known "wave-packet" of quantum physics. Thus, having the asymptotic behavior of  $S$  in (2.68) derived by [Tod and Moroz \(1999\)](#) in mind and being inspired by the Gaussian fit used in [Guzmán and Avilez \(2018\)](#) to describe a purely solitonic final configuration, we set

$$|\psi|^2 = \frac{\rho_0}{m} = \frac{\rho_c}{m} e^{-ar_s^2}. \quad (2.72)$$

This is a toy model or approximation of the density profile of an unperturbed Bose-Einstein condensed halo in spherical symmetry.  $\rho_0$  denotes the unperturbed matter density,  $\rho_c$  is the central density of the system and  $r_s$  is the radial distance in spherical coordinates. The density is distributed according to a normal distribution with

$$a = \frac{1}{2\sigma^2}, \quad (2.73)$$

where  $\sigma$  is the standard deviation of the distribution, see figure 2.1. Similar to the actual profile, this Gaussian approximation has no compact support. However, given a normal distribution's cumulative distribution function, one can infer that 99% of the mass lies within  $2.576 \sigma$ . Hence, we set the size of the system to be  $R_{99}$ ,

$$R_{99} = 2.576 \sigma. \quad (2.74)$$

The density profile is normalized,

$$\int_0^\infty \rho_c e^{-ar_s^2} 4\pi r_s^2 dr_s = M = N m, \quad (2.75)$$

which yields

$$\rho_c = \frac{Nm}{\sigma^3 (2\pi)^{3/2}}. \quad (2.76)$$

The second toy model, designed to approximate the actual "soliton" profile, is inspired by considerations of [Chavanis \(2019a\)](#). There they present an argument as to why the density profile of an ( $n = 2$ )-polytrope is a particular solution to equation (2.36) in the fuzzy limit,

$$\frac{\hbar^2}{2m^2} \Delta \left( \frac{\Delta \sqrt{\rho}}{\sqrt{\rho}} \right) = 4\pi G \rho. \quad (2.77)$$

Previous to introducing dimensionless variables and considering spherically symmetric configurations, the Lane-Emden equation, see Appendix A, takes the form

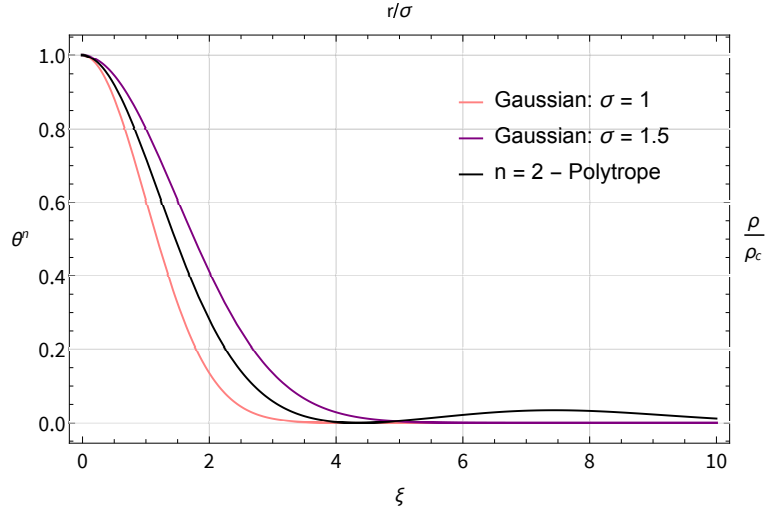


Figure 2.1: Density profile approximations: The two models' respective density profiles (2.72) and (2.81) are plotted for comparison. The two curves in shades of purple correspond to Gaussian density profiles with standard deviations  $\sigma = 1$  and  $\sigma = 1.5$  respectively. The black curve corresponds to  $\theta^2$ , the density profile in units of the central density of an ( $n = 2$ )-polytrope.

$$K_p(n+1)\Delta\rho^{1/n} = -4\pi G\rho. \quad (2.78)$$

Setting  $n = 2$  in equation (2.78), dividing it by  $\sqrt{\rho}$ , applying  $\Delta$  (the Laplacian operator) and then substituting  $\Delta\sqrt{\rho}$  on the right-hand side again through equation (2.78) itself, yields

$$\Delta\left(\frac{\Delta\sqrt{\rho}}{\sqrt{\rho}}\right) = \left(\frac{4\pi G}{3K_p}\right)^2 \rho. \quad (2.79)$$

One can see, that this equation coincides with (2.77) provided that

$$K_p = \left(\frac{2\pi G\hbar^2}{9m^2}\right)^{1/2}. \quad (2.80)$$

This result should be handled with care since equation (2.78) implies (2.79), but (2.79) does not imply (2.78) due to the nature of operations between them. Due to this non-equivalency the polytrope of index  $n = 2$  with the fixed polytropic constant in (2.80), in particular its density profile

$$\rho(r) = \rho_c\theta(\xi)^2, \quad \xi = r\left(\frac{\hbar^2}{8\pi Gm^2\rho_c}\right)^{-1/4}, \quad (2.81)$$

is a valid toy model for our purpose, but not a solution of the Gross-Pitaevskii-Poisson sys-

---

tem of equations in the fuzzy limit. Appendix A gives an overview on polytropic spheres and on the numerical approach to solving the Lane-Emden equation. Figure 2.1 shows a plot of the ( $n = 2$ ) density profile (2.81).

A closer look at the energies of a self-gravitating, non-interacting BEC with the polytropic density profile (2.81) and the energy of an ( $n = 2$ )-polytropic sphere shows the following difference, see Chavanis (2019a). We have seen that the quantum kinetic energy term is given by (2.29). Integration by parts yields

$$K_Q = \frac{\hbar^2}{4m^2} \int \nabla \rho \cdot ds - \frac{\hbar^2}{2m^2} \int \sqrt{\rho} \Delta \sqrt{\rho} dr. \quad (2.82)$$

The surface term vanishes since (2.81) indicates  $\rho'|_{r=R} \propto \theta\theta'|_{\xi=\xi_1}$  and therefore  $\rho'(R) = 0$  at the surface of the complete polytrope. By inserting (2.78) for  $n = 2$ , the quantum kinetic term takes the form

$$K_Q = 3K_p \int \rho^{3/2} dr = \frac{3}{2}U. \quad (2.83)$$

The last equality follows from (2.32), the internal energy that arises from a polytropic pressure. In other words, we know that in the fuzzy limit there is no self-interaction leading to an internal energy arising from a polytropic self-interaction pressure. Moreover, we know that the total energy of a standard polytropic sphere, i.e. a spherical system in hydrostatic equilibrium with a density profile according to the solutions of the Lane-Emden equation (see Appendix A), does not incorporate a "quantum" kinetic energy term. We have seen, that certain operations and identifications allow to associate a polytropic density profile in the form of (2.81) with a Bose-Einstein condensed system in the fuzzy limit. One could guess that the quantum kinetic term then corresponds to an internal energy of the form of (2.32) and according to Chavanis (2019a), this is true up to a factor of 3/2.

Unlike the actual "soliton" or the Gaussian model, the density profile (2.81) has a compact support, i.e. the density becomes zero at a finite radius. Furthermore unlike for example the polytrope of index  $n = 1$ , this model cannot be represented in form of an analytical expression, which seems counterproductive at first sight. However, in Section 5.2 we will see that due to already existing calculations on approximate hydrostatic equilibrium solutions for uniformly and non-uniformly rotating polytropes by Lai et al. (1993), we can exploit the sole fact that our second model is based on an ( $n = 2$ )-polytrope in order to derive global energy expressions of uniformly (in the sense of constant angular velocity  $\Omega$ ) and non-uniformly (in the sense of superposed velocity fields) rotating BEC halos.

## Chapter 3

# Superfluids, Bose-Einstein condensation and turbulence: A short excursion

The previous Chapter established a close relation between scalar-field dark matter and Bose-Einstein condensation, or alternatively superfluids, arising from their inherently similar description. As a consequence, we are dealing with an intriguing point of intersection between the astrophysics and condensed matter physics. This thesis is dedicated to the analysis of certain defects or distortions, which may occur as part of the dynamics of dark matter halos given that they consist of SFDM in the fuzzy limit. Thus, it is crucial at this point to revisit the achievements in theory and experiment of the condensed matter, superfluidity and turbulence communities in order to have a better understanding of the many phenomena familiar from these studies which may have avatars in our astrophysical setting of dark matter halos. This Chapter is dedicated to giving an overview on the strongly entangled fields of Bose-Einstein condensation, superfluidity and classical and quantum turbulence and in doing so introducing concepts and mathematical models, some of which we will apply in the course of our analysis in Chapter 5.

### 3.1 Bose-Einstein condensates

If all particles in a system occupy the same quantum ground level, theory speaks of a macroscopic phenomenon called Bose-Einstein condensation, a phenomenon which by now has been covered by lots of classic text books like [Pethick and Smith \(2008\)](#) or [Pitaevskii and Stringari \(2003\)](#). These particles are required to be bosons due to the Pauli exclusion principle. In 1995 three groups, [Bradley et al. \(1995\)](#), [Davis et al. \(1995\)](#) and [Anderson et al. \(1995\)](#),

---

separately achieved the realization of Bose-Einstein condensation in dilute alkali gases by cooling to  $nK$ -temperatures. To be more precise, Bose-Einstein condensation requires that the system's temperature falls below a certain critical temperature  $T_c$ . This critical temperature's dependency on the system's parameters follows from the simple qualitative argument that the mean interparticle distance  $\langle l \rangle = n_0^{-1/3}$  (where  $n_0$  is the number density of a homogeneous gas) becomes comparable to the de-Broglie wavelength, equation (2.1). Here, the velocity is given by the thermal velocity of the particles,  $v = \sqrt{k_B T / m}$ .

$\lambda_{deB} \sim \langle l \rangle$  yields

$$T_c \approx \frac{h^2 n_0^{2/3}}{m k_B}, \quad (3.1)$$

with  $k_B$  denoting the Boltzmann constant as usual. The experimental realization of Bose-Einstein condensation demands diluteness, i.e. number densities of typically  $10^{12}$  to  $10^{15}$  particles per  $\text{cm}^3$ , trapping of the particles by optical or magnetic tools, and cooling through techniques like evaporation or laser cooling.

Many experimental accomplishments allow us to routinely produce Bose-Einstein condensates and in doing so study these macroscopic objects with properties associated with the microscopic quantum world.

### 3.2 Association of superfluids with Bose-Einstein condensation

Fritz London suggested that the unusual properties seen in He II since its first production in 1908 are a manifestation of Bose-Einstein condensation, [London \(1938\)](#). Physicists had realized that liquid helium has two separate phases, He I and II, separated by the  $\lambda$ -point associated to a critical temperature at low pressure.  $T_\lambda = 2.17$  K in ordinary liquid  $^4\text{He}$ , whereas  $T_\lambda \approx \text{mK}$  in the rare isotope  $^3\text{He}$ . He II at  $T < T_\lambda$  showed up to that point unseen thermal and mechanical "super" properties, superconductivity and superfluidity. They saw that He II is inviscid to such an extent that it seems to "defy" gravity (referred to as the siphon effect).

To be more specific, at nonzero temperatures below the critical temperature superfluid helium consists of two fluids. Landau and Tisza's famous two-fluid model, see [Tisza \(1938\)](#) and [Donnelly \(1991\)](#), describes a system of two interpenetrating fluids. The inviscid superfluid corresponds to the macroscopic occupation of the quantum ground state and the viscid normal fluid carries the viscosity and the entropy of the entire fluid. The fraction of the superfluid density increases from zero at  $T_\lambda$  if  $T$  is lowered until the normal fluid is negligible.

---

### 3.3 Vorticity

What if we are concerned with the dynamics of superfluid helium or alternatively atomic Bose-Einstein condensates (BECs)? Besides the lack of viscosity, experiments and simulations of BECs show the appearance of so-called vortices. Since on the one hand these vortices are only the starting point of a whole theory around the nowadays fashionable subject of quantum turbulence and on the other hand our specific analysis in following Chapters includes vortex formation in astrophysical sized rotating BECs, we will go into detail on what essential role quantum vortices play.

[Tsatsos et al. \(2016\)](#) and [Barenghi et al. \(2014\)](#) give excellent reviews on superfluid and quantum turbulence and especially on how the fact that rotated BECs experience quantized vorticity crucially shapes their turbulent behaviour. If rotation was introduced, these systems would show a peculiar response. Below the critical temperature, they stand still and can only rotate by threading themselves with quantized vortex lines. Their visualizations resemble mini-tornadoes. These appear as stable topological excitations of the ground state whereas in classical fluids, there are no long-lived thin vortices. In that sense, the mathematical ideals of normal viscous fluids become real in atomic BECs. As a consequence, the vortex line density  $\mathcal{L}$ , the vortex length per unit volume, is an important observable characteristic. Also, the fact that vorticity manifests itself as line singularities, which have a fixed circulation, results in a length scale non-existent in classical fluid dynamics: the mean vortex separation  $l$ . We would like to stress that indeed the quantized circulation (3.7) itself causes this new length scale  $l$ .

[Tsatsos et al. \(2016\)](#) mention two theoretical models concerning superfluids and BECs under rotation. Meanwhile [Barenghi et al. \(2014\)](#) divide the description into three scale levels. At length scales much greater than the mean vortex separation  $l$ , models do not distinguish between individual vortex lines and consider a vortex line continuum.

The intermediate level where individual vortex lines are essential, however at length scales far away from the vortex core, three dimensional vortex dynamics is well-described by the vortex filament model of [Schwarz \(1985\)](#). This Biot-Savart model describes the velocity field by the vortex motion. The vortex lines are represented by space curves  $c = c(\tau, t)$  of circulation  $\kappa$ . The curves are parameterized by the arc-length  $\tau$  and the time  $t$ . As a starting point, the velocity is written as the rotation of a vector potential

$$\vec{v}_{ic} = \vec{\nabla} \times \vec{A}. \quad (3.2)$$

As a consequence and completely analogous to the description of magnetic fields, this formulation involves a self-induced velocity along the curve  $c$ ,

---


$$\vec{v}_c(\vec{c}, t) = \frac{\kappa}{4\pi} \int_{\mathcal{L}} \frac{\vec{r} - \vec{c}}{|\vec{r} - \vec{c}|^3} \times d\vec{r}. \quad (3.3)$$

Since the velocity is a rotation field by relation (3.2), its divergence vanishes and thus the velocity is inherently incompressible. A more general field should, according to the Helmholtz decomposition, incorporate two parts,

$$\vec{v} = \vec{v}_{ic} + \vec{v}_{ir}, \quad (3.4)$$

an incompressible velocity field  $\vec{v}_{ic}$  given by the Biot-Savart model and an irrotational part  $\vec{v}_{ir}$ . In simulations and computations based on this model by Schwarz the final configuration is entirely determined by the cell geometry, flow parameters and the initial vortex distribution. The drawbacks of this formulation are that vortex-vortex interactions, such as reconnections (see Section 3.4) need to be inserted ad hoc since they do not arise naturally and that it assumes that vortices have infinitesimally small cores.

Finally, even at the most microscopic level, where length scales can be comparable to the vortex core size  $s$  and corresponding phenomena must be accounted for, the Gross-Pitaevskii approximation (Pitaevskii (1961) and Gross (1961)) for a weakly interacting Bose gas specifically designed to describe quantized vorticity is the most commonly applied model in the BEC community. It is a mean-field theory based on total condensation, describing a many-body system by one state  $\psi(\vec{r}, t)$ . For an infinite number of particles and ground state condensation at  $T = 0$ , the Gross-Pitaevskii equation is exact. In contrast to the previous Biot-Savart model, solutions to the fundamental Gross-Pitaevskii equation can account for many phenomena in the context of quantum turbulence like vortex reconnections. From the experimental point of view the time-dependant Gross-Pitaevskii equation for a system of  $N$  bosons with particle mass  $m$  reads

$$i\hbar \frac{\partial \psi(\vec{r}, t)}{\partial t} = \left( -\frac{\hbar^2}{2m} \Delta + V_{\text{trap}} + g|\psi(\vec{r}, t)|^2 \right) \psi(\vec{r}, t). \quad (3.5)$$

This differential equation is equivalent to the model (2.7) and (2.8), we have introduced in Section 2.1 in order to describe an astrophysical Bose-Einstein condensed dark matter halo, except for the external potential  $V_{\text{trap}}(\vec{r}, t)$  (spatial confinement) in the place of the gravitational potential term in equation (2.7) coupled to the Poisson equation, which we will use in the context of our analysis. In general the trapping potential depends on the experimental setup. Obviously, all considerations like for example the normalization of the complex-valued wavefunction  $\psi$  or the Madelung transformation made in Section 2.1 apply equally

---

to equation (3.5). This transformation yields

$$\frac{\partial \vec{v}}{\partial t} = -\frac{1}{m\rho} \vec{\nabla} p - \vec{\nabla} \left( \frac{v^2}{2} \right) + \frac{1}{m} \vec{\nabla} \left( \frac{\hbar^2}{2m\sqrt{\rho}} \vec{\nabla}^2 \sqrt{\rho} \right) - \frac{1}{m} \vec{\nabla} V_{\text{trap}}, \quad (3.6)$$

where  $p = \rho^2 g/2$ . The classical limit  $\hbar \rightarrow 0$  of this differential equation is identical to the dissipation-free Navier-Stokes equation describing an irrotational fluid.

We assume a zero-viscosity fluid, a superfluid in other words, to be dissipation free and hence possess a conservative velocity field, i.e. a gradient flow  $\vec{v} \propto \vec{\nabla} S$ , which implies irrotationality, i.e.  $\omega = \vec{\nabla} \times \vec{v} = 0$ . Indeed, the Madelung transformation of the Gross-Pitaevskii equation implies an identification of the velocity in the form of relation (2.16). However, it is only at first sight, that the formulation leaves no room for fluid vorticity. Wherever the fluid mass density  $\rho = m|\psi|^2$  vanishes, the phase  $S$  and hence the  $\vec{v}$  become ill-defined. The implication of irrotationality would only hold true if the phase function  $S$  had continuous first and second derivatives everywhere. However, notice that this would not be the case if there was a vortex line at some loci along which  $\vec{v}$  diverges. It turns out that the phase function along vortex lines has non-trivial winding and hence the vorticity there is non-vanishing: Since the wavefunction is required to be single-valued, a circulation along a contour  $C$  enclosing a vortex singularity may not change  $\psi$ . Hence,  $S$  can vary at most by  $d2\pi$ , where  $d$  is the winding number, also called the vortex-charge. As a consequence, this circulation is an integer multiple of the quantum of circulation  $\kappa = h/m$ ,

$$\Gamma = \oint_C d\vec{r} \cdot \vec{v} = d \frac{2\pi\hbar}{m} = d \frac{h}{m}. \quad (3.7)$$

Hui et al. (2020) emphasize that vortices require that the real as well as the imaginary part of  $\psi$  vanishes. In an astrophysical context, where we are dealing with dark matter halos of finite size, they expect so-called vortex rings or loops.

One of the strengths of the Gross-Pitaevskii model is that it admits vortex solutions of its quantum mechanical equations of motion obeying the quantization condition (3.7). The wavefunction of an axial symmetric vortex aligned with the  $z$ -direction at the origin in cylindrical coordinates is a stationary solution and has the form

$$\psi(\vec{r}) = \psi(r, z, \phi) = |\psi|(r, z) e^{id\phi}. \quad (3.8)$$

The velocity field around this vortex has a form given by the Madelung transformation,

$$\vec{v} = \frac{\hbar}{m} \vec{\nabla} S = \frac{\hbar}{m} \frac{1}{r} \frac{\partial S}{\partial \phi} \vec{\phi} = \frac{\hbar}{m} \frac{d}{r} \vec{\phi}, \quad (3.9)$$

is directed along the azimuthal direction and is irrotational for  $r \neq 0$ . It turns out that the

---

above vortex wavefunction is an angular momentum eigenstate, where the angular momentum's  $z$ -component is given by  $l_z = d\hbar$  and thus yields the total angular momentum

$$L_z = dN\hbar \equiv dL_{QM} . \quad (3.10)$$

$L_{QM}$  denotes the angular momentum required to sustain a singly-charged (or singly-quantized) vortex line. Following [Rindler-Daller and Shapiro \(2012\)](#), we will use the vortex ansatz in cylindrical coordinates  $(r, \phi, z)$

$$w(r, \phi) = |w|(r)e^{id\phi}, \quad (3.11)$$

with amplitude<sup>11</sup>

$$|w|(r) = \begin{cases} 1 & \text{for } r \geq s, \\ C_n \left(\frac{r}{s}\right)^d & \text{otherwise,} \end{cases} \quad (3.12)$$

in the calculations of Sections 5.1 and 5.2. This ansatz corresponds to an axisymmetric,  $d$ -quantized vortex along the axis of rotation (here the  $z$ -axis) with vortex core size  $s$ . The amplitude is dimensionless and the constant  $C_n$  will be given by a normalization condition.

In conclusion, within the Gross-Pitaevskii formulation a *discontinuous* velocity flow can indeed be both, inviscid and irrotational. Equation (3.9) tells us that  $\vec{v}$  diverges as  $r \rightarrow 0$ . Why does this conclusion not yield physical inconsistency? The reason has already been mentioned. The real and imaginary parts of the wavefunction must tend to zero inside the vortex core, hence the density also vanishes. Thus, we are not going to find any particles moving with infinite speed in the core.

There are many perceptions or perspectives on such a vortex. It can be seen as a defect, perturbation or topological excitation with a higher energy than the quantum ground state. If seen as the latter, it has been shown that the vortex energy is proportional to  $d^2$  (see [Tsatsos et al. \(2016\)](#) and references therein). Hence, for given  $d$ ,  $d$  singly-quantized vortices in a system are energetically favored compared to one  $d$ -charged vortex. The perception of a vortex as a topological defect or perturbation yields the possibility to estimate the core diameter. In our vortex ansatz, the core size  $s$  corresponds to the cylindrical radius, where the density regains its unperturbed local value. In Sections 2.2 and 2.3 we have encountered the notion of the so-called healing length  $\xi$ , a scale over which the gas "heals" a disturbance, and have defined the gravitational healing length  $\xi_G$  in the fuzzy regime of the Gross-Pitaevskii-Poisson framework. Since the vortex can be identified as a local disturbance of the density, one expects its extension at equilibrium to be of the order of the healing length or gravitational healing length respectively, i.e.  $s \approx \xi_G$ . By way of equations (2.49) and (2.70), this implies  $s \leq R_{99}$ , i.e. the vortex could take up almost the entire halo in the fuzzy regime.

---

<sup>11</sup>The index  $n$  in  $C_n$  refers to "normalization" and is not to be confused with the polytropic index.

---

### 3.4 Quantum turbulence

Vortex lines in BECs are the fundamental constituents of so-called quantum turbulence. In some respects it is important to distinguish between what is often called superfluid or helium turbulence in Bose-Einstein condensed liquid helium and turbulence in trapped, dilute atomic BECs, often referred to as quantum turbulence, reviewed in [Barenghi et al. \(2014\)](#) and [Tsatsos et al. \(2016\)](#) respectively.

What is turbulence? It can be described as disordered and irregular flow associated with a huge number of simultaneously excited degrees of freedom which interact nonlinearly. In order to prevent this definition from being too generic, it is reasonable to restrict it to systems whose description includes the  $(\vec{v} \cdot \vec{\nabla})\vec{v}$  nonlinearity appearing in the Navier-Stokes equation or equivalently in its skeleton, the Euler equation.

Classical turbulence involving eddies, which exchange energy, is built on a mathematical description given by the Navier-stokes equation

$$\frac{\partial \vec{v}}{\partial t} + (\vec{v} \cdot \vec{\nabla})\vec{v} = -\frac{1}{\rho}\vec{\nabla}p + \nu\vec{\nabla}^2\vec{v} + \vec{g}, \quad (3.13)$$

describing an incompressible (solenoidal) fluid with constant density, where  $\nu$  is the kinematic viscosity and  $\vec{g}$  is a placeholder for external forces. The transition between laminar and turbulent flows requires that the dimensionless Reynolds number  $Re = vD/\nu$  ( $v$  being the average velocity fluctuation), estimating the ratio between nonlinear and viscous forces, becomes sufficiently large at the outer scale  $D$ . If you constantly input energy at large scales and the system dissipates energy at same rates at small scales, you can achieve a steady state. At intermediate scales, called inertial range, flow patterns show self-similar behaviour, in which energy is transferred from large to small eddies in the form of a cascade. According to [Kolmogorov \(1941\)](#) the distribution of kinetic energy over different scales is such that the energy spectrum for steady, isotropic, incompressible turbulence (given inertial range scales) has the form

$$E_k = C\epsilon_k^{2/3}k^{-5/3}, \quad (3.14)$$

where  $k = 2\pi/r$  is the wavenumber and  $r$  indicates spatial distance.

Numerical simulations and a variety of experimental setups of liquid helium or atomic BECs have shown that there exist many manifestations of helium or quantum turbulence like disordered configurations of vortex lines. These configurations can be either laminar, e.g. vortex lattices in rotation, or turbulent, e.g. tangled vortex lines. What characterizes quantum turbulence is less the superfluidity of a turbulent system but more the property of quantized vorticity. Vorticity is unconstrained and continuous in classical turbulent systems and quantized and discrete in quantum systems. As a consequence, the building blocks of the latter, namely vortices, are well-defined. The fact that turbulence decays if left unforced

---

in these systems despite zero viscosity in superfluids can only be explained by discrete vortex lines. Hence, quantum turbulence requires a description by a macroscopic wavefunction.

[Tsatsos et al. \(2016\)](#) promote questions like “How many degrees of freedom?” or “What number of vortices is needed for the emergence of turbulence or even Kolmogorov scaling?”. These are challenging open questions in the field of quantum turbulence.

Quantum turbulence is often associated with the motion and interactions of vortices, which are plenty. Vortex line tangles can exhibit partial spatial polarization by organizing into vortex bundles. In doing so, quasiclassical or Kolmogorov turbulence can emerge in a certain inertial range, where energy is transferred from big to small bundles. However, [Tsatsos et al. \(2016\)](#) highlight in their Subsection 3.2 that the scaling of the energy spectrum characterizing the type of turbulence strongly depends on how the superfluid is driven. For thermally driven superfluids (e.g. through heat fluxes) the energy spectrum exhibits low levels at small  $k$ , scales as  $k^{-1}$  at large  $k$  and forms a “bump” in between. On the other hand, if the superfluid is driven by a mechanically-driven normal fluid component, a Kolmogorov-like scale is recovered with large-scale flows due to large-scale vortex line polarization. Vortices in trapped BECs show rich dynamics. There are for example quantum vortex reconnections, where vortices interact, approach, connect and exchange tails. This phenomenon contributes to a great extent to the energy transfer between vortices of different scales. In two dimensions, there are models which predict annihilation of oppositely charged vortex lines and vortex clustering.

What about the lowest temperature limit and the smallest length scales below the mean inter-vortex distance? Vortices can experience helical perturbations referred to as Kelvin waves. At higher temperatures friction effects damp these Kelvin waves and smooth the individual vortex lines. However, in this regime the interaction of Kelvin waves yields shorter and shorter wavelengths in a process called Kelvin-wave cascade. Rapidly rotating Kelvin waves yield phonon emission if the wavelength is short enough. Hence, quantum turbulence has an acoustic (not viscous) sink explaining how its decay is based on discrete vorticity. One could also say that vortices at the smallest scales decay eventually into sound.

There has been found another kind of turbulence, namely ultraquantum turbulence addressing large vortex tangles characterized by a lack of large-scale energy flows and a high degree of randomness. [Tsatsos et al. \(2016\)](#) state that ultraquantum turbulence is more likely to appear in trapped atomic BECs.

## Chapter 4

# Rotating configurations of Bose-Einstein condensed dark matter halos

We have seen what extraordinary phenomena manifest themselves when Bose-Einstein condensates are subject to rotation. The following Chapter will be dedicated to analyse whether and under what conditions vortex creation in self-gravitating BEC- dark matter halos in the fuzzy regime rotating with *constant* angular velocity  $\Omega$  is energetically favored. This analysis requires a complete model of the halo, i.e. a geometry, density and velocity profile consistent with the demands of the Gross-Pitaevskii framework. In Section 2.3, we have already indicated that our analysis incorporates two possible approximations to the amplitude squared of the Gross-Pitaevskii-Poisson system's stationary solution for the wavefunction  $|\psi|^2$  or equivalently approximations to the density profile  $\rho(\vec{r}) = m|\psi(\vec{r})|^2$  in the fuzzy limit<sup>12</sup>. Remember that we made an ansatz for the wavefunction of the form  $\psi = |\psi|e^{iS}$ . By doing so, the velocity information of the dark matter halo is given by the real phase function  $S(t, \vec{r})$  since  $\vec{v} = \hbar \vec{\nabla} S / m$ .

From a cosmological point of view, we expect that angular momentum plays a crucial role in DM-halo physics. The large-scale structure of the universe causes tidal torques, which give halos in their early phases angular momentum. BEC-DM is supposed to behave similarly to standard CDM over scales much larger than the de-Broglie wavelength. Hence, following [Rindler-Daller and Shapiro \(2012\)](#), we will make use of the dimensionless ratio

$$\lambda = \frac{L|E|^{1/2}}{GM^{5/2}}, \quad (4.1)$$

---

<sup>12</sup>Have in mind, that the Gross-Pitaevskii-Poisson system as a matter of fact demands a set of solutions  $(\psi, \Phi)$ .

---

where  $E$  denotes the total energy and  $M$  the total mass of the halo. Cosmological N-Body numerical simulations use this spin-parameter in order to quantify the degree of rotational support of a halo with net angular momentum  $L$ . Typical values for  $\lambda$  are in the range  $[0.01, 0.1]$ , for example found by [Antonuccio-Delogu et al. \(2010\)](#). As a result, our halo model will have a bulk angular momentum, which will eventually be set by the  $\lambda$ -spin parameter by associating it to the angular momentum provided by tidal torquing. The halo will hence experience superfluid currents for  $\Omega \neq 0$ , which will manifest themselves by a non-trivial phase function  $S$ .

Now the key point is that we study halo configurations in equilibrium. In other words, we consider stationary solutions given by (2.24) and (2.25), i.e. quantum states with time-independent observables which are eigenstates of the Hamiltonian, and add the distinction between different reference frames to our considerations. Rotating configurations at constant  $\Omega$  in the rest frame of the halo correspond to stationary solutions in the corotating frame. In this corotating frame, the bulk velocity is given by

$$\vec{v}' = \vec{v} - \vec{\Omega} \times \vec{r}, \quad (4.2)$$

where primed quantities and variables denote those in the corotating frame. The angular momentum is given by

$$\vec{L}' = -i\hbar\vec{r}' \times \vec{\nabla}' \quad (4.3)$$

and the GP energy functional in the fuzzy limit ( $g = 0$ ) is

$$E'[\psi'] = \int_V \left[ \frac{\hbar^2}{2m} |\vec{\nabla}' \psi'|^2 + \frac{m}{2} \Phi |\psi'|^2 + i\hbar \psi'^* \vec{\nabla}' \psi' \cdot (\vec{\Omega} \times \vec{r}') \right] d^3r'. \quad (4.4)$$

This expression for the energy in the corotating frame will be used in our analysis of Chapter 5.

Our investigation is based upon two models:

- **Model A: The Gaussian sphere.** This model approximates the halo as a sphere with radius  $R$  rotating with constant angular velocity  $\vec{\Omega} = (0, 0, \Omega)$  about the z-axis. The density profile is chosen according to the first density model introduced in 2.3 equation (2.72),

$$|\psi|^2 = \frac{\rho_0}{m} = \frac{\rho_c}{m} e^{-ar_s^2}. \quad (4.5)$$

This spherical halo includes no internal velocity field in addition to the bulk rotation

---

$\vec{\Omega} \times \vec{r}$  in the rest frame, hence the sphere shows no net velocity in the corotating frame

$$\vec{v}' = \vec{\Omega} \times \vec{r} - \vec{\Omega} \times \vec{r} = 0 = \frac{\hbar}{m} \vec{\nabla} S' . \quad (4.6)$$

- Model B: The irrotational Riemann-S ellipsoid. [Lai et al. \(1993\)](#) provide us with the foundation of this model and thereby with the opportunity to pursue the question of vortex formation in rotating BEC halos in a more self-consistent way. They developed compressible generalizations of [Chandrasekhar \(1969\)](#)'s figures of equilibrium using an energy variational method. Especially, their compressible version of the so-called irrotational Riemann-S ellipsoid offers a way to account for both, the superfluid's compressibility, and the irrotationality of the velocity flow in the rest frame by superposing an internal velocity field on top of the uniform rotation. The geometry of this non-axisymmetric object modeling our BEC- dark matter halo is given by its three semi-axes  $(a_1, a_2, a_3)$  along  $(x, y, z)$ . It is a classical figure of rotation perfectly suited for our purpose. Without loss of generality, we align the axis of rotation, about which the ellipsoid rotates uniformly with angular velocity  $\Omega$ , along the z-axis. [Rindler-Daller and Shapiro \(2012\)](#) applied the irrotational Riemann-S ellipsoid in their study of rotating BEC halos in the Thomas-Fermi regime, in which the density profile is an  $(n = 1)$ -polytrope. Since we have already established the fact, that the  $(n = 2)$ -polytropic density profile is an appropriate approximation to the actual "soliton" in Section 2.3, we paved the way for applying the results of [Lai et al. \(1993\)](#) for  $(n = 2)$  with some additional considerations regarding the quantum kinetic energy  $K_Q$ . This way, we show that the irrotational Riemann-S ellipsoid is a useful description for BEC-DM halos, whether they be in the Thomas-Fermi or in the fuzzy regime.

## 4.1 Compressible ellipsoidal equilibrium figures

This Section is dedicated to give more insight into the theoretical framework which halo model B is based on and to present the essential strategies, relations and results on compressible figures of equilibrium of the study of [Lai et al. \(1993\)](#) in order to lay the groundwork for next Chapter's calculations.

In his book on "Ellipsoidal figures of equilibrium", the modern hero of astrophysics, Subrahmanyan [Chandrasekhar \(1969\)](#), reevaluated and heavily expanded studies on the gravitational equilibrium of homogeneous uniformly rotating masses and thereby offered the astrophysical community a strong and lasting asset. He sets the stage for his study with a short historical recap starting with Newton's considerations on the effect of rotation on the figure of the earth, followed by Maclaurin who generalized existing results to large ellipticity. Nearly a century later, Jacobi concluded that an ellipsoid with three unequal axes can

---

be, too, a figure of equilibrium. This conclusion implied a huge leap forward since by that time it was consensus that equilibrium requires the two equatorial axes to be equal. Important works were done by Dirichlet and Dedekind inspired by the question: What conditions allow a configuration to have, at all times, an ellipsoidal shape and a motion in the inertial frame governed by a function that is linear in the coordinates?

Riemann then postulated that the most general motion under the above requirement formulated by Dirichlet compatible with an ellipsoidal equilibrium figure is the sum of a uniform rotation with angular velocity  $\vec{\Omega}$  and internal motions with uniform vorticity  $\vec{\zeta}'$ . More precisely, an ellipsoidal equilibrium figure was considered as a homogeneous fluid mass which maintains its ellipsoidal configuration under rotation and under its own gravity at all times. Chandrasekhar (1969) then revisits Riemann's theorem stating that equilibrium demands either that  $\vec{\Omega}$  and  $\vec{\zeta}'$  are both oriented along one of the principal axes, thereby being parallel, or the directions of  $\vec{\Omega}$  and  $\vec{\zeta}'$  lie in one principal plane, while not being parallel. As a result, we must distinguish between two different configuration types among the Riemann ellipsoids. It turns out that in the case of parallel  $\vec{\Omega}$  and  $\vec{\zeta}'$ , we encounter a type of ellipsoids called S-type ellipsoids or Riemann-S ellipsoids, which may be arranged in linear sequences. The latter case of non-parallel  $\vec{\Omega}$  and  $\vec{\zeta}'$  leads to equilibrium figures of completely different structures. Given S-type ellipsoids one can define Riemann sequences as sequences along which the fraction

$$f_R = \frac{\zeta'}{\Omega},$$

where  $\Omega = |\vec{\Omega}|$  and  $\zeta' = |\vec{\zeta}'|$ , is constant. Two famous sequences, the Jacobian and Dedekind sequences, are hereby equal to  $f_R = 0$  and  $f_R = \pm\infty$  Riemann sequences, respectively.

Since we are not going to model our BEC halo as a homogeneous ellipsoidal body but in the case of model B as an ellipsoid comprising an ( $n = 2$ )-polytropic density profile, the analytic studies of Lai et al. (1993) on compressible generalizations of incompressible classical figures like Maclaurin spheroids, Jacobi and Dedekind ellipsoids and especially Riemann ellipsoids are essential to our calculations. An incompressible flow describes a fluid flow whose density is constant within a so-called fluid parcel, i.e. an infinitesimally small volume moving with the bulk velocity. It can be shown that incompressibility also implies that the divergence of the flow velocity vanishes. Less essential to our calculations but according to them most significant are their results concerning the stability of Roche, Darwin and Roche-Riemann binaries.

Motivated by the lack of adequate analytical models for the equilibrium structure of stars perturbed by tidal fields or rotation by that time, Lai et al. (1993) used an ellipsoidal energy variational method in order to meet the demand of numerical work on compressible fluids for approximate analytical solutions. Their method involves the total (not necessarily equilibrium) energy of a self-gravitating, isolated and steady fluid system,

---


$$E = E[\rho(\vec{r}), \vec{v}(\vec{r}); M, S, L, \dots], \quad (4.7)$$

where conserved global quantities like the total mass  $M$ , the entropy  $S$  and the total angular momentum  $L$  specify the system and  $\rho(\vec{r})$  and  $\vec{v}(\vec{r})$  are the fluid density and velocity, respectively. Finding an equilibrium configuration amounts to extremizing (4.7) with respect to all variations of  $\rho(\vec{r})$  and  $\vec{v}(\vec{r})$  which do not change the conserved quantities. Since this implies an infinite number of degrees of freedom, [Lai et al. \(1993\)](#)'s approach is to replace them by a set of parameters  $\alpha_1, \alpha_2, \dots$  based on simplifying assumptions so that

$$E = E[\alpha_1, \alpha_2, \dots; M, S, L, \dots]. \quad (4.8)$$

As a result,

$$\frac{\partial E}{\partial \alpha_i} = 0, \quad i = 1, 2, 3, \dots \quad (4.9)$$

yield the equilibrium conditions.

In a next step, [Lai et al. \(1993\)](#) consider density and pressure profiles according to those of a polytrope of index  $n$ , see Appendix A. First, they consider spherical, i.e. non-rotating, polytropic systems, with mass  $M$  and radius  $R$  (not necessarily the equilibrium radius). Once the density profile and the total mass are given, the system is either characterized by the radius  $R$  or equivalently by the central density

$$\rho_c = \frac{\xi_1}{4\pi|\theta'_1|} \frac{M}{R^3}. \quad (4.10)$$

$\xi$ <sup>13</sup> and  $\theta$ , defined in Appendix A, are the commonly used dimensionless variables in the context of the Lane-Emden equation. In the spherical (non-rotating) case the total energy is given by

$$E(\rho_c; M) = U + W, \quad (4.11)$$

with the internal energy

$$U = k_1 K_p \rho_c^{1/n} M \quad (4.12)$$

and the gravitational potential energy

$$W = -\frac{3}{5-n} \frac{GM^2}{R} = -k_2 \rho_c^{1/3} GM^{5/3}, \quad (4.13)$$

---

<sup>13</sup>Notice that unfortunately both, the dimensionless radius of the Lane-Emden equation as well as the uniform vorticity of the internal motions in a Riemann-S ellipsoid, are denoted  $\xi$  in the common literature.

---

where the constants  $k_1$  and  $k_2$  are defined as

$$k_1 \equiv \frac{n(n+1)}{5-n} \bar{\xi}_1 |\theta'_1|, \quad (4.14)$$

$$k_2 \equiv \frac{3}{5-n} \left( \frac{4\pi |\theta'_1|}{\bar{\xi}_1} \right)^{1/3}. \quad (4.15)$$

Now, there are two crucial assumptions [Lai et al. \(1993\)](#) make in order to arrive from a spherical non-rotating configuration to the energy of a rotating ellipsoidal polytrope, referred to by them as the ellipsoidal approximation:

- The isodensity surfaces are assumed to be self-similar ellipsoids. Thereby the three principal axes  $a_1$ ,  $a_2$  and  $a_3$  of the outer surface where  $\rho = P = 0$ , or equivalently the eccentricities given by

$$e_1 = \sqrt{1 - (a_2/a_1)^2} \quad \text{and} \quad e_2 = \sqrt{1 - (a_3/a_1)^2}, \quad (4.16)$$

solely specify the geometry.

- The density profile  $\rho(m)$  and specific internal energy profile  $u(m)$ , where  $m$  denotes the mass inside an isodensity surface, are set identical to those of a spherical polytrope of same  $n$ ,  $K_p$  and volume, i.e. whose radius is the mean radius

$$R = (a_1 a_2 a_3)^{1/3}. \quad (4.17)$$

In the incompressible limit, i.e.  $n = 0$ , these approximations turn into strictly valid statements and their method yields exact solutions.

Amongst a variety of other classical objects [Lai et al. \(1993\)](#) treat compressible Riemann-S ellipsoids (triaxial structures) by incorporating the presence of non-uniform rotation. The goal is to develop an expression for the total energy in the ellipsoidal approximation.

As part of the ellipsoidal approximation it was assumed that the specific internal energy profile  $u(m)$  of our rotating configuration is the same as that of the corresponding spherical non-rotating polytrope with same volume or equivalently same central density. Hence, the total internal energy  $U$  is given by (4.12) and therefore independent of the system's geometry.

What about the gravitational potential energy  $W$ ? [Lai et al. \(1993\)](#) compare  $W$  of a homogeneous rotating triaxial ellipsoid (e.g. given by [Chandrasekhar \(1969\)](#)),

$$W(\text{Ellipsoid}) = -\frac{3}{5} \frac{GM^2}{R} f, \quad (4.18)$$

where  $R$  is given by (4.17) and  $f$  is the essential dimensionless ratio in this context given by

$$f = \frac{1}{2} \frac{A_1 a_1^2 + A_2 a_2^2 + A_3 a_3^2}{(a_1 a_2 a_3)^{2/3}}, \quad (4.19)$$

to  $W$  of a sphere of constant density,

$$W(\text{Sphere}) = -\frac{3}{5} \frac{GM^2}{R}. \quad (4.20)$$

One can observe, that these two expressions for the gravitational potential energy differ by the multiplier  $f$ . Its dimensionless coefficients  $A_i$  are given in [Chandrasekhar \(1969\)](#) and can be written in terms of the axis ratios:

$$A_1 = 2 \frac{a_2 a_3}{a_1 a_1} \frac{F(\theta, \phi) - E(\theta, \phi)}{\sin^3 \phi \sin^2 \theta} \quad (4.21)$$

$$A_2 = 2 \frac{a_2 a_3}{a_1 a_1} \frac{E(\theta, \phi) - F(\theta, \phi) \cos^2 \theta - (a_3/a_2) \sin^2 \theta \sin \phi}{\sin^3 \phi \sin^2 \theta \cos^2 \theta} \quad (4.22)$$

$$A_3 = 2 \frac{a_2 a_3}{a_1 a_1} \frac{(a_2/a_3) \sin \phi - E(\theta, \phi)}{\sin^3 \phi \sin^2 \theta}, \quad (4.23)$$

where  $\cos \phi = a_3/a_1$ ,  $\sin \theta = \sqrt{\frac{1-(a_2/a_1)^2}{1-(a_3/a_1)^2}}$  and the standard incomplete elliptic integrals are given by

$$E(\theta, \phi) = \int_0^\phi (1 - \sin^2 \theta \sin^2 \phi')^{1/2} d\phi', \quad (4.24)$$

$$F(\theta, \phi) = \int_0^\phi (1 - \sin^2 \theta \sin^2 \phi')^{-1/2} d\phi'. \quad (4.25)$$

The ellipticity of these equilibrium figures is a pure result of rotation reflected by the factor  $f$ . Based on Newton's theorem stating that an ellipsoidal shell of constant density has a constant gravitational potential inside (see [Chandrasekhar \(1969\)](#)) and the ellipsoidal approximation, [Lai et al. \(1993\)](#) conclude that the gravitational potential  $W$  of a spherical polytrope and the one of a homogeneous sphere are equally modified by rotation. Hence, the gravitational potential energy of our compressible Riemann-S ellipsoid is given by

$$W = -\frac{3}{5-n} \frac{GM^2}{R} f = -k_2 \rho_c^{1/3} GM^{5/3} f. \quad (4.26)$$

What remains is the kinetic energy of rotation  $T$  which requires more elaborate groundwork. First, one starts with an object that rotates rigidly with constant angular velocity  $\vec{\Omega} = \Omega \vec{e}_3$ . Then one superposes an internal velocity field with uniform vorticity parallel to  $\vec{\Omega}$ ,

$$\zeta' \equiv (\vec{\nabla}' \times \vec{v}') \cdot \vec{e}_3, \quad (4.27)$$

---

specified by the requirement that the resulting velocity vector at any point shall be tangent to the isodensity surface at that point. From that it follows that the fluid velocity in the rest frame can be written as

$$\vec{v} = \vec{v}' + \vec{\Omega} \times \vec{r}, \quad (4.28)$$

where

$$\vec{v}' = -\frac{a_1^2}{a_1^2 + a_2^2} \zeta' y \vec{e}_1 + \frac{a_2^2}{a_1^2 + a_2^2} \zeta' x \vec{e}_2 \quad (4.29)$$

in Cartesian coordinates  $(x, y, z)$ . In addition, there is a relation between the angular frequency of the internal motions  $\Lambda$  and the vorticity,

$$\zeta' = -\frac{a_1^2 + a_2^2}{a_1 a_2} \Lambda. \quad (4.30)$$

By means of the above relations [Lai et al. \(1993\)](#) find for the angular momentum  $\vec{L}$  and rotational kinetic energy  $T$ ,

$$\vec{L} \equiv \int \vec{r} \times \vec{v} \rho d^3r = (I\Omega - \frac{2}{5} \kappa_n M a_1 a_2 \Lambda) \vec{e}_3 \quad (4.31)$$

and

$$T \equiv \frac{1}{2} \int \vec{v} \cdot \vec{v} \rho d^3r = \frac{\kappa_n}{20} M ((a_1 - a_2)^2 (\Omega + \Lambda)^2 + (a_1 + a_2)^2 (\Omega - \Lambda)^2), \quad (4.32)$$

respectively. The moment of inertia  $I$  is given by

$$I = \frac{\kappa_n}{5} M (a_1^2 + a_2^2) \quad (4.33)$$

and the definition of the constant  $\kappa_n$  and its values for  $n \in (1, 2)$  can be found in equation [\(A.13\)](#). In Chapter 3, we have sufficiently established that a Bose-Einstein condensed halo described by the Gross-Pitaevskii-Poisson framework is in general irrotational with an exception wherever you find a vortex line. It turns out that the construction of Riemann-S ellipsoids allows to guarantee irrotationality given a certain choice of the parameter  $f_R$ . This can be shown by introducing the circulation along the equator,

$$\Gamma_{\text{equator}} \equiv \oint_{\text{equator}} \vec{v} \cdot d\vec{l} = \pi(2 + f_R) a_1 a_2 \Omega, \quad (4.34)$$

and the vorticity in the rest frame

$$\zeta \equiv (\vec{\nabla} \times \vec{v}) \cdot \vec{e}_3 = (2 + f_R) \Omega. \quad (4.35)$$

---

Along the so-called *irrotational* Riemann-S sequence the fraction  $f_R = -2$  yielding  $\xi = \Gamma_{\text{equator}} = 0$ . [Rindler-Daller and Shapiro \(2012\)](#) derive the velocity field of the irrotational (i.e.  $f_R = -2$ ) Riemann-S ellipsoid for a given polytropic index  $n$  in the rotating frame,

$$\vec{v}' = 2\Omega_{\text{grav},R} \left( \frac{2B_{12}}{q_n} \right)^{1/2} (8(1 - e_1^2) + e_1^4)^{-1/2} (y, -(1 - e_1^2)x, 0), \quad (4.36)$$

and in the rest frame,

$$\vec{v} = \Omega_{\text{grav},R} \left( \frac{2B_{12}}{q_n} \right)^{1/2} (1 + 8(1 - e_1^2)/e_1^4)^{-1/2} (y, x, 0), \quad (4.37)$$

respectively, by using (4.27), (4.28), (4.29), (4.30), (4.51) and (4.48). Here we have used [Lai et al. \(1993\)](#)'s definition of the gravitational angular velocity of an ellipsoid with mean radius  $R$  given in (4.17),

$$\Omega_{\text{grav},R} := \sqrt{\pi G \bar{\rho}} = \sqrt{\frac{3GM}{4R^3}}. \quad (4.38)$$

We have plotted  $\vec{v}'/(\Omega_{\text{grav},R}l)$  and  $\vec{v}/(\Omega_{\text{grav},R}l)$ , with  $l$  denoting a quantity with dimension of length, for polytropic index ( $n = 2$ ) in figures 4.1 and 4.2. Obviously, the vorticity vanishes in the rest frame in the case of the  $f_R = -2$  irrotational sequence.

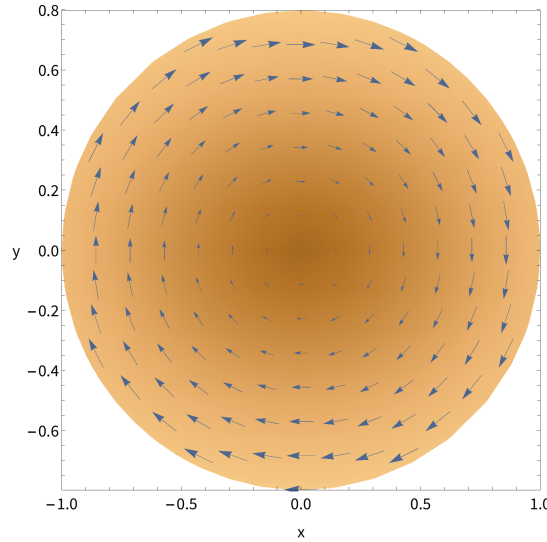


Figure 4.1: Illustrative velocity field of an ( $n = 2$ ), irrotational Riemann-S ellipsoid in the rotating frame according to equation (4.36) with eccentricities  $e_1 = 0.60246$  and  $e_2 = 0.46823$  (or  $\lambda = 0.01$ , see table 5.1).

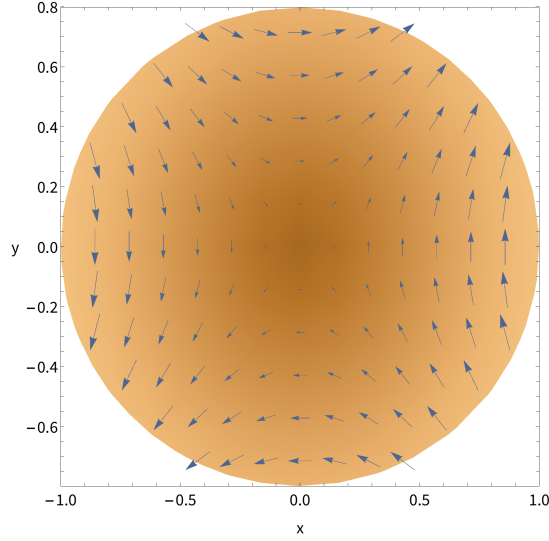


Figure 4.2: Illustrative velocity field of an ( $n = 2$ ), irrotational Riemann-S ellipsoid in the rest frame according to equation (4.37) with eccentricities  $e_1 = 0.60246$  and  $e_2 = 0.46823$  (or  $\lambda = 0.01$ , see table 5.1).

The total energy for a system with fixed  $M, L$  and  $\mathcal{C} \equiv -\kappa_n M \Gamma_{\text{equator}} / (5\pi)$ ,

$$E = E[\rho_c, \eta_1, \eta_2; M, L, \mathcal{C}] = U + T + W, \quad (4.39)$$

is obtained by summing all the individual energy terms, where

$$\eta_1 = \left(\frac{a_3}{a_1}\right)^{2/3} \quad \text{and} \quad \eta_2 = \left(\frac{a_3}{a_2}\right)^{2/3}. \quad (4.40)$$

In other words, the configuration is specified by the central density of the polytropic density profile and the axis ratios. Equilibrium now requires the conditions

$$\frac{\partial E}{\partial \rho_c} = 0, \quad (4.41)$$

$$\frac{\partial E}{\partial \eta_1} = 0 \quad \text{and} \quad (4.42)$$

$$\frac{\partial E}{\partial \eta_2} = 0. \quad (4.43)$$

The first condition yields

$$2T + W + \frac{3}{n}U = 0, \quad (4.44)$$

a virial relation taking *almost* the same form as (2.33). The hidden but crucial difference arises

from the fact that the classical theory of Riemann-S ellipsoids does not involve the quantum kinetic energy we have encountered in Section 2.1. However, we have overcome this obstacle in the course of our calculations, see Section 5.2.

Conditions (4.42) and (4.43) yield after some manipulations two equations relating  $f_R$ ,  $\tilde{\Omega}$  and the axes,

$$\left[1 + \frac{a_1^2 a_2^2}{(a_1^2 + a_2^2)^2} f_R^2\right] \tilde{\Omega} = \frac{2B_{12}}{q_n}, \quad (4.45)$$

$$q_n \frac{a_1^2 a_2^2}{a_1^2 + a_2^2} f_R \tilde{\Omega}^2 = a_1^2 a_2^2 A_{12} - a_3^2 A_3. \quad (4.46)$$

The definition of the constant  $q_n$  and its values for  $n \in (1, 2)$  can be found in equation (A.14). The dimensionless angular velocity  $\tilde{\Omega}$  is given by

$$\tilde{\Omega} = \frac{\Omega}{\Omega_{\text{grav},R}} = \frac{\Omega}{(\pi G \bar{\rho})^{1/2}}, \quad (4.47)$$

where  $\bar{\rho} \equiv 3M/(4\pi R^3)$  and  $R$  is the mean radius. In addition, Lai et al. (1993) introduce the quantities

$$A_{12} = \frac{A_1 - A_2}{a_2^2 - a_1^2} \quad \text{and} \quad B_{12} = A_2 - a_1^2 A_{12}. \quad (4.48)$$

Equilibrium requires the relations (4.45) and (4.46). One can eliminate  $\tilde{\Omega}$  between these two equations and obtains an equilibrium relation for the axis ratios along a given Riemann-S sequence ( $f_R$  fixed) that does not depend on the polytropic index  $n$ :

$$\frac{a_1^2 a_2^2}{(a_1^2 + a_2^2)^2} f_R^2 + \frac{2a_1^2 a_2^2 B_{12}}{a_3^2 A_3 - a_1^2 a_2^2 A_{12}} \frac{f_R}{a_1^2 + a_2^2} + 1 = 0 \quad (4.49)$$

or equivalently for  $f_R = -2$ , i.e. along the irrotational sequence,

$$\frac{4(a_2/a_1)^2}{(1 + (a_2/a_1)^2)^2} - \frac{4B_{12}(a_2/a_1)^2}{(a_3/a_1)^2 A_3 - (a_2/a_1)^2 \frac{A_1 - A_2}{(a_2/a_1)^2 - 1}} \frac{1}{1 + (a_2/a_1)^2} + 1 = 0. \quad (4.50)$$

In other words, in the case of equilibrium one axis ratio determines the other, thereby immediately fixing the geometry, and furthermore  $\tilde{\Omega}^2$  is given by (4.45) once  $a_2/a_1$  and  $a_3/a_1$  are known. For  $f_R = -2$ , (4.45) can be solved for  $\tilde{\Omega}$  and written as

$$\tilde{\Omega} = \left(\frac{2B_{12}}{q_n}\right)^{1/2} \left(1 + \frac{4a_1^2 a_2^2}{(a_1^2 + a_2^2)^2}\right)^{-1/2}. \quad (4.51)$$

We will see in Section 5.2 that the irrotational Riemann-S ellipsoids fulfill  $a_1 \geq a_3 \geq a_2$ , i.e. this sequence consists of prolate figures.

---

Inserting the virial relation (4.44) into the total energy (4.39) yields the total equilibrium energy

$$E_{eq} = \frac{3-n}{n} W \left( 1 - \frac{3-2n}{3-n} \frac{T}{|W|} \right). \quad (4.52)$$

Finally, there is an important relation between the radius of the non-rotating spherical polytrope of *same mass*  $M$ ,  $n$  and  $K_p$ ,

$$R_0 = \zeta_1 (\zeta_1^2 |\theta'_1|)^{-(1-n)/(3-n)} \left( \frac{M}{4\pi} \right)^{(1-n)/(3-n)} \left( \frac{(n+1)K_p}{4\pi G} \right)^{n/(3-n)}, \quad (4.53)$$

(compare with Appendix A) and the mean radius  $R = (a_1 a_2 a_3)^{1/3}$ :

$$R = R_0 \left[ f \left( 1 - 2 \frac{T}{|W|} \right) \right]^{-n/(3-n)}, \quad (4.54)$$

where  $f$  is the dimensionless factor defined in (4.19).

## Chapter 5

# Vortex formation in the fuzzy regime

Finally, the groundwork has been laid so that we can dedicate this Chapter to the main part of this thesis, the energy argument deciding whether the formation of one central vortex line in a BEC- dark matter halo *in the fuzzy regime* in the context of our simplified modelling is energetically favored or not. Our energy analysis is based on the comparison between the total energy of the system without and with a vortex in the corotating frame. To be more precise, the question will be whether the amount of angular momentum quantified by typical spin-parameter values in cosmological simulations, i.e.  $\lambda$  values in the range [0.01, 0.1], is sufficient to trigger the development of a quantum vortex in the halo. In the course of the following energy analysis the primes on variables indicating the corotating frame will be omitted except for phase functions and energies.

### 5.1 Model A: The Gaussian sphere

Within this model, the approach is to construct a wavefunction which accounts for a vortex in an otherwise unperturbed system, calculate the total energy arising from this wavefunction by means of the Gross-Pitaevskii energy functional in the fuzzy limit (4.4), identify those energy terms that arise due to the vortex and determine whether they lower or raise the total energy for given parameters of the system and the dark matter particles.

To this aim, the wavefunction  $\psi$  of the halo superfluid must be decomposed into an unperturbed and a vortex-part in the form of the product state

$$\psi = \psi_0 w = |\psi_0| |w| e^{iS'_0 + S'_1}, \quad (5.1)$$

where "0"-indices indicate variables of the unperturbed system,  $\psi_0 = |\psi_0| e^{iS'_0}$ , and the vortex is included by means of the ansatz  $w = |w| e^{iS'_1}$ . Of course, the appearance of a vortex affects the density and the gravitational potential of the initially unperturbed halo. This

---

raises the question how to identify the density and gravitational potential associated to the perturbation due to the vortex. The total halo density may be decomposed into

$$\rho = \rho_0 + \rho_1 . \quad (5.2)$$

Now owing to the linearity of the Laplace operator in the Poisson equation, one can write

$$\Delta\Phi = \Delta\Phi_0 + \Delta\Phi_1 = 4\pi G(\rho_0 + \rho_1) . \quad (5.3)$$

The fact that the unperturbed halo's density is given by

$$\rho_0 = m|\psi_0|^2 , \quad (5.4)$$

yields

$$\rho_1 = \rho - \rho_0 = \rho_0(|w|^2 - 1) \quad (5.5)$$

and hence

$$\Delta\Phi_1 = 4\pi G\rho_0(|w|^2 - 1) \quad (5.6)$$

must be solved for the gravitational potential associated to the distortion of the density.

We will apply the same method as [Rindler-Daller and Shapiro \(2012\)](#) (described in detail in their Appendix B) to arrive at a convenient splitting of the energy contributions by the unperturbed and vortex-carrying part. According to that method, inserting the ansatz (5.1) into the energy functional (4.4) yields

$$E'[\psi] = E'[\psi_0] + G'_{\rho_0}[w] - R'_{\rho_0}[w], \quad (5.7)$$

where

$$E'[\psi_0] = \int_V \left[ \frac{\hbar^2}{2m} (\vec{\nabla}|\psi_0|)^2 + \frac{m}{2} \Phi_0 |\psi_0|^2 + \frac{\hbar^2}{2m} |\psi_0|^2 \vec{\nabla} S'_0 \cdot \left( \vec{\nabla} S'_0 - \frac{2m}{\hbar} \vec{\Omega} \times \vec{r} \right) \right] dV , \quad (5.8)$$

$$G'_{\rho_0}[w] = \int_V \left[ \frac{\hbar^2}{2m^2} \rho_0 |\vec{\nabla} w|^2 + \frac{\rho_0}{2} \Phi_0 - \frac{\rho_0}{2} \Phi_0 |w|^2 + \frac{\rho_0}{2} \Phi_1 |w|^2 \right] dV \quad (5.9)$$

and

$$R'_{\rho_0}[w] = \int_V \frac{\hbar^2}{2m^2} \rho_0 i w^* \vec{\nabla} w \cdot \left( \vec{\nabla} S'_0 - \frac{m}{\hbar} \vec{\Omega} \times \vec{r} \right) dV . \quad (5.10)$$

A halo system in the fuzzy regime including one central vortex line is energetically favored

as compared to an unperturbed one, if

$$\delta E' \equiv G'_{\rho_0}[w] - R'_{\rho_0}[w] \quad (5.11)$$

is smaller than zero, i.e. reducing the total energy level of the system. Our aim now is to calculate  $\delta E'$  as a function of the parameters defining this model and in order to do so, we apply a density model and a vortex wavefunction which have already been introduced. As described at the beginning of Chapter 4 model A incorporates the ansatz

$$|\psi_0|^2 = \frac{\rho_0}{m} = \frac{\rho_c}{m} e^{-ar_s^2} = \frac{\rho_c}{m} e^{-a(r^2+z^2)} \quad (5.12)$$

for the unperturbed density of the halo with  $a = 1/(2\sigma^2)$  and the radial distance in spherical coordinates  $r_s$ . In Section 3.3, we have introduced the vortex ansatz in cylindrical coordinates  $(r, \phi, z)$ <sup>14</sup>

$$w(r, \phi) = |w|(r) e^{id\phi}, \quad (5.13)$$

with amplitude

$$|w|(r) = \begin{cases} 1 & \text{for } r \geq s, \\ C_n \left(\frac{r}{s}\right)^d & \text{otherwise.} \end{cases} \quad (5.14)$$

(Again,  $s$  denotes the vortex core size.) The form of this vortex wavefunction amplitude has some implications. First, it reflects that outside of the vortex, i.e. abruptly at  $r = s$ , the density is simply given by the unperturbed profile and that there is a discontinuity. Moreover, each axisymmetric integration including the vortex wavefunction has to be split accordingly at  $r = s$ . Also, even though halo model A is a sphere suggesting spherical coordinates during integration, the parametrization of the vortex demands cylindrical coordinates. As a result, the spherical domain over which the integration is performed is defined by the following intervals for the three cylindrical coordinates:

$$r \in [0, s] \text{ and } [s, \sqrt{R^2 - z^2}], \quad (5.15)$$

$$\phi \in [0, 2\pi], \quad (5.16)$$

$$z \in [0, R], \quad (5.17)$$

where  $R$  is the radius of the sphere, i.e. the size of the system set by (2.74).

When calculating the energy of a vortex-carrying system, the winding number (or charge) of the vortex plays an essential role. We have already discussed in Section 3.3 that  $d$  singly-

<sup>14</sup>The reader might wonder at the choice of notation considering the radial lengths in spherical and cylindrical coordinates,  $r_s$  and  $r$  respectively. For brevity, we have chosen  $r$  to denote the radial length in cylindrical coordinates throughout this Section since most parts of the integration will be done in cylindrical coordinates which is reasonable given the many integrals including the vortex wavefunction  $w(r, \phi)$ .

quantized vortices in a system are energetically favored compared to one  $d$ -charged vortex. Hence, we will restrict our analysis to singly-charged vortices, i.e.  $d = 1$ , and specifically to one central singly-quantized vortex.

The dimensionless constant  $C_n$  can now be determined by a normalization condition guaranteeing that

$$\int_V |\psi|^2 dV = \int_V \frac{\rho_0}{m} |w|^2 dV = N. \quad (5.18)$$

Inserting (2.76) into (5.12) and using (5.14), we get<sup>15</sup>

$$\begin{aligned} & \int_{z=-R}^R \int_{\phi=0}^{2\pi} \int_{r=0}^s \frac{Nm}{\sigma^3 (2\pi)^{3/2}} \frac{1}{m} e^{-a(r^2+z^2)} C_n^2 \left(\frac{r}{s}\right)^2 r dr d\phi dz \\ & + \int_{z=-R}^R \int_{\phi=0}^{2\pi} \int_{r=s}^{\sqrt{R^2-z^2}} \frac{Nm}{\sigma^3 (2\pi)^{3/2}} \frac{1}{m} e^{-a(r^2+z^2)} r dr d\phi dz \\ & = N \end{aligned} \quad (5.19)$$

$$\begin{aligned} & \Leftrightarrow \\ & C_n^2 \frac{2\sigma^2}{s^2} \left(1 - \exp\left[-\frac{s^2}{2\sigma^2}\right] \left(1 + \frac{s^2}{2\sigma^2}\right)\right) \text{Erf}\left[\frac{R}{\sigma\sqrt{2}}\right] \\ & + \exp\left[-\frac{s^2}{2\sigma^2}\right] \text{Erf}\left[\frac{R}{\sigma\sqrt{2}}\right] - \exp\left[-\frac{R^2}{2\sigma^2}\right] \sqrt{\frac{2}{\pi}} \frac{R}{\sigma} \\ & = 1 \end{aligned} \quad (5.20)$$

$$\begin{aligned} & \Leftrightarrow \\ C_n^2 & = \frac{s^2}{2} \frac{1 - \exp\left[-\frac{s^2}{2}\right] \text{Erf}\left[\frac{\tilde{R}}{\sqrt{2}}\right] + \exp\left[-\frac{\tilde{R}^2}{2}\right] \sqrt{\frac{2}{\pi}} \tilde{R}}{\left(1 - \exp\left[-\frac{s^2}{2}\right] \left(1 + \frac{s^2}{2}\right)\right) \text{Erf}\left[\frac{\tilde{R}}{\sqrt{2}}\right]} \end{aligned} \quad (5.21)$$

$$=: \frac{s^2}{2} K_n^2, \quad (5.22)$$

where  $\text{Erf}[x]$  denotes the Gauss error function given by the integral

$$\text{Erf}[x] = \frac{2}{\sqrt{\pi}} \int_0^x e^{-t^2} dt. \quad (5.23)$$

The first equivalence makes use of the definition (2.73) and the second equivalence makes use of a convention employed in the course of the entire forthcoming calculation. We have chosen to express all spatial variables in units of the standard deviation of the Gaussian density profile,  $\sigma$ , thereby introducing dimensionless variables which will be denoted as

$$\tilde{x} = \frac{x}{\sigma}, \quad (5.24)$$

<sup>15</sup>The index  $n$  in  $C_n$  and  $K_n$  refers to "normalization" and is not to be confused with the polytropic index.

---

where  $x$  stands for any spatial variable<sup>16</sup>. Moreover, it turns out that it will be useful in the course of calculating  $\delta E'$  to write  $C_n^2$  in the form of (5.22).

The density of a BEC- dark matter halo with a singly-quantized vortex in its center is then given by

$$\rho = \rho_0 |w|^2 = \begin{cases} \rho_0 = \rho_c e^{-a(r^2+z^2)} & \text{for } r \geq s, \\ \rho_0 C_n^2 \left(\frac{r}{s}\right)^2 = \rho_c e^{-a(r^2+z^2)} C_n^2 \left(\frac{r}{s}\right)^2 & \text{otherwise,} \end{cases} \quad (5.25)$$

with  $C_n^2$  given by (5.21). Two-dimensional density profiles  $\rho/\rho_c$  for  $s/\sigma = 0.8$  and  $s/\sigma = 1.8$  are shown in figures 5.1 and 5.2. They show that the vortex eats away the density in the very center of the halo as expected from the vortex wavefunction. [Mathematica-12.0 \(2019\)](#) plots a white ring at  $\tilde{r} = \tilde{s}$  where we find a discontinuity of the overall density profile. This discontinuity can be understood right away by considering both one-sided limits  $\lim_{r \rightarrow s^\pm} \rho$  approaching  $r = s$  from above or below. According to equation (5.25), approaching  $\rho$  at  $r = s$  from below yields  $\rho_c e^{-a(s^2+z^2)} C_n^2$  and from above yields  $\rho_c e^{-a(s^2+z^2)}$ . These two expressions differ by  $C_n^2$ , which itself is a function of the vortex core radius  $s$ . However, since we are considering global energies, this discontinuity poses no further problem.

Looking at equations (5.9) and (5.10), one can see that we are still missing two ingredients, namely the gravitational potentials  $\Phi_0$  and  $\Phi_1$  associated to the unperturbed halo density  $\rho_0$  and the perturbation of the density caused by the vortex  $\rho_1$ , respectively.

As discussed in Section (2.3),  $\Phi_0$  is originally one part of the solution  $(\psi, \Phi)$  of the time-independent and unperturbed Schrödinger-Poisson system (2.61) and (2.62), a pair of coupled equations admitting numerical solutions only. This system of equations consists of two second-order ordinary differential equations and an unknown parameter  $\mu$  thus requiring five boundary conditions. The wavefunction and the gravitational potential are required to be regular at the center and to vanish at infinity. In addition, the value of the wavefunction at the center is fixed. Our approach in model A included approximating the density of the unperturbed halo in spherical symmetry by the Gaussian profile in (2.72) thereby bypassing the numerical solution  $(\psi, \Phi)$  of the SP system. The most consistent way to determine  $\Phi_0$ , the gravitational potential associated to our ansatz for the density  $\rho_0$ , is now to consider the second part of the SP system, namely the Poisson equation. Thus,  $\Phi_0$  is the solution to the following boundary value problem in spherical coordinates:

---

<sup>16</sup>Have in mind, that this convention does not apply to (4.47).

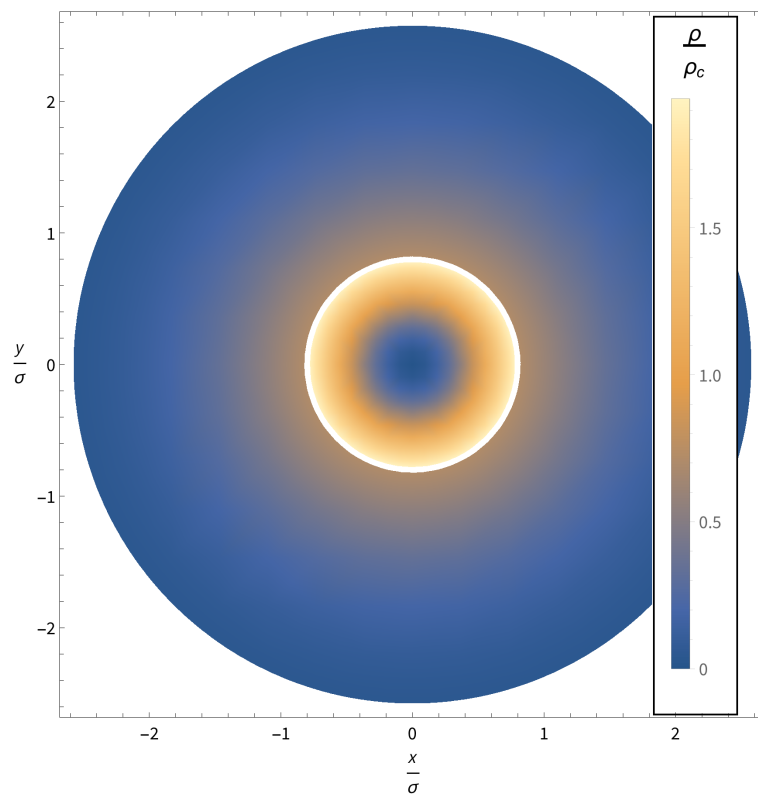


Figure 5.1: Density profile  $\rho = \rho_0|w|^2$  in units of  $\rho_c$  plotted for a BEC halo configuration with radius  $\bar{R} = 2.576$  and vortex core radius  $\bar{s} = 0.8$ .

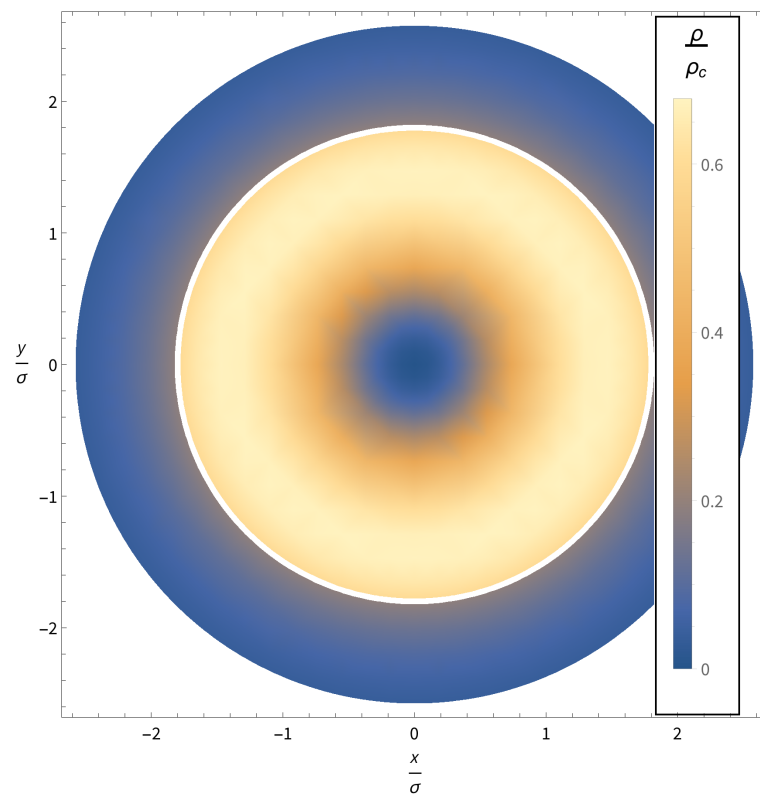


Figure 5.2: Density profile  $\rho = \rho_0 |w|^2$  in units of  $\rho_c$  plotted for a BEC halo configuration with radius  $\tilde{R} = 2.576$  and vortex core radius  $\tilde{s} = 1.8$ .

---


$$\Delta\Phi_0(r_s) = 4\pi G\rho_c e^{-ar_s^2} \quad (5.26a)$$

$$\frac{d}{dr_s}\Phi_0(0) = 0 \quad (5.26b)$$

$$\Phi_0(0) = A, \quad (5.26c)$$

where  $A$  is a constant. Imposing regularity, equation (5.26b), is effectively equivalent to requiring the absence of force in the centre. The computing system [Mathematica-12.0 \(2019\)](#) returns

$$\Phi_0(r_s) = A + \frac{2G\pi\rho_c}{a} - G\rho_c \left(\frac{\pi}{a}\right)^{3/2} \frac{\text{Erf}(\sqrt{a}r_s)}{r_s}, \quad (5.27)$$

as the solution to system (5.26). Requiring a finite configuration, i.e.

$$\lim_{r_s \rightarrow \infty} \Phi_0(r_s) = 0, \quad (5.28)$$

sets  $A = -\frac{2G\pi\rho_c}{a}$  and yields

$$\Phi_0(r_s) = -G\rho_c \left(\frac{\pi}{a}\right)^{3/2} \frac{\text{Erf}(\sqrt{a}r_s)}{r_s}. \quad (5.29)$$

The density perturbation due to the central singly-quantized vortex,

$$\begin{aligned} \rho_1 &= \rho - \rho_0 = m \frac{\rho_0}{m} |w|^2 - \rho_0 \\ &= \rho_0 (|w|^2 - 1) \\ &= \begin{cases} 0 & \text{for } r \geq s \\ \rho_0 \left( C_n^2 \left(\frac{r}{s}\right)^2 - 1 \right) < 0 & \text{otherwise,} \end{cases} \end{aligned} \quad (5.30)$$

is the source of the gravitational potential  $\Phi_1$ . Hence,

$$\Delta\Phi_1 = \begin{cases} \Delta\Phi_1^{(o)} = 0 & \text{for } r \geq s \\ \Delta\Phi_1^{(i)} = 4\pi G\rho_c e^{-ar^2} e^{-az^2} \left( C_n^2 \left(\frac{r}{s}\right)^2 - 1 \right) & \text{otherwise.} \end{cases} \quad (5.31)$$

In fact, obtaining  $\Phi_1$  is a much more complicated scheme, since we are looking for two different functions,  $\Phi_1^{(o)}$  and  $\Phi_1^{(i)}$ . The former is the solution to the following Laplace equation,

$$\Delta\Phi_1^{(o)}(r, z) = 0 \text{ for } r \geq s, \quad (5.32)$$

only valid outside the vortex (hence "(o)"). The general solution to equation (5.32) in cylindrical coordinates is

$$\Phi_1^{(o)}(r, z) = \frac{C_2 - C_1}{\sqrt{r^2 + z^2}}, \quad (5.33)$$

where  $C_1$  and  $C_2$  are integration constants. We follow the same line of argument as [Rindler-Daller and Shapiro \(2012\)](#) by imposing that the solution approaches a point-mass potential for large  $r$  at fixed  $z$  and for large  $z$  at fixed  $r$ . This yields

$$C_2 - C_1 = -GM_{\text{source}}, \quad (5.34)$$

where  $M_{\text{source}}$  is the mass of the assumed point-source. Basically, the notion is that if we are far away enough from the source, i.e. the region in which the vortex-perturbation acts, its gravitational potential field "feels" like a point-mass potential. However, how can  $M_{\text{source}}$  be determined? It is important to keep in mind, that the perturbed matter density inside the vortex region (5.30) is negative, which is physically comprehensible since the vortex removes or rather redistributes the initial matter from the vortex core region. Since this should be reflected by  $\Phi_1^{(o)}$ , we will set

$$M_{\text{source}} = -M_i, \quad (5.35)$$

where  $M_i$  is the mass inside the vortex core. In other words, the source of the outer-vortex potential associated with the perturbation of the density due to the vortex is set to be the negative vortex core mass. The mass inside the vortex core is given by

$$\begin{aligned} M_i &= \int_{z=-R}^R \int_{\phi=0}^{2\pi} \int_{r=0}^s \rho_0 C_n^2 \left(\frac{r}{s}\right)^2 r dr d\phi dz \\ &= Nm K_n^2 \left(1 - \exp\left[-\frac{s^2}{2\sigma^2}\right] \left(1 + \frac{s^2}{2\sigma^2}\right)\right) \text{Erf}\left[\frac{R}{\sigma\sqrt{2}}\right] \\ &= Nm \left(1 - \exp\left[-\frac{\tilde{s}^2}{2}\right] \text{Erf}\left[\frac{\tilde{R}}{\sqrt{2}}\right] + \exp\left[-\frac{\tilde{R}^2}{2}\right] \sqrt{\frac{2}{\pi}} \tilde{R}\right) \end{aligned} \quad (5.36)$$

and finally the potential by

$$\Phi_1^{(o)}(r, z) = \frac{GM_i}{\sqrt{r^2 + z^2}}. \quad (5.37)$$

Finding an analytical inner-vortex solution for  $\Phi_1^{(i)}$  posed a crucial problem to our analysis. The attempt to arrive at an analytical expression for the solution of

$$\Delta\Phi_1^{(i)} = 4\pi G\rho_c e^{-ar^2} e^{-az^2} \left(C_n^2 \left(\frac{r}{s}\right)^2 - 1\right) \quad \text{for } r < s \quad (5.38)$$

is described in [Appendix B](#). Since the partial differential equation (5.38) does not admit an analytical solution to our knowledge, we have solved it numerically. The Poisson equation

---

in question can be written as

$$\left[ \frac{\partial^2}{\partial z^2} + \frac{1}{r} \frac{\partial}{\partial r} + \frac{\partial^2}{\partial r^2} \right] \Phi_1^{(i)}(r, z) = 4\pi G \rho_c e^{-ar^2} e^{-az^2} \left( C_n^2 \left( \frac{r}{s} \right)^2 - 1 \right). \quad (5.39)$$

By multiplying both sides of equation (5.39) with

$$(4\pi G)^{-1} \rho_c^{-1} = \frac{\sigma^3 (2\pi)^{3/2}}{Nm4\pi G}$$

and introducing the dimensionless variable

$$\tilde{\Phi}_1^{(i)} = \Phi_1^{(i)} \frac{(2\pi)^{3/2}}{4\pi} \frac{\sigma}{NmG} \quad (5.40)$$

we get

$$\left[ \frac{\partial^2}{\partial \tilde{z}^2} + \frac{1}{\tilde{r}} \frac{\partial}{\partial \tilde{r}} + \frac{\partial^2}{\partial \tilde{r}^2} \right] \tilde{\Phi}_1^{(i)}(\tilde{r}, \tilde{z}) = e^{-\tilde{r}^2/2} e^{-\tilde{z}^2/2} \left( K_n^2 \frac{\tilde{r}^2}{2} - 1 \right), \quad (5.41)$$

with

$$K_n^2 = K_n^2[\tilde{s}, \tilde{R}] \quad (5.42)$$

given in (5.21). Initially, equation (5.41) has to be solved for  $\tilde{\Phi}_1^{(i)}$  inside the vortex region, i.e. in the region given by

$$\tilde{r} \in [0, \tilde{s}] \text{ and } \tilde{z} \in [-\tilde{R}, \tilde{R}].$$

However, since the density is an even function of  $\tilde{z}$ , the potential will be too and therefore we solved the system in the region

$$\tilde{r} \in [0, \tilde{s}] \text{ and } \tilde{z} \in [0, \tilde{R}].$$

The boundary of that rectangular domain of integration in the  $(\tilde{r}, \tilde{z})$ -plane consists of four line segments connecting the four vertices  $(0, 0)$ ,  $(\tilde{s}, 0)$ ,  $(\tilde{s}, \tilde{R})$ ,  $(0, \tilde{R})$ . There are two line segments connecting the vertices  $(0, 0)$  and  $(\tilde{s}, 0)$ , and  $(0, 0)$  and  $(0, \tilde{R})$  respectively, that lie within the vortex volume. Neumann boundary conditions, setting the normal derivative of  $\tilde{\Phi}_1^{(i)}$  to zero, were imposed on the differential equation along these line segments. Continuity requires that the solution of this partial differential equation matches with the analytical expression for the outer-vortex solution  $\Phi_1^{(o)}(r, z)$  at the respective line segments connecting the vertices  $(\tilde{s}, 0)$  and  $(\tilde{s}, \tilde{R})$ , and  $(0, \tilde{R})$  and  $(\tilde{s}, \tilde{R})$  respectively, i.e. those line segments at the boundary of the vortex volume. Hence, we impose the Dirichlet boundary condition

---


$$\begin{aligned}\tilde{\Phi}_1^{(i)}(\tilde{r}, \tilde{z}) &\stackrel{!}{=} \Phi_1^{(o)} \frac{(2\pi)^{3/2}}{4\pi} \frac{\sigma}{NmG} & (5.43) \\ &= \frac{1}{\sqrt{\tilde{r}^2 + \tilde{z}^2}} \sqrt{\frac{\pi}{2}} \left( 1 - \exp\left[-\frac{\tilde{s}^2}{2}\right] \operatorname{Erf}\left[\frac{\tilde{R}}{\sqrt{2}}\right] + \exp\left[-\frac{\tilde{R}^2}{2}\right] \sqrt{\frac{2}{\pi}} \tilde{R} \right) & (5.44)\end{aligned}$$

along those two line segments. To arrive at equation (5.44), we have used equations (5.36) and (5.37) and inserted (5.21). The implementation in [Mathematica-12.0 \(2019\)](#) returned a dimensionless interpolating function that we denote by  $\tilde{\Phi}_s$ , which is plotted for  $\tilde{s} = 0.8$  as a function of  $\tilde{r}$  and  $\tilde{z}$  in figure 5.3. However, the calculation of the gravitational energy requires the dimensional potential

$$\Phi_s = \tilde{\Phi}_s 4\pi G \rho_c \sigma^2. \quad (5.45)$$

Now the way is clear to proceed with the core of the calculation, namely determining  $\delta E'$ .

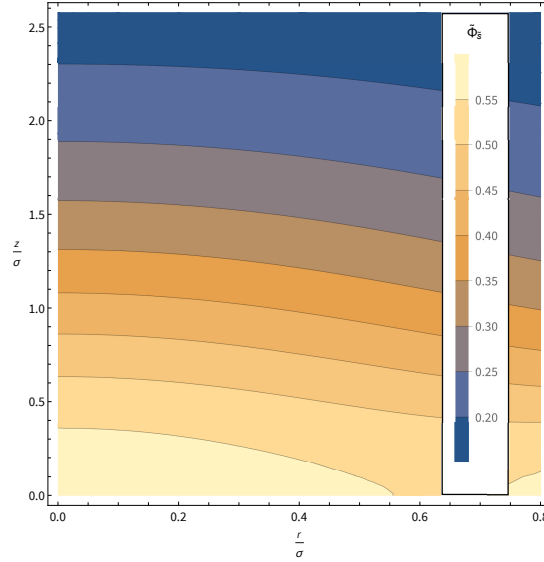


Figure 5.3: Contour plot of  $\tilde{\Phi}_s$  as a function of  $\tilde{r}$  and  $\tilde{z}$ .  $\tilde{R}$  was set according to (2.74) and  $\tilde{s} = 0.8$

We will consider each term in the equations (5.9) and (5.10) separately.

The quantum-kinetic term,

$$\int_V \frac{\hbar^2}{2m^2} \rho_0 |\vec{\nabla} w|^2 dV, \quad (5.46)$$

obviously requires to calculate the square of the absolute value of the gradient of the vortex wavefunction  $w$ .

---


$$\vec{\nabla}w = \begin{cases} \frac{i}{r}e^{i\phi}\hat{\mathbf{e}}_\phi & r \geq s \\ C_n \frac{i}{s}e^{i\phi}\hat{\mathbf{e}}_\phi + C_n \frac{1}{s}e^{i\phi}\hat{\mathbf{e}}_r & \text{otherwise,} \end{cases} \quad (5.47)$$

where  $\hat{\mathbf{e}}_\phi$  and  $\hat{\mathbf{e}}_r$  denote the azimuthal and radial unit vectors along the cylindrical coordinate directions. As a result, the absolute value of the complex vector field  $\vec{\nabla}w$  can be written as

$$\begin{aligned} |\vec{\nabla}w| &= \sqrt{(\vec{\nabla}w)^* \cdot \vec{\nabla}w} \\ &= \begin{cases} \frac{1}{r} & r \geq s \\ \frac{C_n}{s}\sqrt{2} & \text{otherwise.} \end{cases} \end{aligned} \quad (5.48)$$

After splitting the axisymmetric integration domain according to (5.15), the quantum-kinetic term yields

$$\begin{aligned} \int_V \frac{\hbar^2}{2m^2} \rho_0 |\vec{\nabla}w|^2 dV &= \frac{\hbar^2}{2m^2} \rho_c \int_{-R}^R \int_0^{2\pi} \int_s^{\sqrt{R^2-z^2}} e^{-ar^2} e^{-az^2} \frac{1}{r^2} r dr d\phi dz \\ &+ \frac{\hbar^2}{2m^2} \rho_c \int_{-R}^R \int_0^{2\pi} \int_0^s e^{-ar^2} e^{-az^2} 2 \frac{C_n^2}{s^2} r dr d\phi dz \\ &= \frac{\hbar^2}{2m^2} \rho_c \pi \left[ \int_{-R}^R e^{-az^2} \text{Ex}[-a(R^2-z^2)] dz - \sqrt{\frac{\pi}{a}} \text{Erf}[\sqrt{a}R] \text{Ex}[-as^2] \right] \\ &+ \frac{\hbar^2 \rho_c C_n^2 \pi}{m^2 s^2 a} (1 - e^{-as^2}) \sqrt{\frac{\pi}{a}} \text{Erf}[\sqrt{a}R], \end{aligned} \quad (5.49)$$

where the integral function  $\text{Ex}[x] = \text{ExpIntegralEi}[x] = -\int_{-x}^{\infty} \frac{e^{-t}}{t} dt$  is given by [Mathematica-12.0 \(2019\)](#). The quantum-kinetic term in [Rindler-Daller and Shapiro \(2012\)](#), who incorporate a homogeneous Maclaurin spheroid into their modelling, yields a logarithmic term of the form  $\ln(y/s)$ , where  $y$  is the length of the Maclaurin spheroid's equatorial semi-axes and  $s$  is the familiar vortex core radius. In fact, (5.49) shows a comparable functional behaviour which is revealed by the series representation of its factor  $-\text{Ex}[-x^2]$ ,

$$-\text{Ex}[-x^2] = -\gamma + \frac{1}{2} \ln\left(-\frac{1}{x^2}\right) - \frac{1}{2} \ln(-x^2) - \sum_{k=1}^{\infty} \frac{(-x^2)^k}{k k!}, \quad (5.50)$$

where  $\gamma$  is the Euler-Mascheroni constant.

The second term of  $G'_{\rho_0}[w]$  is a gravitational potential energy term, which on its own does not include information of the vortex. Hence, this undisturbed contribution to the gravitational potential energy, which affects the whole sphere equally, was determined by

integration in spherical coordinates.

$$\begin{aligned}\int_V \frac{\rho_0}{2} \Phi_0 dV &= 4\pi \frac{\rho_c}{2} \int_0^R e^{-ar_s^2} \left( -G\rho_c \left( \frac{\pi}{a} \right)^{3/2} \frac{\text{Erf}(\sqrt{ar_s})}{r_s} \right) r_s^2 dr_s \\ &= -2\pi\rho_c^2 G \left( \frac{\pi}{a} \right)^{3/2} \int_0^R e^{-ar_s^2} \text{Erf}(\sqrt{ar_s}) r_s dr_s,\end{aligned}\quad (5.51)$$

where solution (5.29) was inserted in place of  $\Phi_0$ . It is important to mention that the integration domain chosen for the calculation of this energy term is not exactly the same as the integration domain of all other terms. The reason is that when splitting the axisymmetric integration domain according to the vortex ansatz, we integrate over a cylinder with height  $2R$  and radius  $s$  and in addition over a domain which we can visualize by imagining the result of shooting this cylinder through the center of a sphere. With increasing  $s$ , the sum of this object's volume and the cylinder's volume differs a bit more from the volume of a sphere with radius  $R$ .

The third term of  $G'_{\rho_0}[w]$  amounts to

$$\begin{aligned}-\int_V \frac{\rho_0}{2} \Phi_0 |w|^2 dV &= \frac{C_n^2}{s^2} \rho_c^2 G \pi \left( \frac{\pi}{a} \right)^{3/2} \int_{-R}^R \int_0^s e^{-ar^2} e^{-az^2} \text{Erf} \left( \sqrt{a(r^2 + z^2)} \right) \frac{r^3}{\sqrt{r^2 + z^2}} dr dz \\ &+ \rho_c^2 G \pi \left( \frac{\pi}{a} \right)^{3/2} \\ &\cdot \int_{-R}^R \int_s^{\sqrt{R^2 - z^2}} e^{-ar^2} e^{-az^2} \text{Erf} \left( \sqrt{a(r^2 + z^2)} \right) \frac{r}{\sqrt{r^2 + z^2}} dr dz,\end{aligned}\quad (5.52)$$

while the term including the gravitational potential  $\Phi_1$  associated to the distortion of the density by the vortex is

$$\begin{aligned}\int_V \frac{\rho_0}{2} \Phi_1 |w|^2 dV &= \frac{\rho_c}{2} \int_{-R}^R \int_0^{2\pi} \int_0^s e^{-ar^2} e^{-az^2} C_n^2 \left( \frac{r}{s} \right)^2 \tilde{\Phi}_s[\vec{r}, \vec{z}] 4\pi G \rho_c \sigma^2 r dr d\phi dz \\ &+ \frac{\rho_c}{2} \int_{-R}^R \int_0^{2\pi} \int_s^{\sqrt{R^2 - z^2}} e^{-ar^2} e^{-az^2} \frac{GM_i}{\sqrt{r^2 + z^2}} r dr d\phi dz.\end{aligned}\quad (5.53)$$

Evaluating the rotational energy (5.10) requires some ground work. First, we have already established via equation (4.6) that the unperturbed sphere shows no net velocity in the rotating frame, i.e.  $\vec{\nabla} S'_0 = 0$ . Moreover, from (5.47) and

$$\vec{\Omega} = \Omega \hat{\mathbf{e}}_z, \quad (5.54)$$

$$\vec{r} = r \hat{\mathbf{e}}_r + z \hat{\mathbf{e}}_z, \quad (5.55)$$

$$\vec{\Omega} \times \vec{r} = \Omega r \hat{\mathbf{e}}_\phi \quad (5.56)$$

---

it follows that

$$\begin{aligned}
-R'_{\rho_0}[w] &= \frac{\hbar}{m}\rho_c \int_V i e^{-ar^2} e^{-az^2} w^* \vec{\nabla} w \cdot (\vec{\Omega} \times \vec{r}) dV \\
&= -\frac{\hbar}{m}\rho_c \int_{-R}^R \int_0^{2\pi} \int_0^s e^{-ar^2} e^{-az^2} \frac{C_n^2}{s^2} \Omega r^3 dr d\phi dz \\
&\quad -\frac{\hbar}{m}\rho_c \int_{-R}^R \int_0^{2\pi} \int_s^{\sqrt{R^2-z^2}} e^{-ar^2} e^{-az^2} \Omega r dr d\phi dz \\
&= -\Omega \frac{\hbar}{m}\rho_c \pi \frac{C_n^2}{s^2} \frac{1 - e^{-as^2}(1 + as^2)}{a^2} \sqrt{\frac{\pi}{a}} \text{Erf}(\sqrt{a}R) \\
&\quad -\Omega \frac{\hbar}{m}\rho_c \frac{\pi}{a} \left[ -2R e^{-aR^2} + e^{-as^2} \sqrt{\frac{\pi}{a}} \text{Erf}(\sqrt{a}R) \right] \\
&= -\hbar N \Omega, \tag{5.57}
\end{aligned}$$

where we have inserted the expressions for  $\rho_c$  and  $C_n^2$ , (2.76) and (5.21) respectively, in order to arrive at the last equality. In conclusion, the energy difference between the total energy of the halo-vortex configuration and the unperturbed halo energy  $E'[\psi_0]$  in the corotating frame in units of

$$\Omega_{QM} L_{QM} = \frac{N\hbar^2}{mR^2} \tag{5.58}$$

using the characteristic mass introduced in 2.3,

$$m_c^2 = \frac{\hbar^2}{RGM}, \tag{5.59}$$

amounts to

---


$$\begin{aligned}
& \frac{\delta E'}{\Omega_{QM} L_{QM}} = \\
= & \tilde{R}^2 2^{-5/2} \pi^{-1/2} \left[ \int_{-\tilde{R}}^{\tilde{R}} e^{-\tilde{z}^2/2} \text{Ex}\left(-\frac{1}{2}(\tilde{R}^2 - \tilde{z}^2)\right) d\tilde{z} - \sqrt{2\pi} \text{Ex}\left(-\frac{\tilde{s}^2}{2}\right) \text{Erf}\left(\frac{\tilde{R}}{\sqrt{2}}\right) \right] \\
& + K_n^2 \tilde{R}^2 \frac{1}{2} (1 - e^{-\frac{\tilde{s}^2}{2}}) \text{Erf}\left(\frac{\tilde{R}}{\sqrt{2}}\right) \\
& - \left(\frac{m}{m_c}\right)^2 \frac{\tilde{R}}{\sqrt{2\pi}} \int_0^{\tilde{R}} e^{-\frac{\tilde{r}_s^2}{2}} \text{Erf}\left(\frac{\tilde{r}_s}{\sqrt{2}}\right) \tilde{r}_s d\tilde{r}_s \\
& + K_n^2 \left(\frac{m}{m_c}\right)^2 2^{-5/2} \pi^{-1/2} \tilde{R} \int_{-\tilde{R}}^{\tilde{R}} \int_0^{\tilde{s}} e^{-\frac{\tilde{r}^2}{2}} e^{-\frac{\tilde{z}^2}{2}} \text{Erf}\left(\sqrt{(\tilde{r}^2 + \tilde{z}^2)/2}\right) \frac{\tilde{r}^3}{\sqrt{\tilde{r}^2 + \tilde{z}^2}} d\tilde{r} d\tilde{z} \\
& + \left(\frac{m}{m_c}\right)^2 2^{-3/2} \pi^{-1/2} \tilde{R} \int_{-\tilde{R}}^{\tilde{R}} \int_{\tilde{s}}^{\sqrt{\tilde{R}^2 - \tilde{z}^2}} e^{-\frac{\tilde{r}^2}{2}} e^{-\frac{\tilde{z}^2}{2}} \text{Erf}\left(\sqrt{(\tilde{r}^2 + \tilde{z}^2)/2}\right) \frac{\tilde{r}}{\sqrt{\tilde{r}^2 + \tilde{z}^2}} d\tilde{r} d\tilde{z} \\
& + \left(\frac{m}{m_c}\right)^2 \tilde{R} \frac{K_n^2}{4\pi} \int_{-\tilde{R}}^{\tilde{R}} \int_0^{\tilde{s}} e^{-\frac{\tilde{r}^2}{2}} e^{-\frac{\tilde{z}^2}{2}} \tilde{r}^3 \Phi_{\tilde{s}}[\tilde{r}, \tilde{z}] d\tilde{r} d\tilde{z} \\
& + \left(\frac{m}{m_c}\right)^2 \frac{\tilde{R} K_n^2}{\sqrt{\pi} 2^3} \left(1 - e^{-\frac{\tilde{s}^2}{2}} (1 + \frac{\tilde{s}^2}{2})\right) \text{Erf}\left(\frac{\tilde{R}}{\sqrt{2}}\right) \int_{-\tilde{R}}^{\tilde{R}} \int_{\tilde{s}}^{\sqrt{\tilde{R}^2 - \tilde{z}^2}} e^{-\frac{\tilde{r}^2}{2} - \frac{\tilde{z}^2}{2}} \frac{\tilde{r} d\tilde{r} d\tilde{z}}{\sqrt{\tilde{r}^2 + \tilde{z}^2}} \\
& - \frac{\Omega}{\Omega_{QM}}. \tag{5.60}
\end{aligned}$$

As a result, the energy difference in question is a function of several parameters, dark matter particle and model parameters, i.e.

$$\frac{\delta E'}{\Omega_{QM} L_{QM}} := \frac{\delta E'}{\Omega_{QM} L_{QM}} \left[ \frac{R}{\sigma'}, \frac{s}{\sigma'}, \frac{m}{m_c}, \frac{\Omega}{\Omega_{QM}} \right]. \tag{5.61}$$

Understanding the implications of this result, requires some intuition regarding the variables  $\delta E' / (\Omega_{QM} L_{QM})$  depends on.

To this aim, it is helpful to pay attention to the total angular momentum of the dark matter halo  $L$ . In fact, there is a necessary minimum condition for the creation of a vortex, namely

$$L \geq L_{QM}, \tag{5.62}$$

which has to be fulfilled for given parameters.  $L_{QM}$  is the minimum angular momentum, which is required to sustain a vortex line, i.e.

$$L_{QM} = N\hbar = MR^2\Omega_{QM}. \tag{5.63}$$

According to [Tipler and Mosca \(2015\)](#) the total angular momentum of a uniformly rotating

---

system whose axis of rotation coincides with an axis of symmetry, is given by

$$\vec{L} = I\vec{\Omega}, \quad (5.64)$$

where  $I$  denotes the moment of inertia.  $I$  of a continuous body rotating about a specified axis can be written as

$$I = \int_V \vec{r}_\perp^2 \rho(\vec{r}) dV, \quad (5.65)$$

If we decompose the position vector into a component parallel to the axis of rotation and perpendicular to the axis of rotation  $\vec{r}_\perp$ ,  $r_\perp$  gives the radial distance between each mass element and the axis of rotation provided that the center of the mass distribution is located at the origin of the coordinate system. Thus, it follows in spherical coordinates that

$$r_\perp^2 = r_s^2 \sin^2 \theta. \quad (5.66)$$

The total angular momentum of a uniformly rotating sphere filled with matter distributed according to our Gaussian density profile (2.72) is then given by

$$L = \Omega \int_V r_s^2 \sin^2 \theta \rho_c e^{-ar_s^2} r_s^2 \sin \theta d\theta d\phi dr_s, \quad (5.67)$$

with spherical coordinates  $(r_s, \theta, \phi)$ . This yields

$$L = \Omega I = \Omega \rho_c \frac{8\pi}{3} \left[ -\frac{R}{4a^2} e^{-aR^2} (3 + 2aR^2) + \frac{3\sqrt{\pi}}{8a^{5/2}} \text{Erf}(\sqrt{a}R) \right]. \quad (5.68)$$

As a result, condition (5.62) together with the expression for  $\rho_c$  and  $L_{QM} = \Omega_{QM} MR^2$  amounts to

$$1 \leq \frac{\Omega}{\Omega_{QM}} l(\tilde{R}), \quad (5.69)$$

with

$$l(\tilde{R}) = 2\sqrt{\frac{2}{\pi}} \left[ -\tilde{R}^{-1} e^{-\tilde{R}^2/2} (3 + \tilde{R}^2) + \frac{3\sqrt{\pi}}{8} 2^{5/2} \tilde{R}^{-2} \text{Erf}\left(\frac{\tilde{R}}{\sqrt{2}}\right) \right]. \quad (5.70)$$

As we have already discussed in Section 2.3, the size of our halo within model A will be set by  $R_{99}$ , thus

$$\tilde{R} = \frac{R}{\sigma} = \frac{R_{99}}{\sigma} = 2.575829 \approx 2.576. \quad (5.71)$$

Evaluating  $l(\tilde{R}) = l(2.576)$  in condition (5.69) thus yields a lower bound to the ratio  $\frac{\Omega}{\Omega_{QM}}$ :

$$1.43564 = \frac{1}{l(2.576)} \leq \frac{\Omega}{\Omega_{QM}}. \quad (5.72)$$

In the fuzzy regime, the vortex could in principle take up the whole halo, i.e.  $s \leq R$  or in dimensionless notation  $\tilde{s} = \frac{s}{\sigma} \leq \tilde{R}$ . Plotting the energy difference due to the vortex for different particle masses provides more detailed insight. This is where the considerations on the lower bound on the dark matter particle mass in the fuzzy regime (2.55) come into play. The implications on  $\delta E' / (\Omega_{QM} L_{QM})$  can be seen in figure 5.4, where the contributions of the central singly-quantized vortex to the energy of the system is plotted as a function of the vortex core radius for different dark matter particle masses  $m$  at the lower bound on the angular velocity  $1.43564 = \Omega / \Omega_{QM}$ .

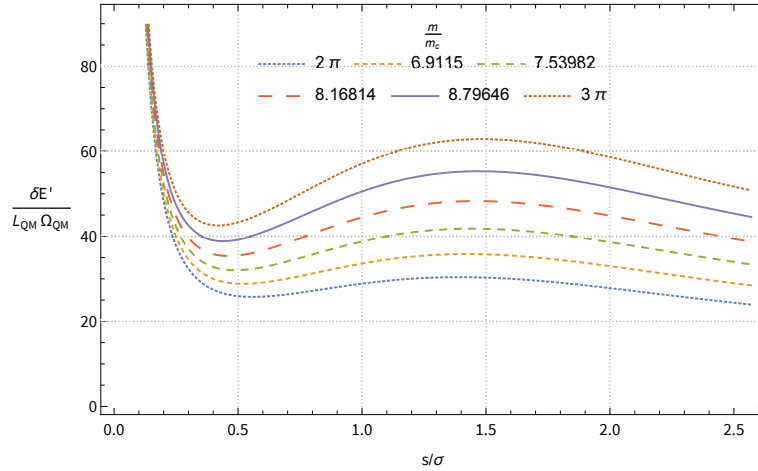


Figure 5.4: Vortex energy  $\delta E'$  in the corotating frame in units of  $(\Omega_{QM} L_{QM})$  plotted as a function of the vortex core radius  $s$  in units of  $\sigma$  for different particle masses  $m/m_c$ . The angular velocity is set to its minimum value,  $1.43564 = \Omega / \Omega_{QM}$ .

It is evident that at  $\Omega / \Omega_{QM} = 1.43564$  non-interacting BEC- dark matter particles are not able to form a central vortex in the context of halo-model A for any of the considered parameter values since  $\delta E' / (\Omega_{QM} L_{QM}) > 0$  everywhere. Moreover, we can see that with increasing dark matter particle mass vortex formation is even less energetically favored. The  $m$ -independent asymptotic behaviour for  $\tilde{s} \rightarrow 0$  is due to the quantum kinetic energy term (5.49). The  $m$ -dependent gravitational potential energy contribution not including any information on the vortex in equation (5.51) fans out the individual graphs in figure 5.4 since this term just adds a  $m$ -dependent constant value to the energy. The third term of  $G'_{\rho_0}[w]$ , which combines the unperturbed gravitational potential with the total density  $\rho_0 |w|^2$  does not show a strong dependence on the vortex core size  $s$  in the given range. Its effect on the to-

tal vortex energy  $\delta E' / (\Omega_{QM} L_{QM})$  amounts to a slight decrease with increasing  $s$ . The rough overall shape and dependence on the vortex core size  $s$  is to a great extent the result of the asymptotic quantum kinetic term and the gravitational potential energy due to the potential  $\Phi_1$ . This can be seen in figure 5.5 where the sum,

$$\int_V \frac{\hbar^2}{2m^2} \rho_0 |\vec{\nabla} w|^2 dV + \int_V \frac{\rho_0}{2} \Phi_1 |w|^2 dV, \quad (5.73)$$

is plotted in units of  $(\Omega_{QM} L_{QM})$  as a function of  $s/\sigma$  for different particle masses  $m$ . A comparison of figures 5.4 and 5.5 suggests that the absence of the remaining terms yields a slight horizontal stretching of the energy graphs. The striking dependence of the gravitational potential energy generated by the potential  $\Phi_1$  on the vortex core size, see equation (5.53), is shown in figures (5.6) and (5.7), where the two integrals corresponding to the inner- and outer-vortex contributions are plotted separately. While the monotonic increase of the inner-vortex contribution, first integral in (5.53), for halo configurations with a larger and larger central vortex is easily comprehensible, the  $s$ -dependence of the outer-vortex contribution, second integral in (5.53), is quite striking. In principle, this second integral should decrease with increasing  $\tilde{s}$  since in that case the integration domain decreases given a fixed halo size  $\tilde{R}$ . However, the  $s$ -dependence of the inner vortex mass (5.36) counteracts this general trend initially yielding a local maximum.

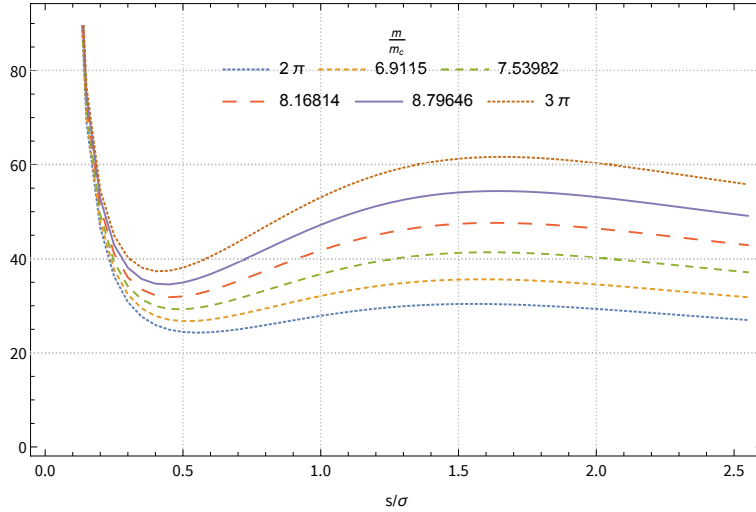


Figure 5.5: The sum of the quantum kinetic term (5.49) and the gravitational energy term including  $\Phi_1$  (5.53) in the corotating frame in units of  $(\Omega_{QM} L_{QM})$  plotted as a function of the vortex core radius  $s$  in units of  $\sigma$ . The angular velocity is set to its minimum value,  $1.43564 = \Omega/\Omega_{QM}$ .

Last but not least, there is the rotational energy term (5.57) which in units of  $(\Omega_{QM} L_{QM})$  yields  $-\Omega/\Omega_{QM}$ , thereby shifting the energy graphs in figure 5.4 as a whole towards lower

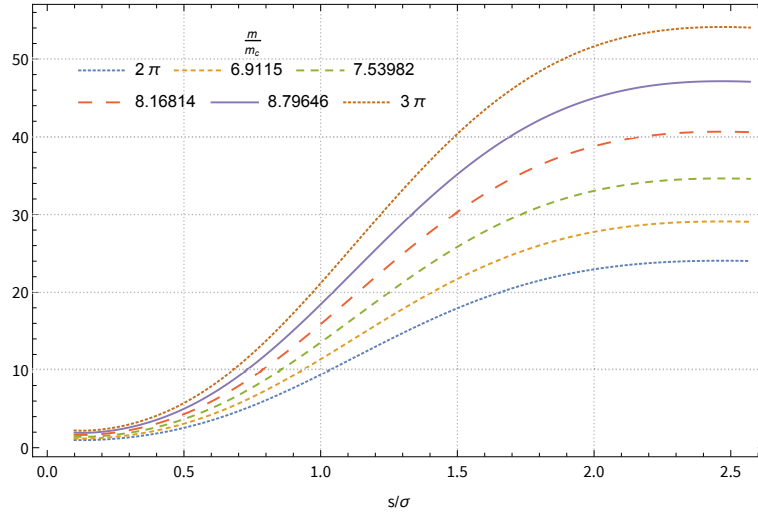


Figure 5.6: The first integral in expression (5.53) in units of  $(\Omega_{QM}L_{QM})$  plotted as a function of the vortex core radius  $s$  in units of  $\sigma$ . The angular velocity is set to its minimum value,  $1.43564 = \Omega/\Omega_{QM}$ . It is reasonable that the contribution to the vortex gravitational potential energy (5.53) from inside the vortex increases for halo configurations with a larger central vortex.

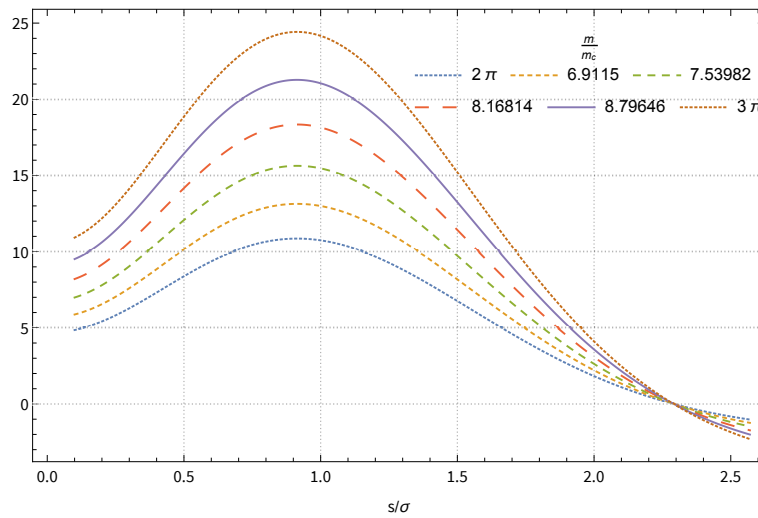


Figure 5.7: The second integral in expression (5.53) in units of  $(\Omega_{QM}L_{QM})$  plotted as a function of the vortex core radius  $s$  in units of  $\sigma$ . The angular velocity is set to its minimum value,  $1.43564 = \Omega/\Omega_{QM}$ . This term shows the most peculiar dependency on the vortex configuration.

values. Having in mind that vortex formation is energetically favored as soon as one of the graphs in figure 5.4 crosses the abscissa and that the condition  $L \geq L_{QM}$  only gives a lower bound to  $\Omega/\Omega_{QM}$ , we are required to determine a possible upper bound on  $\Omega/\Omega_{QM}$  from physical arguments in order to draw definite conclusions for model A.

First, we revisit considerations of Section 2.3 regarding the gravitational healing length  $\xi_G$ . We have encountered a notion considering the healing length  $\xi$  in the Thomas-Fermi regime, where it can be regarded as the distance over which the wave function tends to its background value when subjected to a localized perturbation. Moreover, it has already been established that a vortex can in fact be treated as a perturbation of a superfluid. In this sense, Rindler-Daller and Shapiro (2012) proceed in the course of their vortex energy analysis in the Thomas-Fermi regime with replacing the vortex core size by  $\xi$  on the assumption that  $s$  is of the same order as the healing length  $\xi$ . Following them, we proceed with the assumption that the vortex core size in the fuzzy regime is well approximated by the *gravitational* healing length

$$\xi_G = \frac{\hbar^2}{m^2 GM} = \left(\frac{m_c}{m}\right)^2 R. \quad (5.74)$$

This yields

$$\tilde{s} = \frac{s}{\sigma} \approx \xi_G = \left(\frac{m_c}{m}\right)^2 \tilde{R}, \quad (5.75)$$

i.e. for given  $\tilde{R} = 2.576$ , the vortex core radius is now a function of the particle mass. The result of replacing  $\tilde{s}$  in expression (5.60) for  $\delta E' / (\Omega_{QM} L_{QM})$  according to (5.75) altogether is shown in figure 5.8. This plot highlights the fact that vortex formation is even less energetically favored for higher dark matter particle masses  $m$ .

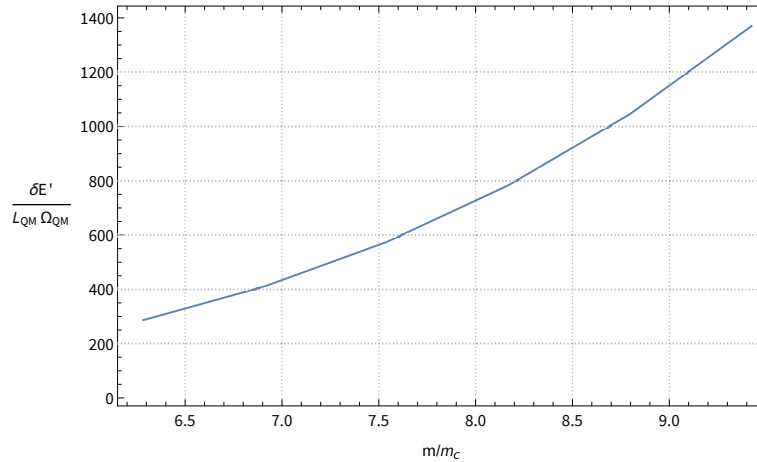


Figure 5.8: Vortex energy  $\delta E'$  in the corotating frame in units of  $(\Omega_{QM} L_{QM})$  plotted as a function of the particle mass  $m/m_c$ . The angular velocity is set to its minimum value,  $1.43564 = \Omega/\Omega_{QM}$ .

---

From a dynamical point of view considering cosmological simulations, the spin-parameter (4.1) (mentioned at the beginning of Chapter 4) provides means to quantify the degree of rotational support of a halo given its angular momentum  $L$ . In our case, we will use  $\lambda$  in order to derive meaningful angular velocities for our BEC-DM halo from the typical range of values for the spin-parameter,  $\lambda \in [0.01, 0.1]$ . To this aim, we will express  $\lambda$  as a function of the angular velocity and the dark matter particle mass. The following calculation considers a rotating BEC- dark matter halo prior to vortex formation. In other words, the derivation of  $\lambda = \lambda(\Omega, m)$  does not involve the vortex ansatz (5.13) or any perturbed quantities, but only unperturbed global properties of the halo such as  $L = \Omega I$  from equation (5.68) and the total energy in the *rest* frame in the fuzzy regime,

$$E = K + W, \quad (5.76)$$

with

$$K \equiv \int_V \frac{\hbar^2}{2m} |\nabla \psi_0|^2 d^3r \quad (5.77)$$

$$= \int_V \frac{\hbar^2}{2m^2} (\nabla \sqrt{\rho_0})^2 d^3r + \int_V \frac{\rho_0}{2} \vec{v}^2 d^3r \equiv K_Q + T, \quad (5.78)$$

and

$$W \equiv \int_V \frac{\rho_0}{2} \Phi_0 d^3r. \quad (5.79)$$

Given the Gaussian approximation for the density profile of the BEC halo (2.72), the quantum kinetic energy term  $K_Q$  amounts to

$$K_Q = \frac{\hbar^2}{2m^2} \rho_c a^2 4\pi \left[ -\frac{R}{4a^2} \exp(-aR^2) (3 + 2aR^2) + \frac{3\sqrt{\pi}}{8a^{5/2}} \text{Erf}(\sqrt{a}R) \right]. \quad (5.80)$$

The rotational kinetic energy incorporates the square of the bulk velocity of the unperturbed halo in the rest frame, i.e.

$$\begin{aligned} \vec{v}^2 &= (\vec{\Omega} \times \vec{r}) \cdot (\vec{\Omega} \times \vec{r}) \\ &= \Omega^2 r^2 - (\vec{\Omega} \cdot \vec{r})^2 \\ &= \Omega^2 \vec{r}_\perp^2. \end{aligned} \quad (5.81)$$

This yields

$$\begin{aligned} T &= \Omega^2 \frac{1}{2} \int_V \rho_0 r_\perp^2 dV \\ &= \frac{\Omega^2}{2} I, \end{aligned} \quad (5.82)$$

where the moment of inertia  $I$ , identified by expression (5.65), is given in (5.68). And finally,  $W$  is given by (5.51).

As a result, we get for the spin-parameter

$$\begin{aligned}\lambda &= \frac{L|E|^{1/2}}{GM^{5/2}} \\ &= \frac{\Omega I}{GM^{5/2}} \left| \frac{\hbar^2}{4m^2} a^2 3I + \frac{\Omega^2}{2} I - 2\pi\rho_c^2 G \left(\frac{\pi}{a}\right)^{3/2} \int_0^R e^{-ar_s^2} \text{Erf}(\sqrt{a}r_s) r_s dr_s \right|^{1/2}. \quad (5.83)\end{aligned}$$

The square of  $\lambda$  can in turn be written as

$$\lambda^2 = \left(\frac{\Omega}{\Omega_{\text{grav}}}\right)^2 \frac{|I|^3 9}{M^3 R^6 16} \left| \left(\frac{\Omega_{QM}}{\Omega_{\text{grav}}}\right)^2 \tilde{R}^4 \frac{3}{2^4} + \frac{1}{2} \left(\frac{\Omega}{\Omega_{\text{grav}}}\right)^2 - \frac{R^3 \sigma^2}{B} C \right|, \quad (5.84)$$

where

$$\Omega_{\text{grav}}^2 := \frac{3GM}{4R^3} \quad (5.85)$$

denotes the square of the gravitational angular velocity,

$$C = \int_0^{\tilde{R}} e^{-\frac{\tilde{r}_s^2}{2}} \text{Erf}\left(\frac{\tilde{r}_s}{\sqrt{2}}\right) \tilde{r}_s d\tilde{r}_s \quad (5.86)$$

the dimensionless quantity depending on  $\tilde{R}$  and

$$B = -\frac{R}{4a^2} e^{-aR^2} (3 + 2aR^2) + \frac{3\sqrt{\pi}}{8a^{5/2}} \text{Erf}(\sqrt{a}R) \quad (5.87)$$

an expression with the dimension  $\text{Length}^5$ . Inserting

$$\frac{\Omega_{QM}}{\Omega_{\text{grav}}} = \frac{\hbar}{m} \frac{2}{\sqrt{3GM\tilde{R}}} = \frac{m_H}{m} = \frac{2}{\sqrt{3}} \frac{m_c}{m}, \quad (5.88)$$

and setting

$$\tilde{\Omega} = \frac{\Omega}{\Omega_{QM}} \quad (5.89)$$

finally yields

$$\begin{aligned}\lambda^2 &= \tilde{\Omega}^2 \left(\frac{m_c}{m}\right)^2 \frac{4\sqrt{2}}{9\pi^{3/2}} \left| -\frac{3 + \tilde{R}^2}{\tilde{R}} \exp(-\tilde{R}^2/2) + \frac{3\sqrt{\pi}}{8} 2^{5/2} \frac{\text{Erf}(\tilde{R}/\sqrt{2})}{\tilde{R}^2} \right|^3 \\ &\quad \left| \left(\frac{m_c}{m}\right)^2 \frac{\tilde{R}^4}{4} + \tilde{\Omega}^2 \frac{2}{3} \left(\frac{m_c}{m}\right)^2 - \frac{C}{-\frac{3+\tilde{R}^2}{\tilde{R}^2} \exp(-\tilde{R}^2/2) + \frac{3\sqrt{\pi}}{8} 2^{5/2} \frac{\text{Erf}(\tilde{R}/\sqrt{2})}{\tilde{R}^3}} \right|. \quad (5.90)\end{aligned}$$

Hence, we see that  $\lambda^2$  is a cumbersome function of  $(\bar{\Omega}, \bar{R}, m/m_c)$ . Since the final goal is to derive values for  $\Omega$  from given  $\lambda$ -values in the range  $[0.01, 0.1]$  and isolating  $\bar{\Omega}$  in equation (5.90) is not possible, we calculate the roots of equation (5.90) for given  $\lambda^2$  and  $m/m_c$ . This approach is illustrated in figure 5.9 which shows that since equation (5.90) is a non-linear function in  $\bar{\Omega}$ , several values for  $\bar{\Omega}$  correspond to one  $\lambda$ -value. We deal with this degeneracy by setting  $\bar{\Omega}$  to the highest of the three corresponding roots for every  $\lambda$  and  $m/m_c$ . In this way, if vortex formation is not energetically favored given that choice for  $\bar{\Omega}$ , it is safe to conclude that vortex formation is also not favored for any of the other possibilities due to the degeneracy. It is important to mention at this point that the angular velocity  $\Omega$  corresponding

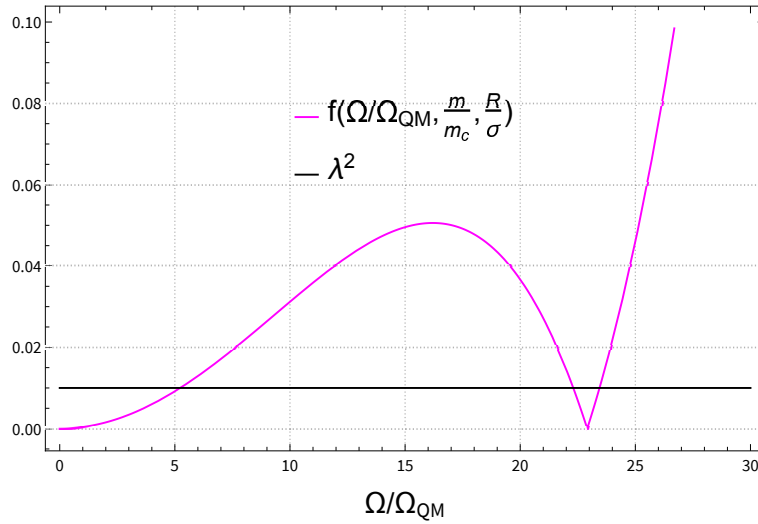


Figure 5.9:  $\lambda^2$  plotted as a function of  $\Omega/\Omega_{QM}$  for  $\bar{R} = 2.576$  and  $m/m_c = 3\pi$ . The magenta curve depicts the right-hand side of equation (5.90). For  $\lambda^2 = 0.01$  (black constant line), equation (5.90) returns three roots which lie at the crossing points of the two curves.

to a given  $\lambda$  now depends on the particle mass  $m$ . In this way, we calculate the contributions of the central singly-quantized vortex to the energy of the system,  $\delta E'/(\Omega_{QM}L_{QM})$ , again as a function of  $m/m_c$  by setting  $\bar{s} = \bar{\xi}_G$ , fixing the value of  $\lambda^2$  and calculating  $\bar{\Omega}$  for every  $m/m_c$  in the considered range. Figures 5.10 and 5.11 show the result of this procedure for the  $\lambda$ -values (0.01, 0.05, 0.1, 0.5, 30). One can immediately see that  $\delta E'/(\Omega_{QM}L_{QM}) \gg 0$  for any considered BEC-DM halo configuration. Even the graphs corresponding to  $\lambda$ -values which lie far away from the range suggested by cosmological N-body simulations, i.e.  $\lambda = 0.5$  or even  $\lambda = 30$  (for illustrative purposes), come nowhere near the abscissa.

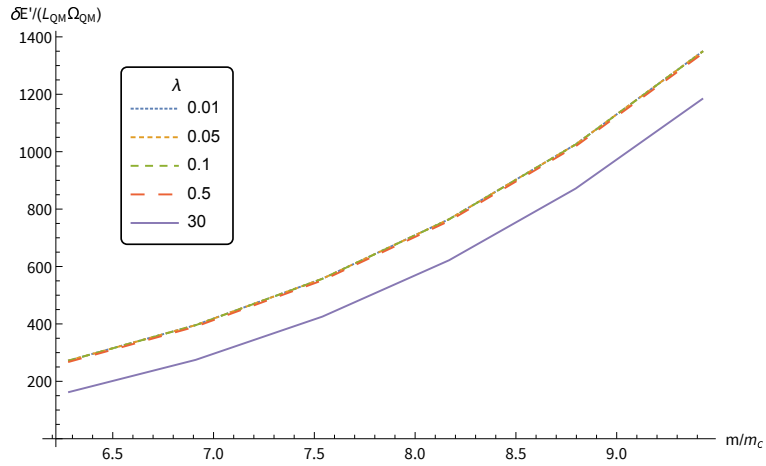


Figure 5.10: Vortex energy  $\delta E'$  in the corotating frame in units of  $(\Omega_{QM} L_{QM})$  plotted as a function of the particle mass  $m/m_c$  for different spin-parameter values  $\lambda$ . The angular velocity is set according to equation (5.90) for fixed  $\lambda$  and  $m/m_c$ .

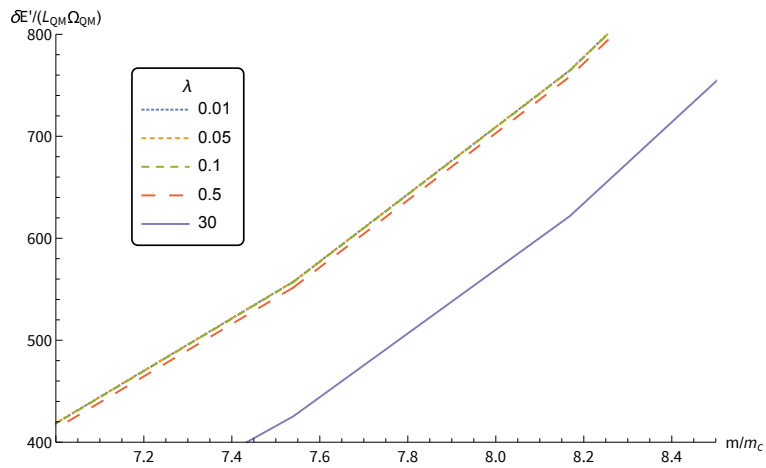


Figure 5.11: A zoom-in of figure 5.10.

---

## 5.2 Model B: The irrotational Riemann-S ellipsoid

So far, we have considered spherical BEC- dark matter halos in the context of model A and conclude that due to our energy argument vortex formation is not favored in the case of this setup. However, model A, incorporating the Gaussian sphere, can be refined and further developed considering two aspects in particular; the spherical shape and the simple uniform rotation. As we have already mentioned in Chapter 4 and described in detail in Section 4.1, [Lai et al. \(1993\)](#) provide us with the compressible generalization of a classical figure of rotation perfectly suited for our purpose; the compressible irrotational Riemann-S ellipsoid.

Dark matter halos presumably acquire angular momentum by tidal torques caused by large-scale structure in early phases of their collapse. As a result, they will attain *non-spherical* equilibrium configurations. Thus, an improved analysis of our BEC-DM halo shall incorporate these notions, inspired by the approach of [Rindler-Daller and Shapiro \(2012\)](#). In that paper, BEC-DM halos in the Thomas-Fermi regime prior to vortex formation were modelled as (n=1)-polytropic, irrotational Riemann-S ellipsoids. In this work, we will model BEC-DM halos in the fuzzy regime by using again the irrotational Riemann-S ellipsoid. However, this time its density profile is given by an (n=2)-polytrope, based upon the analysis in Section 2.3. In other words, the initially vortex-free BEC- dark matter halo will have all the properties of an ( $n = 2$ ) irrotational Riemann-S ellipsoid. The attribute "irrotational" leads us directly to the second reason why halo model B represents a refinement of model A. While the Gaussian sphere model just considered uniform rotation, the defining internal velocity field of Riemann-S ellipsoids given in (4.29) enabling the irrotational sequence of the Riemann-S ellipsoids allows us to account for the irrotationality of the velocity fields of superfluids and Bose-Einstein condensates.

However, by now we know that Bose-Einstein condensates are not irrotational wherever the phase function diverges, i.e. wherever there is a vortex line. As a result, this Section is dedicated to pursue the question of whether vortex formation in a rotating BEC- dark matter halo in the fuzzy regime, which will initially be modeled as a Riemann-S ellipsoid, is also energetically disfavored as concluded in the previous Section for model A. To this aim, we will apply an energy argument, which is similar but not equivalent to the approach described in the previous Section and has been established by [Rindler-Daller and Shapiro \(2012\)](#).

Let us consider some unspecified dynamical process in the course of which a Bose-Einstein condensed halo, described by the Gross-Pitaevskii-Poisson framework in the fuzzy regime, creates one singly-charged vortex in its center. The actual occurrence of this vortex creation requires that the process in question transforms the initial state of the halo into a final state with lower total energy compared to the initial state. As a result, we are going to look at two "snapshots" of that transformation, namely the initial and the final configuration, calculate their total energies and compare those for a given set of parameter ranges.

---

The underlying halo will be modeled by an irrotational Riemann-S ellipsoid along the lines of Section 4.1. In the context of model B, we will assume that the process taking the halo from a vortex-free configuration to a configuration with one central vortex allows this vortex in question to take up all of the angular momentum of the system once it has formed. In this way, the source for the ellipsoidal shape of the halo vanishes thereby allowing us to draw on the Gaussian sphere as a model for the second snapshot or final state in other words. In the course of the following calculations, it was important to distinguish between quantities and global properties of the initial Riemann-S ellipsoid, which will be denoted by the index  $R$ , and the final Gaussian sphere, denoted by the index  $G$ .

We start the analysis by considering the total energy of the vortex-free initial configuration in the rest frame which can be written as

$$E_R = K_Q + T + W, \quad (5.91)$$

where  $T$  and  $W$  are given by (4.32) and (4.26) in Section 4.1, respectively.  $K_Q$  on the other hand has no classical counterpart and is therefore absent in the equilibrium figure studies of Chandrasekhar (1969) or Lai et al. (1993). However, the internal energy of a Riemann-S ellipsoid is given by (4.12) and can be written as

$$U = k_1 K_p \rho_{c,R}^{1/n} M, \quad (5.92)$$

due to the ellipsoidal approximation, where  $\rho_{c,R}$  is the central density of the initial Riemann-S ellipsoid incorporating a polytropic density profile. The following argumentation allows us to derive an expression for the quantum-kinetic energy  $K_Q$  of a Bose-Einstein condensed Riemann-S ellipsoid from (5.92).

The studies of Lai et al. (1993) on ellipsoidal equilibrium figures come with the huge advantage of presenting global energy expressions provided that the density and pressure profiles of the figures in question are those of polytropes of index  $n$  and polytropic constant  $K_p$ . At this point, the second density profile to approximate the actual "soliton" solution of the Gross-Pitaevskii-Poisson system in the fuzzy regime, the  $(n = 2)$ -polytropic profile,

$$\rho(r) = \rho_c \theta(\xi)^2, \quad \xi = r \left( \frac{\hbar^2}{8\pi G m^2 \rho_c} \right)^{-1/4}, \quad (5.93)$$

established in Section 2.3 comes into play. This model allows us to apply the results of Lai et al. (1993) in order to find the total energy of our initial halo configuration. According to considerations of Chavanis (2019a), associating the  $(n = 2)$ -polytropic profile with our BEC

---

halo requires the polytropic constant to be identified as

$$K_p = \left( \frac{2\pi G \hbar^2}{9m^2} \right)^{1/2}. \quad (5.94)$$

In addition, we know from [Chavanis \(2019a\)](#) that the internal energy of a sphere arising from a polytropic pressure is related to the quantum kinetic energy via

$$K_Q = \frac{3}{2}U \quad (5.95)$$

given the density profile (5.93). As a consequence, since according to [Lai et al. \(1993\)](#)'s ellipsoidal approximation the total internal energy of a rotating polytrope is identical to that of a spherical one with same central density, it follows that the quantum-kinetic energy of a Bose-Einstein condensed Riemann-S ellipsoid can be written as

$$K_Q = \frac{3}{2}k_1 K_p \rho_{c,R}^{1/2} M, \quad (5.96)$$

with  $K_p$  given by (5.94) and  $n = 2$ . Before we can continue with the calculation of the total energy  $E_R$ , the current analysis requires to establish relations between several quantities of the initial and final state of the halo. While the underlying initial halo configuration is modeled as an irrotational ( $n = 2$ ) Riemann-S ellipsoid whose respective energy terms [Lai et al. \(1993\)](#) derive from initially spherical polytropes modified by rotation, we set the final halo configuration to be a sphere - a Gaussian sphere not a polytrope. However, [Lai et al. \(1993\)](#) provide us with a relation between the mean radius of the Riemann-S ellipsoid  $R_R = (a_1 a_2 a_3)^{1/3}$  and the radius of the non-rotating, spherical equilibrium *polytrope*,  $R_0$ , with same mass  $M$ , constant  $K_p$  and index  $n$ :

$$R_R = R_0 \left[ f \left( 1 - 2 \frac{T}{|W|} \right) \right]^{-n/(3-n)}, \quad (5.97)$$

where  $f$  is the dimensionless factor defined in (4.19). Now, the process which we are considering shall transform the system in such a way that it settles with the radius of the final Gaussian configuration,  $R_G$ , which we will in turn associate with  $R_0$ . In this sense, we heavily rely on the fact that the density profile of a BEC-DM halo in the fuzzy limit can be approximated by both, the Gaussian profile and the ( $n = 2$ ) polytropic profile. Thus, it follows for

---

polytropic index  $n = 2$  that

$$\begin{aligned} R_R &= R_0 \left[ f \left( 1 - 2 \frac{T}{|W|} \right) \right]^{-2/(3-2)} \\ &\stackrel{!}{=} R_G g(e_1, e_2)^{-2}, \end{aligned} \quad (5.98)$$

where  $g(e_1, e_2) := \left[ f(e_1, e_2) \left( 1 - 2 \frac{T}{|W|} \right) \right]$  since the dimensionless factor  $f$  can be written as a function of the axis ratios or equally as a function of the eccentricities of the ellipsoid,

$$e_1 = \sqrt{1 - (a_2/a_1)^2} \quad \text{and} \quad e_2 = \sqrt{1 - (a_3/a_1)^2}. \quad (5.99)$$

Moreover, the radius of the Gaussian final state  $R_G$  will again be set to  $R_{99}$  due to the fact that the Gaussian profile does not offer a compact support. What about the central densities of the initial and final configurations? Given the central density  $\rho_{c,s}$  of the spherical polytrope with radius  $R_0$ , we have the relation between the central and mean density of a polytrope,

$$\bar{\rho}_s = \frac{3M}{4\pi R_0^3} = 3\rho_{c,s} \frac{|\theta'_1|}{\xi_1}, \quad (5.100)$$

see Appendix A. The analogue for the polytropic Riemann ellipsoid can be written as

$$\bar{\rho}_R = \frac{3M}{4\pi R_R^3} = 3\rho_{c,R} \frac{|\theta'_1|}{\xi_1}. \quad (5.101)$$

The BEC halo in question is considered to be an isolated system, i.e. a closed box in which the total mass  $M$  is conserved. Thus, dividing equation (5.101) by equation (5.100) yields

$$\bar{\rho}_R = \bar{\rho}_s g(e_1, e_2)^6 \quad \text{and} \quad \rho_{c,R} = \rho_{c,s} g(e_1, e_2)^6, \quad (5.102)$$

where we have used relation (5.98). In the context of this model, the vortex-free Riemann-S ellipsoid is sent to a Gaussian sphere with vortex. Hence, we set

$$\rho_{c,s} \stackrel{!}{=} \rho_{c,G} = \frac{M}{\sigma^3 (2\pi)^{3/2}}, \quad (5.103)$$

even though unlike the spherical polytrope the Gaussian profile has no compact support, i.e.  $\rho_{c,G}$  is the central density of an infinitely large system which we cut off at  $R_{99}$ . Once more, we rely on the two density toy models to be equally appropriate and closely related. As a result, the total internal energy of the Riemann-S ellipsoid can be written as

$$U = k_1 \left( \frac{2\pi}{9} \right)^{1/2} G^{1/2} \frac{\hbar}{m} \rho_{c,G}^{1/2} g(e_1, e_2)^3 M, \quad (5.104)$$

where we have used (5.94) and  $k_1$  is given in (4.14) and has to be evaluated for  $n = 2$ . Consequently, the quantum-kinetic energy of the Bose-Einstein condensed Riemann-S ellipsoid in units of  $\Omega_{QM,R}L_{QM}$  is given by

$$\frac{K_Q}{\Omega_{QM,R}L_{QM}} = \frac{3}{2}k_1 \frac{(2\pi)^{1/2}}{3} \frac{\Omega_{\text{grav},R}}{\Omega_{QM,R}} \sqrt{\frac{4}{3}} \left(\frac{R_R}{\sigma}\right)^{3/2} \frac{g(e_1, e_2)^3 M}{M(2\pi)^{3/4}} \quad (5.105)$$

$$= \frac{k_1}{2(2\pi)^{1/4}} \frac{m}{m_{c,R}} \tilde{R}_G^{3/2}, \quad (5.106)$$

where we have used

$$R_R = R_G g(e_1, e_2)^{-2}, \quad (5.107)$$

$$\Omega_{\text{grav},R} = \sqrt{\frac{3GM}{4R_R^3}}, \quad (5.108)$$

$$\Omega_{QM,R} = \frac{\hbar}{\sqrt{R_R GM}}, \quad (5.109)$$

$$m_{c,R} = \frac{\hbar}{\sqrt{R_R GM}} = \frac{\hbar}{\sqrt{R_G GM}} g(e_1, e_2) = m_{c,G} g(e_1, e_2) \text{ and} \quad (5.110)$$

$$\frac{\Omega_{\text{grav},R}}{\Omega_{QM,R}} = \frac{\sqrt{3}}{2} \frac{m}{m_{c,R}} = \frac{\sqrt{3}}{2} \frac{m}{m_{c,G}} g(e_1, e_2)^{-1}. \quad (5.111)$$

By means of the above relations the gravitational potential energy (4.26) for ( $n = 2$ ) in units of  $\Omega_{QM,R}L_{QM}$  amounts to

$$\frac{W}{\Omega_{QM,R}L_{QM}} = -\frac{\Omega_{\text{grav},R}^2 M 4 R_R^2}{3} f(e_1, e_2) \frac{1}{\Omega_{QM,R} N \hbar} \quad (5.112)$$

$$= -\left(\frac{m}{m_{c,R}}\right)^2 f(e_1, e_2). \quad (5.113)$$

The rotational kinetic energy (4.32) on the other hand gives

$$\frac{T}{\Omega_{QM,R}L_{QM}} = \frac{\kappa_2 m \Omega^2}{20 \Omega_{QM,R} \hbar} \left[ (a_1 - a_2)^2 \left(1 + \frac{1}{h(e_1)}\right)^2 + (a_1 + a_2)^2 \left(1 - \frac{1}{h(e_1)}\right)^2 \right] \quad (5.114)$$

$$= \left(\frac{\Omega}{\Omega_{QM,R}}\right)^2 \frac{e_1^4}{(1 - e_1^2)^{1/3} (1 - e_2^2)^{1/3} (2 - e_1^2)}, \quad (5.115)$$

where the value for  $\kappa_2$  can be found in Appendix A and the definition of the dimensionless

factor  $h(e_1)$  arises from setting  $f_R = -2$  and combining the relations (4.1) and (4.30):

$$h(e_1) = \frac{2 - e_1^2}{2\sqrt{1 - e_1^2}} = \frac{1}{2} \left( \frac{a_1}{a_2} + \frac{a_2}{a_1} \right) = \frac{\Omega}{\Lambda}. \quad (5.116)$$

The vortex-free irrotational Riemann-S ellipsoid is sent to a final state that consists of a Gaussian sphere hosting a central singly-charged vortex. In other words, the final state corresponds to our halo model A. Thus, the total energy *in the corotating frame* of the final configuration amounts to

$$E'_G = E'_G[\psi_0] + G'_{\rho_0}[w] - R'_{\rho_0}[w] = E'_G[\psi_0] + \delta E'_G, \quad (5.117)$$

where the total energy of the vortex-free system is given by (5.8) and the energy terms associated to the vortex by (5.9) and (5.10). Since  $\vec{\nabla} S'_0$  vanishes,  $E'_G[\psi_0]$  is given by the sum of the two expressions from Section 5.1, (5.80) and (5.51),

$$\begin{aligned} E'_G[\psi_0] &= \frac{\hbar^2}{2m^2\rho_{c,G}a^2} 4\pi \left[ -\frac{R_G}{4a^2} \exp(-aR_G^2)(3 + 2aR_G^2) + \frac{3\sqrt{\pi}}{8a^{5/2}} \text{Erf}(\sqrt{a}R_G) \right] \\ &\quad - 2\pi\rho_{c,G}^2 G \left( \frac{\pi}{a} \right)^{3/2} \int_0^{R_G} e^{-ar_s^2} \text{Erf}(\sqrt{a}r_s) r_s dr_s. \end{aligned} \quad (5.118)$$

$\delta E'_G$  is given by equation (5.60) except for the fact that equation (5.60) already includes a division by  $\Omega_{QM,G}L_{QM}$ . However, in order to compare the total energies of the initial and final state on an equal footing, we need to express  $E'_G[\psi_0]$  as well as  $\delta E'_G$  in units of  $\Omega_{QM,R}L_{QM}$ , which due to  $\Omega_{QM,R} = g(e_1, e_2)^4 \Omega_{QM,G}$  yields

$$\frac{\delta E'_G}{\Omega_{QM,R}L_{QM}} = g(e_1, e_2)^{-4} \frac{\delta E'_G}{\Omega_{QM,G}L_{QM}}, \quad (5.119)$$

where  $\frac{\delta E'_G}{\Omega_{QM,G}L_{QM}}$  is given in (5.60), and

$$\begin{aligned} \frac{E'_G[\psi_0]}{\Omega_{QM,R}L_{QM}} &= g(e_1, e_2)^{-4} \tilde{R}_G^2 \frac{\pi}{2(2\pi)^{3/2}} \left[ -\tilde{R}_G \exp(-\tilde{R}_G^2/2)(3 + \tilde{R}_G^2) + \frac{3\sqrt{\pi}}{8} 2^{5/2} \text{Erf} \left( \frac{\tilde{R}_G}{\sqrt{2}} \right) \right] \\ &\quad - g(e_1, e_2)^{-4} \left( \frac{m}{m_{c,G}} \right)^2 \frac{\tilde{R}_G}{\sqrt{2\pi}} \int_0^{\tilde{R}_G} e^{-\tilde{r}_s^2/2} \text{Erf} \left( \frac{\tilde{r}_s}{\sqrt{2}} \right) \tilde{r}_s d\tilde{r}_s. \end{aligned} \quad (5.120)$$

The difference in total energy between the initial vortex-free Riemann-S ellipsoidal state and the final spherical state with a vortex in the center  $\delta E'_{RG}$  in the frame rotating with angular velocity  $\Omega$  can be written as

$$\delta E'_{RG} = E'_G - E'_R = (E'_G[\psi_0] + \delta E'_G) - (E_R - \Omega L), \quad (5.121)$$

---

where we are still missing an accurate expression for  $\Omega L$  in units of  $\Omega_{QM,R}L_{QM}$ . Combining the relations (4.31), (4.33) and (5.116), the total angular momentum of an irrotational Riemann-S ellipsoid rotating with angular velocity  $\Omega$  amounts to

$$L = \frac{\kappa_2 M}{5} \Omega \left( (a_1^2 + a_2^2) - \frac{4a_1^2}{1 + \left(\frac{a_1}{a_2}\right)^2} \right). \quad (5.122)$$

As a result, the total angular momentum in terms of  $L_{QM}$  yields

$$\frac{L}{L_{QM}} = \frac{\kappa_2}{5} \frac{m}{m_{c,R}} \frac{\sqrt{3}}{2} \frac{\Omega}{\Omega_{\text{grav},R}} \frac{e_1^4}{(1 - e_1^2)^{1/3} (1 - e_2^2)^{1/3} (2 - e_1^2)}. \quad (5.123)$$

Hence, (the polytropic index  $n$  being set to 2) the angular momentum in units of  $L_{QM}$  is just a function of the dark matter particle mass  $m/m_{c,R}$  for fixed eccentricities, i.e. a fixed halo geometry. In other words, given a halo shape, requiring the amount of angular momentum to be enough in order to sustain a vortex sets a condition on the particle mass. From (5.123) it follows

$$\frac{\Omega L}{\Omega_{QM,R} L_{QM}} = \tilde{\Omega}^2 \frac{\kappa_2}{5} \frac{m^2}{m_{c,G}^2} \frac{3}{4} g(e_1, e_2)^{-2} \frac{e_1^4}{(1 - e_1^2)^{1/3} (1 - e_2^2)^{1/3} (2 - e_1^2)}, \quad (5.124)$$

with

$$\tilde{\Omega} = \Omega / \Omega_{\text{grav},R}. \quad (5.125)$$

In summary, the dimensionless energy difference in units of  $\Omega_{QM,R}L_{QM}$  between the initial

state and final state amounts to

$$\begin{aligned}
& \frac{\delta E'_{RG}}{\Omega_{QM,R} L_{QM}} = \\
& = g(e_1, e_2)^{-4} \tilde{R}_G^2 \frac{\pi}{2(2\pi)^{3/2}} \left[ -\tilde{R}_G \exp(-\tilde{R}_G^2/2)(3 + \tilde{R}_G^2) + \frac{3\sqrt{\pi}}{8} 2^{5/2} \text{Erf} \left( \frac{\tilde{R}_G}{\sqrt{2}} \right) \right] \\
& - g(e_1, e_2)^{-4} \left( \frac{m}{m_{c,G}} \right)^2 \frac{\tilde{R}_G}{\sqrt{2\pi}} \int_0^{\tilde{R}_G} e^{-\tilde{r}_s^2/2} \text{Erf} \left( \frac{\tilde{r}_s}{\sqrt{2}} \right) \tilde{r}_s d\tilde{r}_s \\
& + g(e_1, e_2)^{-4} \frac{\delta E'_G}{\Omega_{QM,G} L_{QM}} \left[ \frac{m}{m_{c,G}}, \tilde{s}, \tilde{R}_G, \frac{\Omega}{\Omega_{QM,G}} \right] \\
& - \frac{k_1}{2(2\pi)^{1/4}} \frac{m}{m_{c,G}} g(e_1, e_2)^{-1} \tilde{R}_G^{3/2} \\
& + \left( \frac{m}{m_{c,G}} \right)^2 g(e_1, e_2)^{-2} f(e_1, e_2) \\
& - \frac{\kappa_2}{10} \left( \frac{\Omega}{\Omega_{QM,R}} \right)^2 \frac{e_1^4}{(1 - e_1^2)^{1/3} (1 - e_2^2)^{1/3} (2 - e_1^2)} \\
& + \tilde{\Omega}^2 \frac{\kappa_2}{5} \frac{m^2}{m_{c,G}^2} \frac{3}{4} g(e_1, e_2)^{-2} \frac{e_1^4}{(1 - e_1^2)^{1/3} (1 - e_2^2)^{1/3} (2 - e_1^2)}, \tag{5.126}
\end{aligned}$$

with the vortex-carrying part  $\delta E'_G / (\Omega_{QM,G} L_{QM}) [m/m_{c,G}, \tilde{s}, \tilde{R}_G, \Omega/\Omega_{QM,G}]$  given by (5.60) and

$$\frac{\Omega}{\Omega_{QM,R}} = \tilde{\Omega} \frac{m}{m_{c,G}} \frac{\sqrt{3}}{2} g(e_1, e_2)^{-1}, \tag{5.127}$$

$$\frac{\Omega}{\Omega_{QM,G}} = \tilde{\Omega} \frac{m}{m_{c,G}} \frac{\sqrt{3}}{2} g(e_1, e_2)^3. \tag{5.128}$$

In order to understand the implications of  $\delta E'_{RG} / (\Omega_{QM,R} L_{QM})$ , we are going to gradually incorporate the framework built by [Lai et al. \(1993\)](#) constructing the equilibrium sequence of Riemann-S ellipsoids, which has been introduced in Section 4.1.

First of all, the gravitational angular velocity  $\tilde{\Omega}$  cannot be independently chosen within this framework but is directly coupled to the geometry of the ellipsoid, in other words to the axis ratios  $a_2/a_1$  and  $a_3/a_1$ , for given polytropic index  $n$  and ratio  $f_R = -2$  via (see (4.51))

$$\tilde{\Omega} \equiv \frac{\Omega}{\Omega_{\text{grav},R}} = \left( \frac{2B_{12}}{q_n} \right)^{1/2} \left( 1 + \frac{4(a_2/a_1)^2}{(1 + (a_2/a_1)^2)^2} \right)^{-1/2}. \tag{5.129}$$

Hence, a visualization of the energy difference's dependence on the vortex core radius  $s$  only requires a choice of axis ratios and to set  $\tilde{R}_G = R_{99}/\sigma = 2.576$ . This can be seen in figure 5.12, where  $a_2/a_1 = 0.7981$  and  $a_3/a_1 = 0.8836$ . At this stage this prolate shape might seem like a random choice. However, we will go into detail on how the spin-parameter  $\lambda$  fixes the

halo's geometry later.

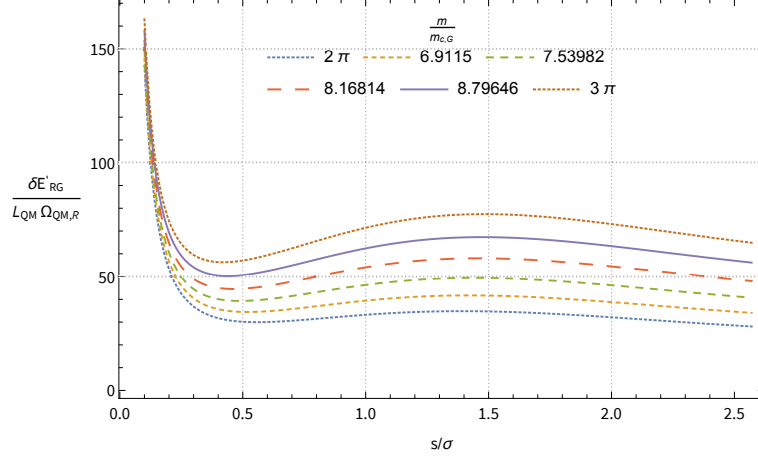


Figure 5.12: Difference in energy  $\delta E'_{RG}$  in the rotating frame in units of  $(\Omega_{QM,R} L_{QM})$  (see (5.126)) plotted as a function of the vortex core radius  $s$  in units of  $\sigma$  for different particle masses  $m/m_{c,G}$ . The gravitational angular velocity is set according to equation (5.129) for given polytropic index  $n = 2$ , ratio  $f_R = -2$  and axis ratios  $a_2/a_1 = 0.7981$  and  $a_3/a_1 = 0.8836$ .

Obviously, figure 5.12 shows the same functional shape as figure 5.4 in the previous Section since the only term in equation (5.126) which depends on  $s$  is our result (5.60) of model A. The far more interesting implication of figure 5.12 is that  $\delta E'_{RG}/(\Omega_{QM,R} L_{QM}) > 0$  and therefore  $E'_G > E'_R$  for every considered choice of halo parameters. We can thus conclude that a process transforming a vortex-free Riemann-S ellipsoid into a Gaussian sphere with a central vortex, which corresponds to our model A, would not be energetically favored.

The fact that vortex formation as part of such a process is even less energetically favored for higher dark matter particle masses is clearly visible in figure 5.13, where the vortex core size is assumed to be of the same order as the gravitational healing length  $\tilde{\zeta}_G$  and thus a function of the particle mass for given  $\tilde{R}_G = 2.576$ :

$$\tilde{s} = \frac{s}{\sigma} \approx \tilde{\zeta}_G = \left( \frac{m_{c,G}}{m} \right)^2 \tilde{R}_G. \quad (5.130)$$

Lai et al. (1993) construct an equilibrium sequence of Riemann-S ellipsoids by starting with the equilibrium conditions (4.42) and (4.43) which eventually yield a relation between the axis ratios  $a_2/a_1$  and  $a_3/a_1$  along a given sequence with fixed  $f_R$ . This relation, given in (4.50) along the irrotational sequence ( $f_R = -2$ ), carries an important implication with it. For given  $f_R$  and one axis ratio, we can immediately determine the second axis ratio, thereby the angular velocity  $\tilde{\Omega}$  and the angular frequency of the internal superposed velocity field  $\Lambda$  of our ellipsoidal equilibrium figure, in other words  $a_2/a_1$  determines the entire geometry and in the further course even global quantities like the total angular momentum (see Section 5.2

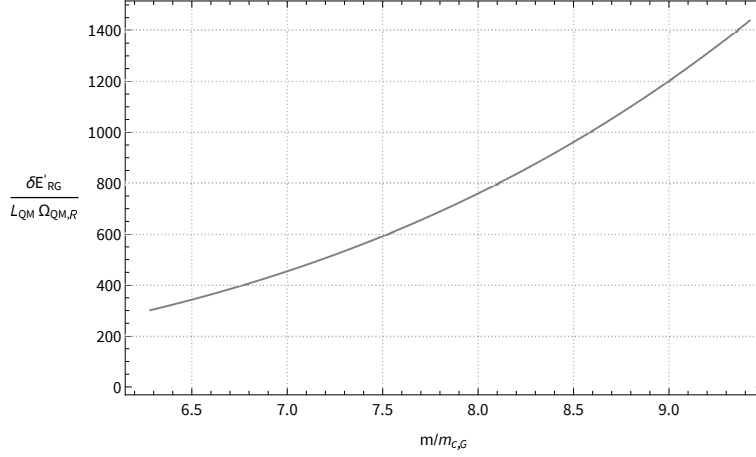


Figure 5.13: Difference in energy  $\delta E'_{RG}$  in the rotating frame in units of  $(\Omega_{QM,R} L_{QM})$  (see (5.126)) plotted as a function of the dark matter particle mass  $m/m_{c,G}$  by means of (5.130). The gravitational angular velocity is set according to equation (5.129) for given polytropic index  $n = 2$ , ratio  $f_R = -2$  and axis ratios  $a_2/a_1 = 0.7981$  and  $a_3/a_1 = 0.8836$ .

of Lai et al. (1993)). However, Rindler-Daller and Shapiro (2012) show that specifying the spin-parameter  $\lambda$  allows us even to determine *both* axis ratios self-consistently by solving a system of equations consisting of relation (4.50) and the following expression for  $\lambda$  in the case of an Riemann-S ellipsoid. We can write  $\lambda$  as

$$\lambda = \frac{L|W|^{1/2}}{GM^{5/2}} \left| \frac{E}{W} \right|^{1/2}, \quad (5.131)$$

where

$$\frac{L|W|^{1/2}}{GM^{5/2}} = \frac{\kappa_2}{5} (\Omega(a_1^2 + a_2^2) - 2a_1a_2\Lambda) \left( \frac{|f(e_1, e_2)|}{GR_R M} \right)^{1/2} \quad (5.132)$$

follows from inserting (4.26) and (4.31). The virial relation (4.44) yields the equilibrium energy (4.52). A division of  $E_{eq}$  by the gravitational potential energy eventually amounts to

$$\left| \frac{E_{eq}}{W} \right|^{1/2} = \left( \frac{1}{2}(1+t) \right)^{1/2}, \quad (5.133)$$

where  $t := \frac{T}{|W|}$ . Rewriting and multiplying the expressions (5.132) and (5.133) yields

$$\lambda = \frac{\tilde{\Omega}\kappa_2\sqrt{3}}{10} \left( \frac{1}{2}(1+t) \right)^{\frac{1}{2}} \left| f \left( \frac{a_2}{a_1}, \frac{a_3}{a_1} \right) \right|^{\frac{1}{2}} \frac{(1 - (a_2/a_1)^2)^2}{1 + (a_2/a_1)^2} \left( \frac{a_2}{a_1} \right)^{-\frac{2}{3}} \left( \frac{a_3}{a_1} \right)^{-\frac{2}{3}}, \quad (5.134)$$

---

with

$$t := \frac{T}{|W|} \quad (5.135)$$

$$= \frac{\frac{\kappa_2}{20} M ((a_1 - a_2)^2 (\Omega + \Lambda)^2 + (a_1 + a_2)^2 (\Omega - \Lambda)^2)}{GM^2 |f(e_1, e_2)| / R_R} \quad (5.136)$$

$$= \kappa_2 \frac{3}{40} |f(e_1, e_2)|^{-1} \frac{e_1^4}{(1 - e_1^2)^{1/3} (1 - e_2^2)^{1/3} (2 - e_1^2)}. \quad (5.137)$$

In order to arrive at equations (5.134) and (5.137),

$$\tilde{\Omega}^2 := \Omega^2 / \Omega_{\text{grav},R}^2 = \frac{\Omega^2 4R_R^3}{3GM}, \quad (5.138)$$

the relation (5.116), the eccentricities  $e_1 = \sqrt{1 - (a_2/a_1)^2}$  and  $e_2 = \sqrt{1 - (a_3/a_1)^2}$  and the mean radius

$$R_R = (a_1 a_2 a_3)^{1/3} = a_1 (1 - e_1^2)^{1/6} (1 - e_2^2)^{1/6} \quad (5.139)$$

were used along the way.

Solving the system of equations (4.50) and (5.134) given the typical range of values for the spin-parameter,  $\lambda \in [0.01, 0.1]$ , in addition to values beyond that range,  $\lambda \in [0.1, 0.3]$ , yields the corresponding axis ratios and values for several dimensionless global quantities and properties of the Riemann-S ellipsoid which only depend on the ratios  $a_2/a_1$  and  $a_3/a_1$  shown in table 5.1. The numerical values of the dimensionless quantities ,

$$\tilde{\Lambda} := \frac{\Lambda}{\Omega_{\text{grav},R}} = \tilde{\Omega}^2 \frac{2\sqrt{1 - e_1^2}}{2 - e_1^2}, \quad (5.140)$$

$$|\tilde{W}| := \frac{|W|}{GM^2/R_R} = f(e_1, e_2), \quad (5.141)$$

$$\frac{R_R}{R_0} = g(e_1, e_2)^{-2}, \quad (5.142)$$

$$\tilde{L}^2 := \frac{L^2}{GM^3 R_R} = \left(\frac{\kappa_2}{5}\right)^2 \frac{3}{4} \tilde{\Omega}^2 \frac{e_1^8}{(2 - e_1^2)^2 (1 - e_1^2)^{2/3} (1 - e_2^2)^{2/3}}, \quad (5.143)$$

which are functions of the eccentricities or equally axis ratios,  $\tilde{\Omega}$  and  $\kappa_2$ , were computed by [Mathematica-12.0 \(2019\)](#) once the system of equations (4.50) and (5.134) was solved for  $a_2/a_1$  and  $a_3/a_1$ . From table 5.1 it is evident that ( $n = 2$ )-polytropic Riemann-S ellipsoids are prolate figures. Figures 5.14 and 5.15 show how the geometry of our BEC- dark matter halo in question is influenced by the spin-parameter  $\lambda$  and the theoretical framework of Riemann-S ellipsoids by the system of equations (4.50) and (5.134).

Bringing the energy analysis back into focus, we can see in figure 5.16 the energy differ-

---

$\lambda$	$e_1$	$e_2$	$a_2/a_1$	$a_3/a_1$	$t$
0.01	0.60246	0.46823	0.79815	0.88361	$3.411 \cdot 10^{-3}$
0.03	0.73601	0.60587	0.67697	0.79556	$1.0328 \cdot 10^{-2}$
0.05	0.79654	0.67861	0.60458	0.73450	$1.7337 \cdot 10^{-2}$
0.1	0.87098	0.78203	0.49132	0.62324	$3.5048 \cdot 10^{-2}$
0.2	0.93067	0.88056	0.36585	0.47394	$7.0077 \cdot 10^{-2}$
0.3	0.95701	0.92861	0.29005	0.37107	$1.0326 \cdot 10^{-1}$
$\lambda$	$\bar{\Omega}$	$\bar{\Lambda}$	$\bar{L}^2$	$ \bar{W} $	$R_R/R_0$
0.01	0.55513	0.54131	$1.9999 \cdot 10^{-4}$	0.99661	1.0207
0.03	0.55644	0.51663	$1.7999 \cdot 10^{-3}$	0.98981	1.0642
0.05	0.55659	0.49287	$4.9998 \cdot 10^{-3}$	0.98299	1.1106
0.1	0.55266	0.43746	$2.0007 \cdot 10^{-2}$	0.96580	1.2398
0.2	0.53113	0.34275	$8.0359 \cdot 10^{-2}$	0.93034	1.5627
0.3	0.49831	0.26663	$1.8267 \cdot 10^{-1}$	0.89313	1.9911

Table 5.1: Parameters (defined in (5.140)-(5.143)) of the irrotational, ( $n = 2$ )-polytropic Riemann-S ellipsoid as a function of  $\lambda$  computed by means of [Mathematica-12.0 \(2019\)](#).

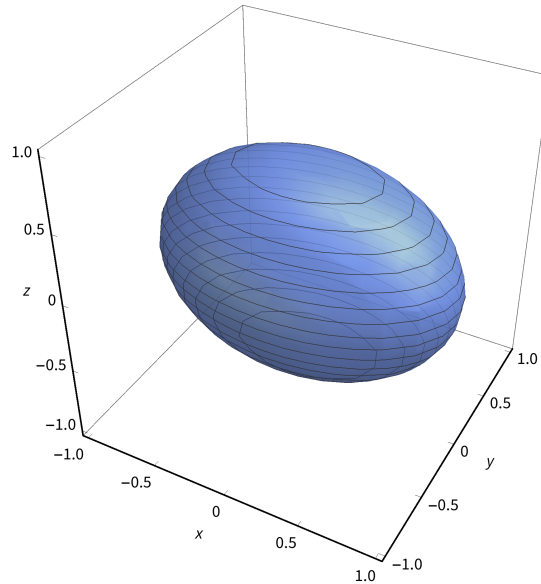


Figure 5.14: Irrotational Riemann-S ellipsoid rotating about the z-axis with  $a_1 = 1$  and  $\lambda = 0.05$ .

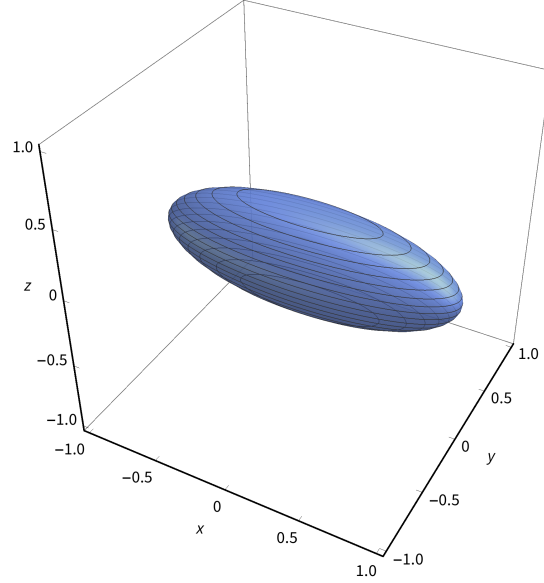


Figure 5.15: Irrotational Riemann-S ellipsoid rotating about the z-axis with  $a_1 = 1$  and  $\lambda = 0.3$ .

ence  $\delta E'_{RG}/(\Omega_{QM,R}L_{QM})$  plotted as a function of the particle mass  $m$  along the lines of figure 5.13. However, now the axis-ratios and thus the energy difference are fixed by the spin-parameter  $\lambda$ . In fact, thanks to the total angular momentum in terms of  $L_{QM}$  given in (5.123), we are given the opportunity to constrain the transition from a Bose-Einstein condensed Riemann-S ellipsoidal halo into a Gaussian sphere with one central vortex even further by imposing  $L \stackrel{!}{=} L_{QM}$ , i.e. the constraint of having exactly the minimum amount of angular momentum to sustain one vortex. Meeting this condition implies

$$\frac{m}{m_{c,G}} \stackrel{!}{=} g(e_1, e_2) \left( \frac{\kappa_2 \sqrt{3}}{5} \tilde{\Omega} \frac{e_1^4}{(1-e_1^2)^{1/3}(1-e_2^2)^{1/3}(2-e_1^2)} \right)^{-1}, \quad (5.144)$$

i.e. the dark matter particle mass is now a function of the halo geometry. In other words, a fixed halo spinning given by  $\lambda$  together with the constraint that the halo system shall possess a total angular momentum of exactly  $L_{QM}$  during the entire transition, results in condition (5.144) on the particle mass. In figure 5.17 one can see the condition on the particle mass as a function of the spin-parameter  $\lambda$  for three different fixed total angular momenta  $L \in [L_{QM}, 10L_{QM}, 100L_{QM}]$ . This logarithmically scaled plot shows that either higher values for  $\lambda$  or lower total angular momenta imply lower dark matter particle masses. Finally, it is evident that setting the total angular momentum to  $L_{QM}$  has implications on the energy difference  $\delta E'_{RG}/(\Omega_{QM,R}L_{QM})$  between the initial and final state of the transition considered in halo model B. We have seen that requiring  $L \stackrel{!}{=} L_{QM}$  essentially fixes the particle mass

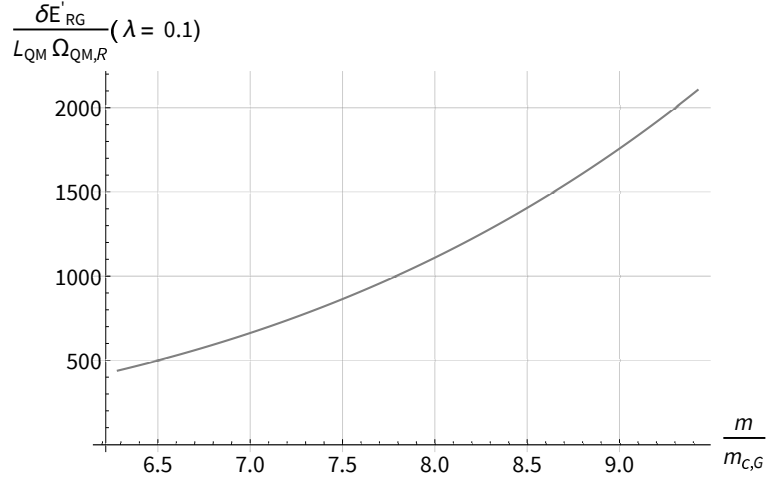


Figure 5.16: Difference in energy  $\delta E'_{RG}$  in the rotating frame in units of  $(\Omega_{QM,R} L_{QM})$  (see (5.126)) plotted as a function of the dark matter particle mass  $m/m_{c,G}$  by means of (5.130). The gravitational angular velocity is set according to equation (5.129) for given polytropic index  $n = 2$ , ratio  $f_R = -2$  and the axis ratios are listed in table 5.1 for  $\lambda = 0.1$ .

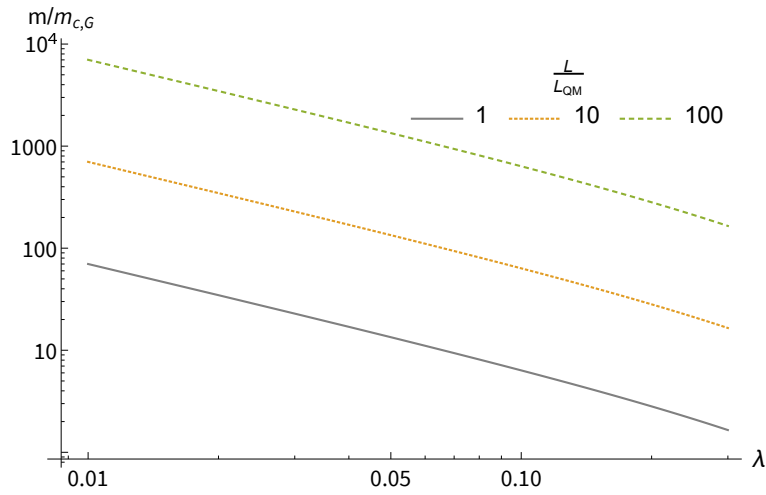


Figure 5.17: Particle mass  $m$  in units of  $m_{c,G}$  as a function of the spin-parameter  $\lambda$  for three different fixed total angular momenta  $L \in [L_{QM}, 10L_{QM}, 100L_{QM}]$ .

for given  $\lambda$  or equally for given axis ratios of the halo. Hence, this condition can only be met at one single point when considering the energy difference as a function of particle mass like in figure 5.16. As a result, in the case of  $L \stackrel{!}{=} L_{QM}$  fixing the halo geometry by  $\lambda$  immediately yields one value for  $\delta E'_{RG}/(\Omega_{QM,R}L_{QM})$ . This can be seen in figure 5.18, where  $\delta E'_{RG}/(\Omega_{QM,R}L_{QM})$  and  $m/m_{c,G}$  are plotted as a function of  $\lambda$ . We can see that although the energy difference decreases with increasing spin-parameter, it is far away from becoming negative within the  $\lambda$ -range given by cosmological simulations and thus vortex formation in the fuzzy regime is also not favored in the context of halo model B.

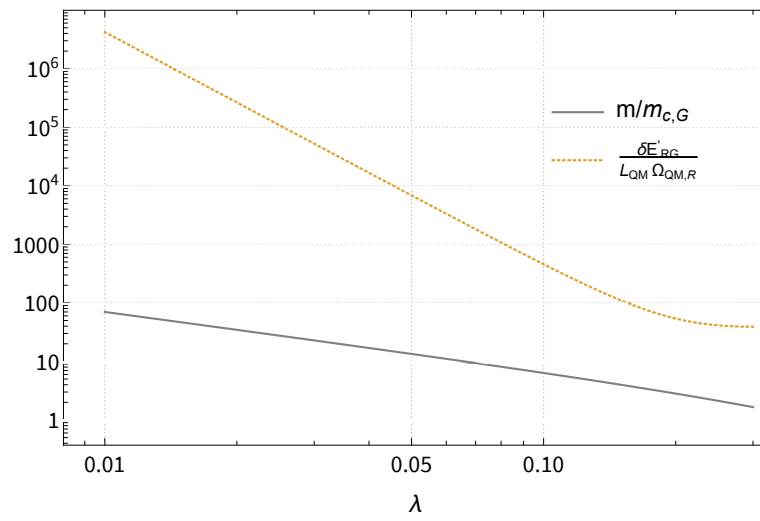


Figure 5.18: Particle mass  $m$  in units of  $m_{c,G}$  and the energy difference  $\delta E'_{RG}/(\Omega_{QM,R}L_{QM})$  as a function of the spin-parameter  $\lambda$  for fixed total angular momentum  $L = L_{QM}$ .

---

## Chapter 6

# Conclusions and discussion

We have examined gravitationally bound structures made up of macroscopically condensed ultra-light dark matter particles. These structures are referred to as Bose-Einstein condensed dark matter halos whose  $N$  particles may be described by one single scalar wavefunction. These bound systems obey the Gross-Pitaevskii-Poisson system of equations which can be written in the form of quantum-mechanical fluid equations allowing for two distinct regimes. This thesis' analysis has a focus on the so-called fuzzy regime in which merely the quantum pressure arising from the uncertainty principle acts against gravity. Here, we encounter a regime in which all length scales and contributions to the total energy are comparable, making it a challenging working ground for (semi-)analytical considerations. Bose-Einstein condensation of astronomically relevant extent requires the de-Broglie wavelength to be of same order as the system's size. In addition, perturbations of the system due to its quantum nature can also be of same order as the system's size, which yields  $m \approx m_c = 0.923 \times 10^{-25} (R/100\text{kpc})^{-1/2} (M/10^{12} M_\odot)^{-1/2}$ .

However, the main objective of our analysis has been to study the occurrence of the distinct phenomenology *rotating* laboratory BECs and hence BEC- dark matter halos may exhibit. In fact, the Gross-Pitaevskii equation allows for *vortex* solutions describing mini-tornadoes in the fluid where the density goes to zero and the velocity diverges. These vortex lines are manifestations of the quantized vorticity in superfluids and the building blocks of quantum turbulence. To be more precise, we have pursued the question whether the formation of a single central vortex in a BEC-DM halo in equilibrium, whose degree of rotational support is given by the common spin-parameter values of cosmological simulations, is energetically favored in the context of two halo models. To this aim, we took two valid approximations to the density profile of the "soliton" groundstate of the Schrödinger-Poisson system, a Gaussian wave-packet and an ( $n = 2$ ) polytrope, and paired them with two different halo geometries, a sphere and an irrotational Riemann-S ellipsoid respectively. As a result of our two energy arguments, we come to the conclusion that vortex formation in the

---

fuzzy regime is not energetically favored, neither in the case of our spherical setup in halo model A, nor in the case of the ellipsoidal geometry of halo model B. We therefore conclude that vortices are not to be expected for virialized gravitationally bound groundstate BECDM halos in the fuzzy regime, regardless of the choice of parameters we have considered. Moreover, we have shown in the context of both models that vortex formation is even less favored for higher dark matter particle masses.

Current findings, most notably coming from the realm of numerical simulations, are in striking accordance with our predictions regarding several aspects that we will dedicate the remaining Chapter to. These numerical simulations investigate fuzzy dark matter whose dynamics is governed by the time-dependent Schrödinger-Poisson system,

$$i\hbar \frac{\partial \psi}{\partial t} = -\frac{\hbar^2}{2m} \Delta \psi + m\Phi \psi, \quad (6.1)$$

$$\Delta \Phi = 4\pi G m |\psi|^2. \quad (6.2)$$

At this point, it is important to highlight that what is termed “halo” in the context of our analysis corresponds to what is referred to as the “halo cores” of final virialized halos in papers on merger simulations of “primordial solitons”.

[Schwabe et al. \(2016\)](#) simulate the dynamics of so-called solitons, i.e. ground state solutions of the Schrödinger-Poisson system, predicted to constitute the cores of dark matter halos in the context of fuzzy dark matter. To be more precise, they investigate binary and multiple mergers of up to 13 members made up of dark matter particles with masses of  $2.5 \times 10^{-22}$  eV. One generic signature of fuzzy dark matter is the existence of these compact soliton cores which are embedded in a halo structure with a density profile whose outer part declines like NFW density profiles. They study the final structure of these cores within a simplified setup in which just the two isolated cores merge. This is based on the time scales of major mergers governed by dynamical friction being much larger than the gravitational time scales of the solitonic cores. They implemented the Schrödinger equation in comoving coordinates and considered a grid size of  $512^3$  cells. Their three-dimensional simulation is based on a 4th-order Runge-Kutta finite-difference solver on this grid.

Due to the scaling symmetry of the Schrödinger-Poisson system (2.66) the initial condition of their binary collisions is given by the mass ratio  $\mu$ , the core distance, the relative velocity, the total mass  $M$ , the phase difference and the angular momentum perpendicular to the orbital plane. Their runs can be divided into two different regimes; unbound cores with positive total energy, i.e. high relative velocity, and bound cores with negative total energy, i.e. zero relative velocity. Unbound cores pass through each other, superpose while transferring quantum-kinetic energy  $K_Q$  (2.29) to bulk kinetic energy  $T$  and back <sup>17</sup> and remain

---

<sup>17</sup>In the context of simulations, the quantum kinetic energy  $K_Q$  is often referred to as gradient energy.

---

to a great extent undisturbed. The relative motion of the cores is stored in their interference pattern during collision which results in the energy transformation. Bound systems show essentially different dynamics and evolution of global quantities. Two bound solitonic cores merge rapidly and the emerging new core relaxes via gravitational cooling where energy and mass are carried away towards the grid boundaries and eventually absorbed by an imaginary potential, i.e. a sponge [Schwabe et al. \(2016\)](#) artificially add to the time-dependent Schrödinger equation governing the evolution of the system. Their representative runs show that the process of merging takes roughly one free-fall time after which a new excited soliton core forms. Their main result is that the evolution of the new core mass and the fraction of the emerging core mass  $M_c$  to the sum of the two initial core masses is nearly independent of parameters like the binary angular momentum, initial phase difference between the cores or their initial distance but rather depends weakly on  $\mu$ , the total energy  $E$  and total initial mass  $M$ . Their runs follow power laws of the form

$$M_c/M \propto \left( \frac{|E|}{M^3} \right)^{1/x}, \quad (6.3)$$

with  $x = 4$  or  $6$  depending on the specific run parameter setting. It appears that the mass of the newly-formed core comprises  $\approx 70\%$  of the sum of the masses of the progenitors. [Schwabe et al. \(2016\)](#) find that the final solitonic cores of their simulations are well fit by the soliton profile of [Schive et al. \(2014b\)](#),

$$\rho_{\text{soliton}} \approx \rho_0 \left[ 1 + 0.091 \left( \frac{r}{r_c} \right)^2 \right]^{-8}, \quad (6.4)$$

with  $r_c$  denoting the solitonic core radius and  $\rho_0$  the central density (cf. equation (2.71)), while the density of the surrounding envelope declines roughly as  $r^{-3}$ , as is the case for NFW profiles. These features are already seen in binary mergers, not only in multimerger simulations.

[Schwabe et al. \(2016\)](#) find that their emerging solitonic cores are rotating ellipsoids, if the system is initialized with non-zero total angular momentum. In fact, the respective volume rendered images and velocity fields of the cores strongly indicate that they resemble irrotational Riemann-S ellipsoids, as the authors point out. The same conclusion was drawn by [Edwards et al. \(2018\)](#). While the older work by [Rindler-Daller and Shapiro \(2012\)](#) had introduced Riemann-S ellipsoids, their study was limited to the Thomas-Fermi regime. Now, the work in this thesis has firmly shown that irrotational Riemann-S ellipsoids can be used in the fuzzy regime, as well. In this regard, the compressible irrotational Riemann-S ellipsoid incorporated into our halo model B constitutes a valid framework in order to provide analytical counterparts for the formed solitonic halo cores of BEC-DM halo formation simulations.

---

Mocz et al. (2017) present a set of 100 numerical simulations in which a group consisting of 4 to 32 primordial solitonic cores merge and form one final halo whose core is well-fitted by the density profile introduced by Schive et al. (2014b). However, in contrast to the simulations by Schive et al. (2014b) and Schwabe et al. (2016), they specifically include the study of quantum turbulence exhibited by the final halos which is particularly interesting to compare with our results from Section 5. Their merger simulations, aimed at studying small-scale phenomena of Bose-Einstein condensed dark matter in a cosmological context, obviously rely on evolution under the time-dependent Schrödinger-Poisson system. As a consequence, the theoretical background of their numerical simulations include the Madelung transformation, the total energy  $E = K_Q + T + W$  (see (2.29) and (2.30)), the virial theorem,  $0 = 2\langle K \rangle + \langle W \rangle$ , where  $\langle \rangle$  denotes the time average and the system's total net angular momentum  $\vec{L}$  set to zero. They mention that if one allows for the condensate's wave function to depend on the position vector  $\vec{r}$ , i.e. in general  $S = S(\vec{r}, t)$ , then spatial wave interference could seed turbulence. Notice that we do indeed consider  $S = S(\vec{r})$  in the case of our vortex ansatz (5.13) and (5.14), but that one single vortex does not fall into the category of quantum turbulence. In contrast to the 4th-order Runge-Kutta finite-difference solver of Schwabe et al. (2016), the method of Mocz et al. (2017) is a second-order pseudo-spectral solver employing a "kick-drift-kick" technique, which they describe in their Subsection 3.1. Moreover, while Schwabe et al. (2016) employ the sponge at their box boundaries, Mocz et al. (2017) choose periodic boundary conditions which allow wave reflection at the boundaries and therefore the total energy  $E$  as well as the total mass  $M$  are conserved during their simulations of bound systems. Therefore Mocz et al. (2017) are closer to the cosmological case whereas Schwabe et al. (2016)'s results are more comparable to "isolated" merger systems in a static background.

Given the soliton fit (6.4), Mocz et al. (2017) find that the break between the soliton profile and the outer NFW-like profile within the final virialized BEC-DM halo occurs universally at  $\approx 3.5r_c$ , which approximately corresponds to the soliton radius. Moreover, they find that the ratio between the soliton core mass  $M_c$  and the total mass traces the energy of the system since according to their analysis

$$\frac{M_c}{M} \propto \left( \frac{|E|}{M^3} \right)^{1/3}. \quad (6.5)$$

However, most interesting in the context of our analysis are their results on turbulence and vortex lines exhibited by the final halo. By analysing the energy power spectra  $E_k$ , the radial energy density profiles and 2D slices of  $|\psi|$  of their 100 simulations, Mocz et al. (2017) conclude the following. In general, they see sustained chaotic motion, granules and turbulence everywhere in the domain except for the central solitonic core. The stable soliton core stays free of substructure and disruption from turbulence. The radial energy density profiles show that the quantum gradient energy supports the structure up to  $2.7r_c$ . Beyond that radius all three energy density contributions become comparable yielding a characteristic signature of

---

turbulence, equipartition. The energy power spectra lack power for small  $k$  (large scales), show a mode which displays most of the turbulence and follow a  $k^{-1.1}$  power law for large  $k$  (small scales). This resembles the spectrum of thermally-driven and hence isotropic turbulence of Gross-Pitaevskii fluids, see Section 3.4, where small modes dominate. Mocz et al. (2017) show that the power spectra of their simulations peak at  $2\pi/k_{peak} \approx 7.5r_c$  which corresponds to a scale of twice the soliton radius. This explains why the filamentary distribution of the  $|\psi|$  and phase function fields (outside the soliton) seen in their figure 6 show preferentially soliton width sized granules. The reason is that inside the soliton turbulence and thereby the small-wavelength modes' contribution is suppressed, Mocz et al. (2017) do not see any vortex lines entering the soliton, and the dominant soliton-width-scaled modes disturb the larger ones thereby lowering their contribution seen in the power spectrum. Finally, Mocz et al. (2017) take the next step of coupling their BEC- dark-matter-only simulations to baryonic components in Mocz et al. (2020).

This vortex-free solitonic core embedded into a turbulent envelope, which is traversed with vortex lines seen by Mocz et al. (2017), goes along the same lines of our analysis due to the following reasons. On the one hand, according to Mocz et al. (2017), no vortex-line enters the central solitonic core. This is in perfect consistency with our findings where we have approximated the ground state "soliton" solution of the Schrödinger-Poisson system by either a Gaussian or an ( $n = 2$ )-polytropic profile with the result that vortex formation is energetically not favored. On the other hand, the fact that Mocz et al. (2017)'s multimerger-simulations yield a final halo with sustained chaotic motion, granules and turbulence in its outer region, does in no way contradict our conclusions. The reason is that the merging of primordial solitons yields excitation, superposition and interference of  $\psi$ -waves. In particular, also destructive interference occurs which takes the form of vortex-lines. However, Schive et al. (2014a)'s cosmological simulations showed that in the center of gravitationally bound objects made up of BEC-DM in the fuzzy limit, one finds coherent standing waves, i.e. stable solitonic cores. Exactly these manifestations of the attractor solution of the Schrödinger-Poisson system were our object of investigation and results for them are in agreement with ours.

Hui et al. (2020) dedicate a mixture of analytical and numerical analysis to exactly those outer regions of the virialized BEC-DM halo that do exhibit these turbulent dynamics and like us <sup>18</sup> focus on formation of vortices. It is important to highlight that they investigate analytical "defect" solutions in the absence of gravity and only incorporate gravitational effects in their numerical simulations. However, since all characteristic length scales in the fuzzy regime of the Gross-Pitaevskii-Poisson system (unlike the Thomas-Fermi regime) are

---

<sup>18</sup>However, have in mind that our analysis considers wave defects like vortices in cores subject to angular momentum in contrast to destructive interference in the outer regions of halo envelopes into which these cores are embedded.

---

of equal order, for example perturbations characterized by the vortex core size  $s$  can in principle reach the system size, there are no leading energy terms emerging in the fuzzy limit. This feature can also be seen in figures (5.5) to (5.7), where the gravitational potential energy due to the vortex proves to be very significant. [Hui et al. \(2020\)](#) then test their expectations by running numerical simulations including gravity. In addition, they apply a random phase model in order to investigate the probability of destructive interference and thereby the frequency of vortex-line occurrence. This approach may be a promising way to develop analytical studies of the turbulent outer regions of BEC-DM halos.

## Appendix A

# Polytropic spheres

Classical literature on stellar structure like [Chandrasekhar \(1939\)](#) or [Kippenhahn et al. \(2012\)](#) present a special class of equilibrium configurations of gas spheres, so-called polytropic spheres.

For spheres in hydrostatic equilibrium one shall require

$$\frac{dP}{dr} = -\frac{d\Phi}{dr}\rho, \quad (\text{A.1})$$

considering static and spherically symmetric solutions only, and combine with the Poisson equation

$$\frac{1}{r^2} \frac{d}{dr} \left( r^2 \frac{d\Phi}{dr} \right) = 4\pi G\rho, \quad (\text{A.2})$$

where  $P$  denotes the pressure,  $\rho$  the density and  $\Phi$  the gravitational potential of the system.

This class of configurations is characterized by a simple so-called polytropic relation between the pressure and the density of the form

$$P = K_p \rho^{1+\frac{1}{n}}, \quad (\text{A.3})$$

where the polytropic "constant"  $K_p$  and the polytropic index  $n$  are constant. [Kippenhahn et al. \(2012\)](#) mention that there are two reasons for a polytropic relation specifically in stars. On the one hand the equation of state of the gas can have the form (A.3), in which case  $K_p$  is fixed by natural constants. On the other hand, the equation of state may contain the temperature  $T$  and in addition we have a relation between  $T$  and  $P$ . These two relations then yield a polytropic relation, where however  $K_p$  is a free parameter that can vary from star to star.

---

By introducing the dimensionless variables

$$\theta = \left( \frac{\rho}{\rho_c} \right)^{1/n}, \quad \zeta = \frac{r}{a}, \quad (\text{A.4})$$

where  $\rho_c$  denotes the central density and

$$a = \rho_c^{\frac{1}{2}(\frac{1}{n}-1)} \sqrt{\frac{K_p(n+1)}{4\pi G}}, \quad (\text{A.5})$$

after combining equations (A.1),(A.2) and (A.3), one obtains the fundamental differential equation

$$\frac{1}{\zeta^2} \frac{d}{d\zeta} \left( \zeta^2 \frac{d\theta}{d\zeta} \right) = -\theta^n, \quad (\text{A.6})$$

the famous Lane-Emden equation with boundary conditions

$$\theta(0) = 1, \quad (\text{A.7})$$

$$\theta'(0) = 0. \quad (\text{A.8})$$

Here, the prime denotes differentiation with respect to  $\zeta$ . Solutions corresponding to  $0 \leq n < 5$  have a compact support. Thus, they become zero at a finite radius  $\zeta_1$ :

$$\theta|_{\zeta=\zeta_1} = 0. \quad (\text{A.9})$$

In that case, one can define a so-called complete polytrope with surface at  $\zeta = \zeta_1$  and subsequently its radius, mass and mass-radius relation depending on the polytropic index  $0 \leq n < 5$ :

$$R = \zeta_1 \sqrt{\frac{K_p(n+1)}{4\pi G}} \rho_c^{-\frac{n-1}{2n}}, \quad (\text{A.10})$$

$$M = -4\pi \frac{\theta'_1}{\zeta_1} \rho_c R^3, \quad (\text{A.11})$$

$$M^{(n-1)/n} R^{(3-n)/n} = -\zeta_1^{(n+1)/n} \theta_1'^{(n-1)/n} \frac{K_p(1+n)}{G(4\pi)^{1/n}}. \quad (\text{A.12})$$

Only for  $n \in \{0, 1, 5\}$  there exists a solution which can be given by analytical expressions. Chandrasekhar (1939) presents several tables of numerical values for polytropic models with index  $n$ . Some of the basic values are listed in table A.1.

An expansion of equation (A.6) shows that the point  $\zeta = 0$  represents a regular singu-

---

n	$\zeta_1$	$\left(-\zeta^2 \frac{d\theta}{d\zeta}\right) \Big _{\zeta=\zeta_1}$	$\rho_c / \bar{\rho}$
0	2.4494	4.8988	1.0000
1	3.14159	3.14159	3.28987
1.5	3.65375	2.71406	5.99071
2	4.35287	2.41105	11.40254

Table A.1: Numerical values of polytropes with index  $n$  according to Chandrasekhar (1939).  $\bar{\rho}$  denotes the mean density and  $\rho_c$  the central density.

larity of the ordinary differential equation. Thus any numerical method will have difficulty starting at  $\zeta = 0$ . We therefore started integrating at some value  $\zeta = \zeta'$  near zero. However, accurate solutions then require initial conditions at  $\zeta'$ . The approach was to calculate a Taylor series expansion of  $\theta$  about  $\zeta = 0$  and to use this series in order to determine the initial conditions at  $\zeta'$ . The implementation in Mathematica-12.0 (2019) yielded the numerical values shown in table A.2.

The global energy terms given by Lai et al. (1993) include the constants  $\kappa_n$  and  $q_n$  depending on the polytropic index  $n$ . Through numerical integration by Mathematica-12.0 (2019) we get

$$\kappa_n \equiv \frac{5}{3\zeta_1^4 |\theta'_1|} \int_0^{\zeta_1} \theta^n \zeta^4 d\zeta \begin{cases} = \frac{5}{3} \left(1 - \frac{6}{\pi^2}\right) \approx 0.653 & \text{for } n = 1 \\ \approx 1.4481 & \text{for } n = 2 \end{cases} \quad (\text{A.13})$$

and

$$q_n \equiv \kappa_n \left(1 - \frac{n}{5}\right) \begin{cases} = \frac{4}{3} \left(1 - \frac{6}{\pi^2}\right) \approx 0.523 & \text{for } n = 1 \\ \approx 0.868859 & \text{for } n = 2. \end{cases} \quad (\text{A.14})$$

n	$\zeta_1$	$\kappa_n$	$q_n$
1	3.14159265	0.653455	0.522764
2	4.352874593	1.4481	0.868859

Table A.2: Numerical values calculated by Mathematica-12.0 (2019)

---

## Appendix B

# The perturbed halo potential $\Phi_1$ : An analytical approach

We have already indicated in Section 5.1, that finding an analytical expression for the inner-vortex solution  $\Phi_1^{(i)}$  is a difficult or rather virtually impossible task to undertake. This Appendix shall for the sake of completeness present our effort in constructing such an expression by means of several severe assumptions.

The density perturbation due to the central singly-quantized vortex,

$$\begin{aligned} \rho_1 &= \rho - \rho_0 = m \frac{\rho_0}{m} |w|^2 - \rho_0 \\ &= \rho_0 (|w|^2 - 1) \\ &= \begin{cases} 0 & \text{for } r \geq s \text{ (outside the vortex)} \\ \rho_0 \left( C_n^2 \left( \frac{r}{s} \right)^2 - 1 \right) < 0 & \text{otherwise,} \end{cases} \end{aligned} \quad (\text{B.1})$$

is the source of the gravitational potential  $\Phi_1$ . Hence,

$$\Delta \Phi_1 = \begin{cases} \Delta \Phi_1^{(o)} = 0 & \text{for } r \geq s \\ \Delta \Phi_1^{(i)} = 4\pi G \rho_c e^{-ar^2} e^{-az^2} \left( C_n^2 \left( \frac{r}{s} \right)^2 - 1 \right) & \text{otherwise.} \end{cases} \quad (\text{B.2})$$

We found that in order to arrive at some approximation to the true solution of

$$\Delta \Phi_1^{(i)} = 4\pi G \rho_c e^{-ar^2} e^{-az^2} \left( C_n^2 \left( \frac{r}{s} \right)^2 - 1 \right) \text{ for } r < s, \quad (\text{B.3})$$

it is recommended to base the calculations on an equivalent formulation, namely the Poisson

---

integral for some general potential  $\Phi(\vec{r})$  and density field  $\rho(\vec{r})$ ,

$$\Phi(\vec{r}) = -G \int_V \frac{\rho(\vec{r}')}{|\vec{r} - \vec{r}'|} d^3r'. \quad (\text{B.4})$$

In our case and in cylindrical coordinates  $(r, \phi, z)$ , this amounts to

$$\Phi_1^{(i)}(\vec{r}) = -G \int_{-R}^R \int_0^{2\pi} \int_0^s \rho_c e^{-ar'^2} e^{-az'^2} \left( C_n^2 \left( \frac{r'}{s} \right)^2 - 1 \right) \frac{1}{|\vec{r} - \vec{r}'|} r' dr' d\phi' dz'. \quad (\text{B.5})$$

Primed variables are supposed to cover every position within the domain of integration and thereby include every part of the static, localized mass distribution, which is the source of the potential. From the theory of electrostatics, see [Fließbach \(2012\)](#), we know that for a position in space  $\vec{r}$  far away from the localized mass distribution  $\rho(\vec{r}')$ , the gravitational potential  $\Phi(\vec{r})$  is given by the so-called multipole expansion which converges under the above condition, i.e. a localized source close to the origin and a point at which the potential is observed far from the origin. Unfortunately, when searching for the inner-vortex solution  $\Phi_1^{(i)}(\vec{r})$ , the points at which the potential is observed lie within the mass distribution, which implies that the multipole expansion cannot be applied in the first place. However, based on the assumption that the multipole expansion method is legitimate in a case where the point at which the potential is observed lies precisely at the boundary of the localized density distribution, we can split the domain of integration in the hope of finding a subdomain of integration which allows the multipole expansion method. The following considerations are illustrated in figure [B.1](#). Our domain of integration is the vortex cylinder defined by

$$r \in [0, s] \quad (\text{B.6})$$

$$\phi \in [0, 2\pi], \quad (\text{B.7})$$

$$z \in [0, R]. \quad (\text{B.8})$$

Imagine a reflection of the area shown in [B.1](#) with respect to the  $r'$ -axis and then rotating both areas about the  $z'$ -axis. Every fixed position within the domain, pointed at by the vector  $\vec{r}$ , divides this domain into four subdomains, denoted by 1, 2, 3 and 4 in figure [B.1](#). Given the vector components of the now fixed vector  $\vec{r}$  and the vector  $\vec{r}'$  pointing at somewhere in the domain in cylindrical coordinates, i.e.  $(r, \phi, z)$  and  $(r', \phi', z')$ , the subdomains 1, 2, 3 and 4

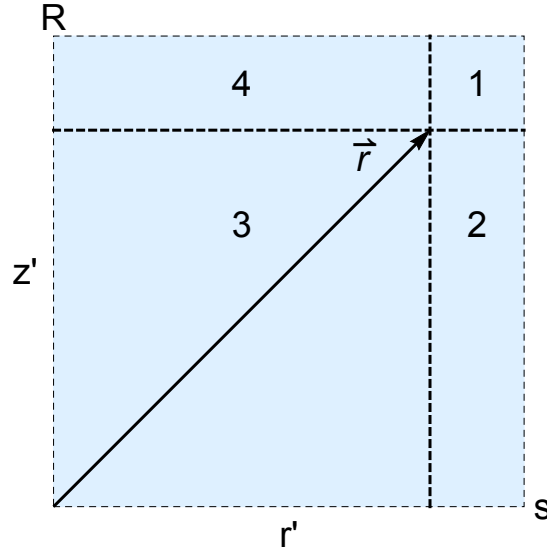


Figure B.1: Splitting the domain of integration

are given by

$$\text{subdomain 1: } r' > r, z' > z \quad (\text{B.9})$$

$$\text{subdomain 2: } r' > r, z' \leq z \quad (\text{B.10})$$

$$\text{subdomain 3: } r' \leq r, z' \leq z \quad (\text{B.11})$$

$$\text{subdomain 4: } r' \leq r, z' > z. \quad (\text{B.12})$$

From that we can infer that the density distribution within subdomain 3 allows a multipole expansion in order to arrive at a potential although under unfavorable conditions since the point at which the potential is observed does not lie far from the distribution but just outside of it.

Following [Fließbach \(2012\)](#), the potential  $\Phi$  can be written as

$$\Phi(\vec{r}) = -G \sum_{l=0}^{\infty} \sum_{m=-l}^{+l} \sqrt{\frac{4\pi}{2l+1}} \frac{q_{lm}}{r_s^{l+1}} Y_{lm}(\theta, \phi), \quad (\text{B.13})$$

given the above conditions, where  $Y_{lm}(\theta, \phi)$  denote the spherical harmonics and for a cylindrical symmetric density distribution the coefficients are given by

$$q_{lm} = \delta_{m0} q_{l0} = \delta_{m0} \int_V \rho(r_s, \theta) r_s^l P_l(\cos \theta) . \quad (\text{B.14})$$

$(r_s, \theta, \phi)$  are spherical coordinates, the delta distribution implies

$$\delta_{m0} = \begin{cases} 0 & \text{for } m \neq 0 \\ 1 & m = 0 \end{cases} \quad (\text{B.15})$$

and  $P_l(x)$  denote the Legendre polynomials given explicitly by Rodrigues' formula, i.e.

$$P_l(x) = \frac{1}{2^l l!} \frac{d^l}{dx^l} (x^2 - 1)^l. \quad (\text{B.16})$$

The division of the integration domain effectively amounts to splitting the integration over the vortex-volume:

$$\begin{aligned} \int_V &= \int_1 + \int_2 + \int_3 + \int_4 \\ &= \left( \int_z^R + \int_{-R}^{-z} \right) \int_0^{2\pi} \int_r^s + \int_2 + \int_{-z}^z \int_0^{2\pi} \int_0^r + \int_4. \end{aligned} \quad (\text{B.17})$$

Since no strategy was found to approximate the integration over the subdomains 2 and 4, the total analytic expression will be approximated by the sum of the solutions for the domains 1 and 3:

$$\Phi_1^{(i)} \approx \Phi_{1,1}^{(i)} + \Phi_{1,3}^{(i)}. \quad (\text{B.18})$$

We are going to derive an analytic expression for  $\Phi_{1,3}^{(i)}$  by truncating the multipole expansion at  $l = 2$ , i.e. our approximation is given by the following partial sum:

$$\Phi_{1,3}^{(i)} \approx -G \left[ \frac{q_{00}}{r_s} + \frac{q_{10}}{r_s^2} \cos \theta + \frac{q_{20}}{2r_s^3} (3 \cos^2 \theta - 1) \right]. \quad (\text{B.19})$$

The monopole  $q_{00}$  is given by

$$\begin{aligned} q_{00} &= 4\pi\rho_c \int_0^z \int_0^r e^{-ar^2} e^{-az^2} \left( C_n^2 \left( \frac{r'}{s} \right)^2 - 1 \right) r' dr' dz' \\ &= 4\pi\rho_c \left[ \frac{e^{-ar^2} \sqrt{\pi}}{4a^{5/2}s^2} \left( (1 + ar^2 - e^{ar^2}) C_n^2 + a(e^{ar^2} - 1)s^2 \right) \text{Erf}(\sqrt{az}) \right]. \end{aligned} \quad (\text{B.20})$$

The dipole is evaluated by integrating an odd function of  $z'$  over a symmetric interval, thus yielding zero:

$$\begin{aligned} q_{10} &= 2\pi\rho_c \int_{-z}^z \int_0^r e^{-ar^2} e^{-az^2} \left( C_n^2 \left( \frac{r'}{s} \right)^2 - 1 \right) z' r' dr' dz' \\ &= 0. \end{aligned} \quad (\text{B.21})$$

And finally,

$$\begin{aligned}
q_{20} &= 2\pi\rho_c \int_{-z}^z \int_0^r e^{-ar^2} e^{-az'^2} \left( C_n^2 \left( \frac{r'}{s} \right)^2 - 1 \right) (r'^2 + z'^2) \frac{1}{2} \left( 3 \frac{z'^2}{r'^2 + z'^2} - 1 \right) r' dr' dz' \\
&= 2\pi\rho_c \frac{e^{-ar^2 - az^2}}{4a^{7/2}s^2} \left[ 2\sqrt{az} \left( C_n^2 + ar^2 C_n^2 - as^2 + e^{ar^2} (-C_n^2 + as^2) \right) \right. \\
&\quad \left. - e^{az^2} \sqrt{\pi} \left( (-1 - ar^2(1 + ar^2) + e^{ar^2}) C_n^2 + a^2 r^2 s^2 \right) \text{Erf}(\sqrt{az}) \right]. \tag{B.22}
\end{aligned}$$

In order to calculate the multipole expansion coefficients, we have made use of

$$z = r_s \cos \theta \tag{B.23}$$

$$r_s = \sqrt{r^2 + z^2} \tag{B.24}$$

$$P_0(x) = 1 \tag{B.25}$$

$$P_1(x) = x \tag{B.26}$$

$$P_2(x) = \frac{1}{2}[3x^2 - 1]. \tag{B.27}$$

Hence, we get

$$\Phi_{1,3}^{(i)} \approx -G \left[ \frac{q_{00}}{\sqrt{r^2 + z^2}} + \frac{q_{20}}{2(r^2 + z^2)^{3/2}} \left( 3 \frac{z^2}{r^2 + z^2} - 1 \right) \right]. \tag{B.28}$$

A quite different approach was applied in order to derive an analytical expression for  $\Phi_{1,1}^{(i)}$ . It holds true for subdomain 1 that  $r' > r$  and  $z' > z$ . Thus we proceed with the strong assumption that  $\vec{r} \ll \vec{r}'$  and therefore  $|\vec{r} - \vec{r}'| \approx |\vec{r}'|$ , which yields

$$\begin{aligned}
\Phi_{1,1}^{(i)} &\approx -G 4\pi\rho_c \int_z^R \int_r^s e^{-ar^2} e^{-az'^2} \left( C_n^2 \left( \frac{r'}{s} \right)^2 - 1 \right) \frac{1}{\sqrt{r'^2 + z'^2}} r' dr' dz' \\
&= G 4\pi\rho_c \int_z^R e^{-az'^2} \left[ \frac{e^{-ar^2}}{4a^{3/2}s^2} \left( -2C_n^2 \sqrt{a(r^2 + z'^2)} - e^{ar^2 + az'^2} \sqrt{\pi} \right. \right. \\
&\quad \left. \left. \times (2as^2 + C_n^2(-1 + 2az'^2)) \text{Erf} \left( \sqrt{a(r^2 + z'^2)} \right) \right) - \frac{e^{-as^2}}{4a^{3/2}s^2} \left( -2C_n^2 \sqrt{a(s^2 + z'^2)} - \right. \right. \\
&\quad \left. \left. e^{as^2 + az'^2} \sqrt{\pi} (2as^2 + C_n^2(-1 + 2az'^2)) \text{Erf} \left( \sqrt{a(s^2 + z'^2)} \right) \right) \right] dz'. \tag{B.29}
\end{aligned}$$

Unfortunately, due to the several severe approximations these considerations rely on, expression (B.18) including (B.28) and (B.29) yields a gravitational potential,

$$\tilde{\Phi}_{approx} \approx (\Phi_{1,1}^{(i)} + \Phi_{1,3}^{(i)}) \frac{1}{4\pi G \rho_c \sigma^2}, \tag{B.30}$$

---

which differs sufficiently enough from the numerical solution shown in figure 5.3 that we have not used this result for  $\Phi_1^{(i)}$  in our energy analysis.

## Appendix C

# Non-collisionality

What do the terms “collisionless” or more specifically “a collisionless system” refer to? What defines such systems? How can they be described? This Section is dedicated to provide answers to these questions based on [Binney and Tremaine \(2008\)](#) and [Dorfi \(2017\)](#).

According to [Binney and Tremaine \(2008\)](#), whether a system is collisional or collisionless is decided by the nature of the force governing the interactions between the system’s constituents. The fundamental difference between a *collisionless* galaxy and a *collisional* diffuse gas of molecules is the range of the underlying force. The trajectory of a molecule in a diffuse gas consists of long periods of unaffected movement with constant velocity and violent collisions with other molecules yielding short-lived accelerations. Their interaction is short-range. In contrast, stars in a galaxy or collisionless dark matter particles<sup>19</sup> are subject to gravity, which is long-range. Hence, a star in a galaxy “feels” a smooth acceleration given by a gravitational force that can be treated as if arising from a smooth density distribution rather than a sum of localized masses.

The so-called relaxation time  $t_{\text{relax}}$  offers a way to quantify the above notion and is given by

$$t_{\text{relax}} \sim \frac{N}{8 \ln N} t_{\text{cross}}, \quad (\text{C.1})$$

with  $N$  the total number of stars (or particles) and  $t_{\text{cross}}$  the crossing time of that system. The (whether frequent or unlikely) two-body encounters or “kicks” between passing objects of a system have altered one object’s orbit significantly from the orbit it would have had given a truly smooth gravitational field, after  $t_{\text{relax}}$ . Thus, as long as timescales of a system do not exceed  $t_{\text{relax}}$ , its dynamics is that of a *collisionless system*. For instance, the relaxation time of elliptical galaxies with  $N \sim 10^{12}$  exceeds by far the age of the universe.

Collisionless systems are described on the basis of the *collisionless Boltzmann equation*. In

---

<sup>19</sup>One can disregard weak or gravitational interaction between individual WIMPs in any galactic context.

---

order to derive this equation, Dorfi (2017) lists several necessary assumptions. It is assumed that the system consists of  $N$  particles, whose orbits do not vary drastically. No masses are created or destroyed. And finally, a smooth gravitational potential can be given in the Newtonian limit.

The basic idea is to use these assumptions and the characteristics of a collisionless system to avoid the unfeasible task of tracking every particle's orbit by introducing the *distribution function* (DF),  $f$ , which is defined such that

$$f(\vec{x}, \vec{p}, t) d^3x d^3p, \quad (\text{C.2})$$

gives the probability that at time  $t$  a particle has position  $\vec{x}$  and momentum  $\vec{p}$  in the given range.  $f$  is normalized such that

$$\int f(\vec{x}, \vec{p}, t) d^3x d^3p = 1. \quad (\text{C.3})$$

Some authors, like Dorfi (2017), prefer the DF already multiplied with the total number  $N$ , so that the normalization is given by

$$\int f(\vec{x}, \vec{p}, t) d^3x d^3p = N. \quad (\text{C.4})$$

As the DF evolves in time, probability must be conserved. Thus, there exists a continuity equation given by

$$\frac{\partial f}{\partial t} + \frac{\partial}{\partial w_i}(f \dot{w}_i) = 0, \quad (\text{C.5})$$

with  $\vec{w} = (w_i) = (x_1, x_2, x_3, p_1, p_2, p_3)$  denoting a set of canonical coordinates<sup>20</sup>. By using Hamilton's equations (and denoting the Hamiltonian as  $H$ )

$$\dot{x}_i = \frac{\partial H}{\partial p_i} \quad \dot{p}_i = -\frac{\partial H}{\partial x_i}, \quad (\text{C.6})$$

the second term of the continuity equation becomes

$$\frac{\partial}{\partial w_i}(f \dot{w}_i) = \frac{\partial}{\partial x_i} \cdot \left( f \frac{\partial H}{\partial p_i} \right) - \frac{\partial}{\partial p_i} \cdot \left( f \frac{\partial H}{\partial x_i} \right) \quad (\text{C.7})$$

$$= \frac{\partial f}{\partial x_i} \cdot \frac{\partial H}{\partial p_i} - \frac{\partial f}{\partial p_i} \cdot \frac{\partial H}{\partial x_i} \quad (\text{C.8})$$

$$= \dot{x}_i \cdot \frac{\partial f}{\partial x_i} + \dot{p}_i \cdot \frac{\partial f}{\partial p_i}. \quad (\text{C.9})$$

---

<sup>20</sup>Have in mind that we apply the Einstein summation convention unless otherwise stated in this Section.

---

As a result, one can obtain several forms of the *collisionless Boltzmann equation*:

$$\frac{\partial f}{\partial t} + \dot{x}_i \cdot \frac{\partial f}{\partial x_i} + \dot{p}_i \cdot \frac{\partial f}{\partial p_i} = 0, \quad (\text{C.10})$$

$$\frac{\partial f}{\partial t} + \{f, H\} = 0, \quad (\text{C.11})$$

$$\frac{df}{dt} = 0, \quad (\text{C.12})$$

where the definition of the Poisson bracket  $\{f, H\}$  and the Lagrangian derivative

$$\frac{df}{dt} \equiv \frac{\partial f}{\partial t} + \dot{w}_i \cdot \frac{\partial f}{\partial w_i} \quad (\text{C.13})$$

were used, see [Binney and Tremaine \(2008\)](#).

Inserting the Hamiltonian  $H = \frac{\vec{p}^2}{2m} + \phi(\vec{x}, t)$  with the gravitational potential  $\phi$  into (C.11) yields

$$\frac{\partial f}{\partial t} + \frac{p_i}{m} \cdot \frac{\partial f}{\partial x_i} - \frac{\partial \phi}{\partial x_i} \cdot \frac{\partial f}{\partial p_i} = 0. \quad (\text{C.14})$$

The collisionless Boltzmann equation together with the Poisson equation

$$\Delta \phi = 4\pi G \rho = 4\pi G m n = 4\pi G m N \int f(\vec{x}, \vec{p}, t) d^3 p, \quad (\text{C.15})$$

given the number density

$$n(\vec{x}, t) = N \int f(\vec{x}, \vec{p}, t) d^3 p, \quad (\text{C.16})$$

and same mass  $m$  for all particles, form a self-contained system which in principle determines the complete dynamics of this star- or dark matter-“gas”. However, calculating the distribution function  $f$  is often not practical.

In order to have a better understanding of the system’s behavior, it is helpful to infer so-called moments of the Boltzmann equation. It is customary to interpret  $f$  as a function of the velocity components  $v_i = p_i/m$ , rather than momentum components  $p_i$ . For this  $f$ , the Boltzmann equation reads

$$\frac{\partial f}{\partial t} + v_i \cdot \frac{\partial f}{\partial x_i} - \frac{\partial \phi}{\partial x_i} \cdot \frac{\partial f}{\partial v_i} = 0. \quad (\text{C.17})$$

The  $0th$  moment is the probability density distribution  $\nu(\vec{x}, t)$ :

$$\nu(\vec{x}, t) = \int f(\vec{x}, \vec{v}, t) d^3 v. \quad (\text{C.18})$$

---

The first moment is the mean velocity  $\bar{v}_i$ , defined by

$$\bar{v}_i(\vec{x}, t) = \frac{1}{\nu} \int v_i f(\vec{x}, \vec{v}, t) d^3v. \quad (\text{C.19})$$

Integrating the Boltzmann equation over all velocities, gives

$$\int \frac{\partial f}{\partial t} d^3v + \int v_i \cdot \frac{\partial f}{\partial x_i} d^3v - \int \frac{\partial \phi}{\partial x_i} \cdot \frac{\partial f}{\partial v_i} d^3v = 0. \quad (\text{C.20})$$

The partial time derivative may be taken outside the integral in (C.20) (no time-dependancy of the bounds of integration). Thus, by considering the definition of  $\nu(\vec{x}, t)$ , the first term can be rewritten as

$$\frac{\partial \nu}{\partial t}. \quad (\text{C.21})$$

Moreover, the partial derivative  $\frac{\partial}{\partial x_i}$  can be taken outside the integral due to the independence between  $x_i$  and  $v_i$ . The second term therefore becomes

$$\frac{\partial(\nu \bar{v}_i)}{\partial x_i}. \quad (\text{C.22})$$

The last term can be evaluated by direct integration:

$$-\frac{\partial \phi}{\partial x_i} \int \frac{\partial f}{\partial v_i} d^3v = -\frac{\partial \phi}{\partial x_i} \int_{-\infty}^{\infty} \int_{-\infty}^{\infty} f|_{v_i=-\infty}^{v_i=\infty} d^2v_{j \neq i} = 0, \quad (\text{C.23})$$

since there are no particles with infinite speed. The result is the so-called continuity equation for collisionless systems or *first Jeans equation*,

$$\frac{\partial \nu}{\partial t} + \frac{\partial(\nu \bar{v}_i)}{\partial x_i} = 0. \quad (\text{C.24})$$

In order to derive the second Jeans equation, an equation of motion similar to the one in hydrodynamics, the Boltzmann equation is multiplied by  $v_j$  before integrating over all velocities,

$$\int v_j \frac{\partial f}{\partial t} d^3v + \int v_j v_i \cdot \frac{\partial f}{\partial x_i} d^3v - \int v_j \frac{\partial \phi}{\partial x_i} \cdot \frac{\partial f}{\partial v_i} d^3v = 0. \quad (\text{C.25})$$

Partial integration of the integral in the last term gives

$$\int v_j \frac{\partial f}{\partial v_i} d^3v = \int v_j (f(v_i))|_{v_i=-\infty}^{v_i=\infty} d^2v_{j \neq i} - \int f \frac{\partial v_j}{\partial v_i} d^3v = -\nu \delta_{ij}. \quad (\text{C.26})$$

Following the same argumentation as above and defining the second moment of the Boltzmann equation

---


$$\overline{v_i v_j}(\vec{x}, t) = \frac{1}{v} \int v_i v_j f(\vec{x}, \vec{v}, t) d^3 v \quad (\text{C.27})$$

leads to the *second Jeans equation*,

$$\frac{\partial(v\overline{v_j})}{\partial t} + \frac{\partial(v\overline{v_i v_j})}{\partial x_i} + v \frac{\partial\phi}{\partial x_j} = 0. \quad (\text{C.28})$$

In order to put this equation into a more familiar form, the definition of the velocity-dispersion tensor,

$$\sigma_{ij}^2(\vec{x}, t) \equiv \frac{1}{v} \int (v_i - \overline{v_i})(v_j - \overline{v_j}) f(\vec{x}, \vec{v}, t) d^3 v = \overline{v_i v_j} - \overline{v_i} \overline{v_j}. \quad (\text{C.29})$$

is needed.

Subtracting  $\overline{v_j}$  times the left-hand side of the first Jeans equation from the second Jeans equation (which is allowed since it equals 0) yields

$$v \frac{\partial\overline{v_j}}{\partial t} - \overline{v_j} \frac{\partial(v\overline{v_i})}{\partial x_i} + \frac{\partial(v\overline{v_i v_j})}{\partial x_i} + v \frac{\partial\phi}{\partial x_j} = 0. \quad (\text{C.30})$$

One can see that the result is analogous to Euler's equation of hydrodynamics by using the definition of the velocity-dispersion tensor:

$$v \frac{\partial\overline{v_j}}{\partial t} + v \overline{v_i} \frac{\partial\overline{v_j}}{\partial x_i} = -v \frac{\partial\phi}{\partial x_j} - \frac{\partial(v\sigma_{ij}^2)}{\partial x_i}. \quad (\text{C.31})$$

The last term on the right-hand side of this (sometimes called) *third Jeans equation* represents a kind of pressure force,  $-\nabla p$ . To be more precise,  $-v\sigma_{ij}^2$  is a stress tensor describing anisotropic pressure.

---

# Bibliography

- Anderson, M. H., Ensher, J. R., Matthews, M. R., Wieman, C. E., and Cornell, E. A. (1995). Observation of Bose-Einstein Condensation in a Dilute Atomic Vapor. *Science*, 269(5221):198–201.
- Antonuccio-Delogu, V., Dobrotka, A., Becciani, U., Cielo, S., Giocoli, C., Macciò, A. V., and Romeo-Veloná, A. (2010). Dissecting the spin distribution of dark matter haloes. *Monthly Notices of the RAS*, 407(2):1338–1346.
- Arbey, A., Lesgourgues, J., and Salati, P. (2001). Quintessential halos around galaxies. *Physical Review D*, 64(12):123528.
- Arvanitaki, A., Dimopoulos, S., Dubovsky, S., Kaloper, N., and March-Russell, J. (2010). String axiverse. *Physical Review D*, 81(12):123530.
- Bahcall, J. N., Flynn, C., and Gould, A. (1992). Local Dark Matter from a Carefully Selected Sample. *Astrophysical Journal*, 389:234.
- Barenghi, C. F., L'vov, V. S., and Roche, P.-E. (2014). Experimental, numerical, and analytical velocity spectra in turbulent quantum fluid. *Proceedings of the National Academy of Science*, 111:4683–4690.
- Begeman, K. G., Broeils, A. H., and Sanders, R. H. (1991). Extended rotation curves of spiral galaxies : dark haloes and modified dynamics. *Monthly Notices of the RAS*, 249:523.
- Bertone, G., Hooper, D., and Silk, J. (2004). Particle dark matter: evidence, candidates and constraints. *Physics Reports*, 405:279–390.
- Binney, J. and Tremaine, S. (2008). *Galactic Dynamics: Second Edition*. Princeton University Press.
- Boylan-Kolchin, M., Bullock, J. S., and Kaplinghat, M. (2011). Too big to fail? The puzzling darkness of massive Milky Way subhaloes. *Monthly Notices of the RAS*, 415(1):L40–L44.

- 
- Bozek, B., Marsh, D. J. E., Silk, J., and Wyse, R. F. G. (2015). Galaxy UV-luminosity function and reionization constraints on axion dark matter. *Monthly Notices of the RAS*, 450(1):209–222.
- Bradley, C. C., Sackett, C. A., Tollett, J. J., and Hulet, R. G. (1995). Evidence of Bose-Einstein Condensation in an Atomic Gas with Attractive Interactions. *Physical Review Letters*, 75(9):1687–1690.
- Brooks, A. M., Kuhlen, M., Zolotov, A., and Hooper, D. (2013). A Baryonic Solution to the Missing Satellites Problem. *Astrophysical Journal*, 765(1):22.
- Burkert, A. (1995). The Structure of Dark Matter Halos in Dwarf Galaxies. *The Astrophysical Journal Letters*, 447:L25–L28.
- Chandrasekhar, S. (1939). *An introduction to the study of stellar structure*. The University of Chicago Press.
- Chandrasekhar, S. (1969). *Ellipsoidal figures of equilibrium*. Yale University Press.
- Chavanis, P.-H. (2019a). Derivation of the core mass-halo mass relation of fermionic and bosonic dark matter halos from an effective thermodynamical model. *Physical Review D*, 100(12):123506.
- Chavanis, P.-H. (2019b). Predictive model of BEC dark matter halos with a solitonic core and an isothermal atmosphere. *Physical Review D*, 100(8):083022.
- Coles, P. and Lucchin, P. (2003). *Cosmology: The Origin and Evolution of Cosmic Structure*. Wiley.
- Davidson, S. (2015). Axions: Bose Einstein condensate or classical field? *Astroparticle Physics*, 65:101–107.
- Davis, K. B., Mewes, M. O., Andrews, M. R., van Druten, N. J., Durfee, D. S., Kurn, D. M., and Ketterle, W. (1995). Bose-Einstein condensation in a gas of sodium atoms. *Physical Review Letters*, 75(22):3969–3973.
- Donnelly, R. J. (1991). *Quantized Vortices in Helium II*. Cambridge University Press.
- Dorfi, E. A. (2017). *Astrophysik II*. Skriptum zur Vorlesung.
- Edwards, F., Kendall, E., Hotchkiss, S., and Easther, R. (2018). PyUltraLight: a pseudo-spectral solver for ultralight dark matter dynamics. *Journal of Cosmology and Astroparticle Physics*, 2018(10):027.

- 
- Fließbach, T. (2012). *Elektrodynamik - Lehrbuch zur Theoretischen Physik II*. Springer-Verlag Berlin Heidelberg.
- Goodman, J. (2000). Repulsive dark matter. *New Astronomy*, 5(2):103–107.
- Gross, E. P. (1961). Structure of a quantized vortex in boson systems. *Il Nuovo Cimento*, 20(3):454–477.
- Guzmán, F. S. and Avilez, A. A. (2018). Head-on collision of multistate ultralight BEC dark matter configurations. *Physical Review D*, 97(11):116003.
- Guzmán, F. S. and Ureña-López, L. A. (2004). Evolution of the Schrödinger-Newton system for a self-gravitating scalar field. *Physical Review D*, 69(12):124033.
- Hooper, D. (2007). *Dark Cosmos: In Search of Our Universe's Missing Mass and Energy*. Harper-Collins.
- Hu, W., Barkana, R., and Gruzinov, A. (2000). Fuzzy Cold Dark Matter: The Wave Properties of Ultralight Particles. *Physical Review Letters*, 85(6):1158–1161.
- Hui, L., Joyce, A., Landry, M. J., and Li, X. (2020). Vortices and waves in light dark matter. *arXiv e-prints*, page arXiv:2004.01188.
- Hui, L., Ostriker, J. P., Tremaine, S., and Witten, E. (2017). Ultralight scalars as cosmological dark matter. *Physical Review D*, 95(4):043541.
- Jungman, G., Kamionkowski, M., and Griest, K. (1996). Supersymmetric dark matter. *Physics Reports*, 267:195–373.
- Kaup, D. J. (1968). Klein-Gordon Geon. *Physical Review*, 172(5):1331–1342.
- Kippenhahn, R., Weigert, A., and Weiss, A. (2012). *Stellar Structure and Evolution*. Astronomy and Astrophysics Library. Springer Berlin Heidelberg.
- Kolmogorov, A. (1941). The Local Structure of Turbulence in Incompressible Viscous Fluid for Very Large Reynolds' Numbers. *Akademiia Nauk SSSR Doklady*, 30:301–305.
- Lai, D., Rasio, F. A., and Shapiro, S. L. (1993). Ellipsoidal Figures of Equilibrium: Compressible Models. *Astrophysical Journal Supplement Series*, 88:205.
- London, F. (1938). The  $\lambda$ -Phenomenon of Liquid Helium and the Bose-Einstein Degeneracy. *Nature*, 141(3571):643–644.
- Madelung, E. (1927). Quantentheorie in hydrodynamischer Form. *Zeitschrift für Physik*, 40(3-4):322–326.

- 
- Marsh, D. J. E. (2016). Axion cosmology. *Physics Reports*, 643:1–79.
- Mathematica-12.0 (2019). Wolfram research, inc. Champaign, IL, 2019.
- McGaugh, S. S. and de Blok, W. J. G. (1998). Testing the Dark Matter Hypothesis with Low Surface Brightness Galaxies and Other Evidence. *Astrophysical Journal*, 499(1):41–65.
- Membrado, M., Pacheco, A. F., and Sañudo, J. (1989). Hartree solutions for the self-Yukawian boson sphere. *Physical Review A: General Physics*, 39(8):4207–4211.
- Mocz, P., Fialkov, A., Vogelsberger, M., Becerra, F., Shen, X., Robles, V. H., Amin, M. A., Zavala, J., Boylan-Kolchin, M., Bose, S., Marinacci, F., Chavanis, P.-H., Lancaster, L., and Hernquist, L. (2020). Galaxy formation with BECDM - II. Cosmic filaments and first galaxies. *Monthly Notices of the RAS*, 494(2):2027–2044.
- Mocz, P., Vogelsberger, M., Robles, V. H., Zavala, J., Boylan-Kolchin, M., Fialkov, A., and Hernquist, L. (2017). Galaxy formation with BECDM - I. Turbulence and relaxation of idealized haloes. *Monthly Notices of the RAS*, 471(4):4559–4570.
- Moore, B., Ghigna, S., Governato, F., Lake, G., Quinn, T., Stadel, J., and Tozzi, P. (1999). Dark Matter Substructure within Galactic Halos. *The Astrophysical Journal Letters*, 524(1):L19–L22.
- Moustakas, L. A. and Metcalf, R. B. (2003). Detecting dark matter substructure spectroscopically in strong gravitational lenses. *Monthly Notices of the RAS*, 339(3):607–615.
- Navarro, J. F., Frenk, C. S., and White, S. D. M. (1997). A Universal Density Profile from Hierarchical Clustering. *Astrophysical Journal*, 490(2):493–508.
- Peccei, R. D. and Quinn, H. R. (1977). CP conservation in the presence of pseudoparticles. *Physical Review Letters*, 38(25):1440–1443.
- Peebles, P. J. E. (2000). Fluid Dark Matter. *The Astrophysical Journal Letters*, 534(2):L127–L129.
- Pethick, C. J. and Smith, H. (2008). *Bose-Einstein Condensation in Dilute Gases*. Cambridge University Press, 2 edition.
- Pitaevskii, L. and Stringari, S. (2003). *Bose-Einstein Condensation*. Oxford University Press.
- Pitaevskii, L. P. (1961). Vortex lines in an imperfect bose gas. *Sov. Phys. JETP*, 13(2):451–454.
- Planck Collaboration (2016). Planck 2015 results. XIII. Cosmological parameters. *Astronomy and Astrophysics*, 594:A13.

- 
- Planck Collaboration (2018). Planck 2018 results. VI. Cosmological parameters. *arXiv e-prints*, page arXiv:1807.06209.
- Rindler-Daller, T. and Shapiro, P. R. (2012). Angular momentum and vortex formation in Bose-Einstein-condensed cold dark matter haloes. *Monthly Notices of the RAS*, 422(1):135–161.
- Rindler-Daller, T. and Shapiro, P. R. (2014). Complex Scalar Field Dark Matter on Galactic Scales. *Modern Physics Letters A*, 29(2):1430002.
- Rubin, V. C. (1954). *Fluctuations in the Space Distribution of the Galaxies*. PhD thesis, Georgetown University.
- Rubin, V. C. (1978). Sexism in science. *Physics Today*, 31(1):13.
- Rubin, V. C. (1982). Male world of physics? *Physics Today*, 35(5):121.
- Rubin, V. C. and Ford, W. Kent, J. (1970). Rotation of the Andromeda Nebula from a Spectroscopic Survey of Emission Regions. *Astrophysical Journal*, 159:379.
- Ruffini, R. and Bonazzola, S. (1969). Systems of Self-Gravitating Particles in General Relativity and the Concept of an Equation of State. *Physical Review*, 187(5):1767–1783.
- Schive, H.-Y., Chiueh, T., and Broadhurst, T. (2014a). Cosmic structure as the quantum interference of a coherent dark wave. *Nature Physics*, 10(7):496–499.
- Schive, H.-Y., Liao, M.-H., Woo, T.-P., Wong, S.-K., Chiueh, T., Broadhurst, T., and Hwang, W. Y. P. (2014b). Understanding the Core-Halo Relation of Quantum Wave Dark Matter from 3D Simulations. *Physical Review Letters*, 113(26):261302.
- Schwabe, B., Niemeyer, J. C., and Engels, J. F. (2016). Simulations of solitonic core mergers in ultralight axion dark matter cosmologies. *Physical Review D*, 94(4):043513.
- Schwarz, K. W. (1985). Three-dimensional vortex dynamics in superfluid  $^4\text{He}$ : Line-line and line-boundary interactions. *Physical Review B: Solid State*, 31(9):5782–5804.
- Spergel, D. N. and Steinhardt, P. J. (2000). Observational Evidence for Self-Interacting Cold Dark Matter. *Physical Review Letters*, 84(17):3760–3763.
- Springel, V. (2005). The cosmological simulation code GADGET-2. *Monthly Notices of the RAS*, 364(4):1105–1134.
- Springel, V., White, S. D. M., Jenkins, A., Frenk, C. S., Yoshida, N., Gao, L., Navarro, J., Thacker, R., Croton, D., Helly, J., Peacock, J. A., Cole, S., Thomas, P., Couchman, H.,

- 
- Evrard, A., Colberg, J., and Pearce, F. (2005). Simulations of the formation, evolution and clustering of galaxies and quasars. *Nature*, 435(7042):629–636.
- Tipler, P. A. and Mosca, G. (2015). *Physik für Wissenschaftler und Ingenieure*. Springer-Verlag Berlin Heidelberg.
- Tisza, L. (1938). Transport Phenomena in Helium II. *Nature*, 141(3577):913.
- Tod, P. and Moroz, I. M. (1999). An analytical approach to the Schrödinger-Newton equations. *Nonlinearity*, 12(2):201–216.
- Tsatsos, M. C., Tavares, P. E. S., Cidrim, A., Fritsch, A. R., Caracanhas, M. A., dos Santos, F. E. A., Barenghi, C. F., and Bagnato, V. e. S. (2016). Quantum turbulence in trapped atomic Bose-Einstein condensates. *Physics Reports*, 622:1–52.
- Tulin, S. and Yu, H.-B. (2018). Dark matter self-interactions and small scale structure. *Physics Reports*, 730:1–57.
- Viel, M., Lesgourgues, J., Haehnelt, M. G., Matarrese, S., and Riotto, A. (2005). Constraining warm dark matter candidates including sterile neutrinos and light gravitinos with WMAP and the Lyman- $\alpha$  forest. *Physical Review D*, 71(6):063534.
- Vogt, S. S., Mateo, M., Olszewski, E. W., and Keane, M. J. (1995). Internal Kinematics of the Leo II Dwarf Spheroidal Galaxy. *Astronomical Journal*, 109:151.
- Weinberg, D. H., Bullock, J. S., Governato, F., de Naray, R. K., and Peter, A. H. G. (2015). Cold dark matter: Controversies on small scales. *Proceedings of the National Academy of Science*, 122(10):12249–12255.
- Zwicky, F. (1933). Die Rotverschiebung von extragalaktischen Nebeln. *Helvetica Physica Acta*, 6:110–127.

# List of Figures

1.1	Rotation Curve	4
2.1	Different density profile models	27
4.1	Velocity field of the ( $n = 2$ ), irrotational Riemann-S ellipsoid in the rotating frame	45
4.2	Velocity field of the ( $n = 2$ ), irrotational Riemann-S ellipsoid in the rest frame	46
5.1	Model A: Density profile for $s/\sigma = 0.8$	54
5.2	Model A: Density profile for $s/\sigma = 1.8$	55
5.3	Model A: Numerical inside-vortex solution of the potential $\Phi_1$	59
5.4	Model A: Vortex Energy as a function of $s$	65
5.5	Model A: Crucial vortex energy terms as a function of $s$	66
5.6	Model A: Inner-vortex Gravitational energy as a function of $s$	67
5.7	Model A: Outer-vortex gravitational energy as a function of $s$	67
5.8	Model A: Vortex Energy as a function of $m$	68
5.9	Model A: Spin-parameter $\lambda$ as a function of $\Omega/\Omega_{QM}$	71
5.10	Model A: Vortex Energy as a function of $m$ with $\Omega$ fixed via equation (5.90)	72
5.11	Model A: Vortex Energy as a function of $m$ . Zoom-In	72
5.12	Model B: Energy difference as a function of $s$	81
5.13	Model B: Energy difference as a function of $m$	82
5.14	Irrotational Riemann-S ellipsoid with $\lambda = 0.05$	84
5.15	Irrotational Riemann-S ellipsoid with $\lambda = 0.3$	85
5.16	Model B: Energy difference as a function of $m$ for $\lambda = 0.1$	86
5.17	Dark matter particle mass as a function of $\lambda$	86
5.18	Model B: Energy difference $\delta E'_{RG}$ as a function of $\lambda$	87
B.1	Multipole expansion: Domain of integration	101